Modeling *Hydra* from neuron to muscle to behavior

Hengji Wang

A dissertation
submitted in partial fulfillment of the
requirements for the degree of

Doctor of Philosophy

University of Washington

2022

Reading Committee:

Adrienne Fairhall, Chair

Marcel den Nijs

Armita Nourmohammad

Eric Shea-Brown

Program Authorized to Offer Degree:
Physics

University of Washington

Abstract

Modeling *Hydra* from neuron to muscle to behavior

Hengji Wang

Chair of the Supervisory Committee:
Adrienne Fairhall
Physiology and Biophysics

The fundamental question in neuroscience is to understand how single neurons combine to function as a network, and how their activity drives muscles to produce variety of behaviors to interact with the environment and maintain the dynamic equilibrium of the whole system. *Hydra*, with a simple nervous system and a transparent body that is ideal for recently developed calcium imaging techniques, provides an ideal system in which to build a complete model to understand neural activity and the transformation from neuron to muscle to behaviors. While recent calcium imaging techniques have been applied in recording both neuronal and muscle activities, the mechanisms and principles that support these dynamics are still rarely known. In this work, I build a complete model describing the neuromechanics, single neuron dynamics and the neural network of *Hydra*, interpreting the experimental findings from a biophysical perspective. I first review the basic facts about *Hydra* and some modeling approaches that provide a toolbox for our modeling work. Next, I summarize the questions raised by recent calcium imaging of *Hydra*. I develop a complete mechanistic model that simulates the transformation from neural drive to calcium dynamics in the muscular system, which are converted into active forces that drive a biomechanical model to generate different movements. The model addresses detailed questions such as the mechanisms underlying different timescales of muscle dynamics and the interaction of different muscle layers, and provides a testbed to understand how behaviors arise from specific neural drive. Thirdly, I explore the mechanism behind the bursting dynamics of the

contraction burst network in *Hydra*. I propose that the periodic activity of single neurons is driven by mechanosensory signals due to water transportation in the myoepithelial tissue, and build an LIF-based neuronal model that successfully simulates the bursting pattern and reproduces the dynamical features observed in experiments. Finally, I construct a mutual inhibition network composed of two observed subnetworks in *Hydra*, simulating the network-level neural activity that has been recorded in both intact and bisected *Hydra*. Our models reveal a commonality between *Hydra*'s nervous system and the autonomic nervous system in advanced organisms.

TABLE OF CONTENTS

Page

List of Figures iii

List of Tables viii

Chapter 1: Introduction 1
1.1 Introduction to Hydra 1
1.2 Models of calcium dynamics 5
1.3 Models of bursting 8

Chapter 2: A complete biomechanical model of Hydra contractile behaviors, from neural drive to muscle to movement 23
2.1 Abstract 23
2.2 Introduction 24
2.3 Results 29
2.4 Discussion 41
2.5 Materials and Methods 45
2.6 Acknowledgement 51

Chapter 3: Modeling the osmotically driven bursting dynamics of Hydra CB neuron 89
3.1 Abstract 89
3.2 Introduction 90
3.3 Results 92
3.4 Discussion 102
3.5 Materials and Methods 103
3.6 Acknowledgements 104

Chapter 4: A mutual inhibition network model of the neural circuits of Hydra . . 113
4.1 Introduction 113
4.2 Results 115
4.3 Discussion 126

4.4 Materials and Methods 127

Chapter 5: Conclusions 132

LIST OF FIGURES

Figure Number Page

1.1 Simplified *Hydra* anatomy, adapted from [243]. 2

1.2 Gap junction connectivity between epitheliomuscular cells in epithelia, reproduced from [223]. 3

1.3 Topographical distribution of neurons in *Hydra*, reproduced from [79]. 4

1.4 A simple model of Ca^{2+} signaling, reproduced from [75]. 7

1.5 Four major classes of bursting models that are based on ionic mechanisms, reproduced from [121] 9

2.1 Framework of our project. Neural activity patterns trigger calcium dynamics in the muscle layers, which are transformed into contractile forces in the longitudinal (ectoderm; green) and circumferential (endoderm; red) directions, here indicated by the direction of fibres in the muscle layers. This provides the active force to drive a viscoelastic biomechanical model of the Hydra body column, simulating behaviors. 27

2.2 Single cell dynamics. (*A*) Intracellular calcium signaling model including two pathways: (i) in the *slow pathway* (red), neuropeptides bind a G protein-coupled receptor (GPCR) and activate a G protein, which activates phospholipase C (PLC) and hydrolyzes phosphatidylinositol bisphosphate (PIP2) into inositol 1,4,5-trisphosphate (IP_3), which plays a role of the second messenger for calcium signaling. IP_3 can bind to IP_3 receptors (IPR) on the endoplasmic reticulum (ER) membrane and thus cause the release of Ca^{2+} from the ER. Ca^{2+} is extruded to the extracellular space through plasma membrane Ca^{2+} ATPase (PMCA) and is recycled to the ER through sarco/endoplasmic reticulum Ca^{2+}-ATPase (SERCA) [90, 75]. (ii) the *fast pathway* (blue) is initiated by the binding of neuropeptides on ionotropic receptors, which activate ligand-gated ion channels (LGIC) and depolarize the cellular membrane [101]. The elevated membrane potential activates calcium channels (L-type/T-type), triggering a large influx of Ca^{2+} from the extracellular space and invoking a further depolarization. Meanwhile, the high membrane potential inactivates calcium channels and activates potassium channels, resulting in membrane repolarization [112]. (*B*) Simulated slow dynamics showing change of Ca^{2+} and IP_3 concentrations. (*C*) Simulated fast dynamics showing change of membrane potential and Ca^{2+} concentration. 28

2.3 Muscle sheet dynamics. (*A*) We simulate multicellular dynamics by coupling single cell models to their neighbors by gap junctions. (*B*) Simulation of the body column wave. (*C*) Simulation of the bending wave. (*D*) Simulation of the contraction pulse (fast wave). 31

2.4 Recorded fluorescence from calcium imaging showing simultaneous activation of ectoderm (green) and endoderm (red) during contractions, shown by computing the corresponding time-varying length (blue) of *Hydra*. 34

2.5 Body column settings and dynamics. (*A*) The layout of the body column model. Green and red represent the ectodermal and endodermal layers respectively, in which the myonemes are aligned in longitudinal and circumferential directions respectively, as represented by the fibre directions. Blue dots represent cross-layer gap junctions. (*B-D*) Connectivity patterns and calcium patterns of ectoderm (green border) and endoderm (red border) in simulations with different connectivity ratios, where the ratios are separately 20% (*B*), 2% (*C*) and 0.05% (*D*). In connectivity patterns each bright spot represents a gap-junctional connection at that position. (*E-F*) Diagrams show cross-layer propagation for different connection densities of cross-layer gap junctions. We simulate 20 epochs for each density; we take snapshots at 50ms and 100ms after only triggering the fast pathway (*E*), and 10s and 25s after only triggering the slow pathway (*F*), then average the $[Ca^{2+}]_i$ of the whole endoderm, plotting the mean and standard deviation of the 20 epochs for each density at these time points. (*G-H*) $[Ca^{2+}]_i$ traces and wavefronts along the center longitudinal line (marked in the dashed rectangle), shown for the bending wave (*G*) and fast wave (*H*). The right sides show how the wave fronts evolve with time. 35

2.6 Geometry of the biomechanical model from a side view (left) and top view (right). Gray represents the muscle shell domain, while the enclosed fluid is shown as purple. 38

2.7 Different behaviors simulated by the model. (*A*) contraction (*B*) elongation (*C*) nodding (*D*) bending. 39

2.8 Pipeline of the simulation from neural activity to behaviors. (*A-B*) NGCaMP fluorescence trace: stars mark estimated times of neural firing (*A*) and consequently, stimulation times for the model (*B*). (*C-D*) Averaged $[Ca^{2+}]_i$ and fluorescence intensities in ectoderm and endoderm (*C*) and $[Ca^{2+}]_i$ patterns of some moments (*D*). (*E-F*) Averaged active stress in ectoderm and endoderm (*E*) and stress patterns of some moments (*F*). (*G-H*) Comparison between length evolution of the model and from a *Hydra* (*G*) recording and some stills of the final simulated behaviors from the model (*H*). 40

2.9 Modeled calcium activation pattern under sequential stimulation of the fast pathways of randomly chosen 2×2 groups of muscle cells in the body column with no gap junctional electrical conductance. 43

2.10 Pipeline of the video analysis. 50

S1 Calcium fluxes (A) and ion currents (B), respectively correspond to Fig. 3A and Fig. 3B in the main text. 74

S2 Cell counting and length measurement in a small *Hydra*. Green circles are the counts in longitudinal direction and red colors are the counts in circumferential direction. 75

S3 Observables of $[Ca^{2+}]$ propagation change with different stimulation strengths of the slow wave (A - C) and the fast wave (D - F), including the distribution of maximum concentration (amplitude) over longitudinal index (A, D), the arrival time of peaks versus the longitudinal index (B, E) and the wavefront index change over time (C, F). 76

S4 Effects of gap-junctional coupling coefficients on wave propagation. (A) The effect of g_{IP_3} on the longitudinal range of the slow wave. (B) The effect of g_{IP_3} on the circular range of the slow wave. (C) The effect of g_c on the longitudinal propagation speed of the fast wave. (D) The effect of g_c on the circular propagation speed of the fast wave. 77

S5 Effects of intracellular parameters on wave propagation. (A) Effects of sweeping k_{IPR} and k_{deg} on the longitudinal range of the slow wave. (B) Effects of sweeping k_{SERCA} and k_{PMCA} on the longitudinal range of the slow wave. (C) Effects of sweeping g_{Ca} and g_K on the longitudinal propagation speed of the fast wave. 78

S6 Simulation following another video where two bursts are consecutive. (A) whole-frame fluorescence trace and neural firing moments; (B) comparison between length evolution of the model and the real *Hydra* in the video. . . . 79

S7 Effect on the length change by sweeping different parameters: (A) Endodermal c_{half}; (B) Endodermal k_7; (C) Endodermal K_F; (D) relaxation time (representing viscosity). 80

S8 Spatiotemporal pattern of the impulse response of the longitudinal center-line points in the biophysical model and Green's function. (A) Biophysical model response to a fast pathway stimulation. (B) Biophysical model response to a slow pathway stimulation. (C) Green's function of the fast wave. (D) Green's function of the slow wave. 81

S9 Nonlinearity exhibited by the interaction of two pointwise-stimulated fast waves. (A) Traces showing how $[Ca^{2+}]_i$ evolves, in which each curve represents a time point. (B) Snapshot of the muscle sheet at 25 ms after the stimulation, in which two waves cancel each other at the middle. 82

3.1 Conceptual scheme of the biological process described by the model, where colors in the muscle region represent the intensity of muscle stress. (A) Cross-section of *Hydra* body: water is constantly absorbed from outside into cell tissues and vacuoles due to the osmotic gradient; (B) when the resulting muscle stress increases over a threshold, it triggers the firing of neurons through mechanosensitive channels; (C) neural excitation stimulates muscle contraction of the whole body, which briefly further increases muscle stress and also extrudes water, reducing pressure and restoring the state to A. 90

3.2 Stress dependence of open probability (P_o) and firing frequency (f). 94

3.3 Simulation results of the model. (A) the trace of membrane potential; (B) traces of active and water stress; (C) the trajectory depicted as a curve on the (σ_a, σ_w) plane. 96

3.4 Inter-spike intervals (ISI) from our model (blue line) and calcium imaging videos (dim lines). Boxplots show the means and standard deviations of experimental ISI. 97

3.5 Relation between the neural activity and k_{in}. (A - D) Plots of how frequency of bursts (A), pulse number per cycle (B), duration of a burst (C) and frequency of pulses in a burst (D) vary with k_{in}. (E) Example firing patterns of $k_{\text{in}} = 5, 25, 50$ and 100. 98

3.6 Effects of k_a and k_e on the firing pattern. (A - D) Log-scale phase diagrams of frequency of bursts (A), pulses number per cycle (B), duration of a burst (C) and frequency of pulses in a burst (D), where the neuron is showing a bursting pattern in colored region and a spiking pattern in uncolored region. (E) Example firing patterns corresponding to the markers in plot A. 100

3.7 Spike trains of neurons in random networks with $g_c = 0$ and 200 nS, where x-axis represents time and each row along the y-axis represents the spike train of each neuron. 101

3.8 Spike trains of neural responses to external stimulation, where red arrows indicate times of stimulation and gray arrows the start time of the first burst of spontaneous activity without stimulation. (A) Spontaneous activity; (B) electrically stimulated; (C) mechanically stimulated. 102

4.1 Conducting paths indicated by the split-body experiments [131]. 115

4.2 Layout of the longitudinal-biased neural network model for CB net. 117

4.3 Spike trains from running simulation on the CB network model. Each index denotes a single CB neuron, increasing from top to bottom in a counterclockwise manner. 118

4.4 Models that are cut in different ways. (A) H-shape; (B) I-shape. 118

4.5 Comparisons between simulation results (bottom) and experimental recordings in [131] (top) under different cut preparations. Arrow heads marked with A, B in the top figures represent electrode placements. 119
4.6 Layout of the mutual inhibition network model consisting of CB (blue, pacemakers are not highlighted here) and RP (orange) neurons. (A) Connectivity in CB net; (B) connectivity in RP net; (C) inhibitory synapses from CB to RP; (D) synapses from RP to CB. 120
4.7 Simulation results of the mutual inhibition network. (A) Spiking trains of neurons in CB net; (B) spiking trains of neurons in RP net. 122
4.8 Fluorescence and behavior during regeneration of bisected *Hydra*. RP events are marked by black X's and CB events are marked by red X's. (A) Prebisection baseline data; (B-C) 0 hr after bisection; (D-E) 48 hr after bisection; (F-G) 72 hr after bisection. 123
4.9 Statistical analysis from bisection experiments. (A) Distribution of CB frequency; (B) distribution of RP frequency; (C) comparison between hypostomal and peduncular halves over time. 124
4.10 Design of bisecting the model. (A) Cut of CB $\rightarrow$ RP synapses; (B) cut of RP $\rightarrow$ CB synapses. 125
4.11 Simulation results of the bisected model. (A) CB spiking trains at hypostomal half; (B) RP spiking trains at hypostomal half; (C) CB spiking trains at the peduncular half; (D) RP spiking trains at the peduncular half. 125
4.12 Layout (A-D) and results (E-F) of the simulation of the peduncle half regeneration, where z represents the cut position, n_{pm} represents the number of CB pacemakers, and conn_scale represents the scale of connectivity probability on newly added neurons. 126

LIST OF TABLES

Table Number Page

S1 Parameters used in the single cell model 83
S2 Parameters used in the modified Hai-Murphy model 84
S3 Parameters used in the COMSOL model 85
S4 COMSOL solver configurations 86
S5 Parameters of Green's function after fitting 87
3.1 Parameters used in the model. 104
4.1 Parameters for single CB / RP neurons. 128

ACKNOWLEDGMENTS

First, I wish to express my sincere thanks to my advisor Adrienne Fairhall for her sustained support, encouragement, inspiration and patience during my PhD journey. Adrienne not only guided me into the research world of computational neuroscience with her rich knowledge and experience, but also shaped me into a better person with her strong enthusiasm in both work and life, and her kindness towards everyone.

I would like to thank all members of my supervisory committee, Marcel den Nijs, Eric Shea-Brown, Armita Nourmohammad and Boris Blinov for their time and insightful comments on my work.

I then would like to thank all of my collaborators: Joshua Swore, John Szymanski, Wataru Yamamoto, Shashank Sharma, Martha Bosma, Thomas Daniel, Rafael Yuste, Michael Regnier, Robert Steele, Celina Juliano and Jacob Robinson. The work in this dissertation would be impossible without their valuable advice and discussion.

Also, I would like to thank all members in our computational neuroscience center: Alison Duffy, Rich Pang, Yoni Browning, Kenneth Latimer, Scott Sterret, David Bell, John Ferré, Leenoy Meshulam, Fereshteh Lagzi, Patrick Zhang, Stefano Recanatesi, Jianghong Shi, Hannah Choi, Gabrielle Gutierrez, Alison Weber, Matthew Farrell, Helena Liu, Doris Voina, Daniel Zdeblick, Monica Liu, Ziyu Lu, Ryan Raut, Praveen Venkatesh, Po-Chen Kuo, Prof. Edgar Walker, and all other people that ever rotated or visited here. Their intense discussions and communications build our center into a close community that makes our research life colorful and cheering.

Finally, I want to say thanks to my friends, for sharing experiences and enjoying the life together; to my parents, for their unconditional love and understanding; to Yue, for our nine years of companionship with each other.

Chapter 1

INTRODUCTION

How do behaviors arise from neural activity? This is one of the most fundamental questions in neuroscience. Small model systems pose the opportunity to develop complete models for the neural dynamics and its control of behavior. *Hydra* is a small freshwater Cnidarian that has served as a fruitful model system for more than 270 years [41] since the early studies by Abraham Trembley [106]. With its robustness to external perturbations, transparent body column, permitting optical recording of neuronal activity, and rather simple nervous system, *Hydra* serves as a perfect system for us to study and build comprehensive computational models to explain the dynamics of its neural circuits and how its neural activity generates muscle movement and behavior on a whole-animal scale. In this dissertation, I'll introduce different models for *Hydra* that respectively explain the transformation of its neural drive to muscle dynamics and behaviors (chapter 2), the mechanisms underlying the bursting dynamics of its CB neurons (chapter 3), and the synchronization of its neural network (chapter 4). Our models in combination together capture mechanisms at every stage from neuron to muscle to contractile behavior in *Hydra*, and will likely inspire and inform study of the neural control of behaviors in other species.

1.1 Introduction to Hydra

1.1.1 Anatomy

Hydra's body column, with an oral region surrounded by tentacles located on its hypostome, and a basal aboral region called the peduncle used for anchoring Figure 1.1. The body column is a two-layered structure consisting of ectodermal and endodermal epithelia separated by an acellular matrix layer called the mesoglea. The two epithelia and mesoglea form a lay-

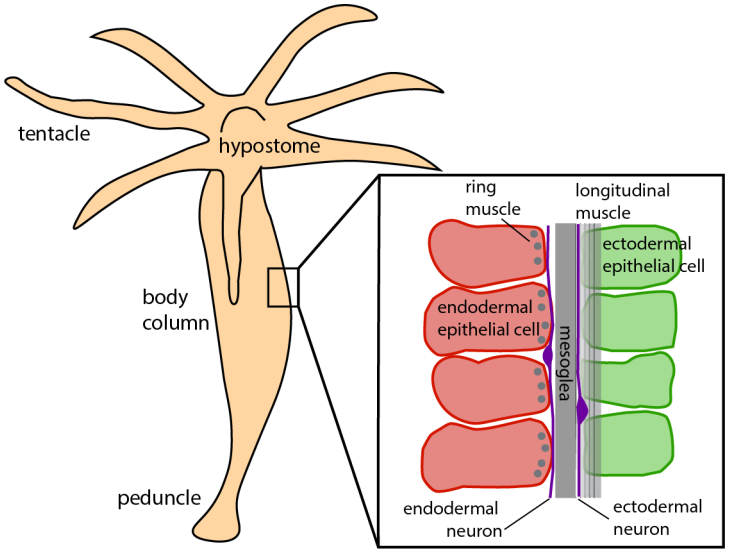

Figure 1.1: Simplified *Hydra* anatomy, adapted from [102].

ered body wall throughout the entire polyp enclosing a gastric cavity within, and together constitute a hydrostatic skeleton [63, 71, 102]. Epitheliomuscular cells are found to be multifunctional and play many different roles for *Hydra* [99], including metabolism, excretion, respiration and osmoregulation [11]. Muscle fibres run longitudinally in the ectoderm and circumferentially in the endoderm through myonemes, and their orthogonal contractions contribute to generate all motions and behaviors in *Hydra* [99]. Gap junctions are found between neurons, between epitheliomuscular cells, and between neurons and epitheliomuscular cells [111]. In the epithelia, gap junctions connect the adjacent epitheliomuscular cells within each layer, and also connect cells in separate layers by penetrating the mesoglea [92] (Figure 1.2). The epithelia has been shown to be excitable and can conduct electrical signals, through electrophysiological experiments on both normal [57, 58, 61, 60, 89, 4] and nerve-free *Hydra* [17, 72]. Neurons of several types are interspersed between the epithelial cells (Figure 1.1), and neuromuscular synaptic connectivity has been observed by electron microscopy [64].

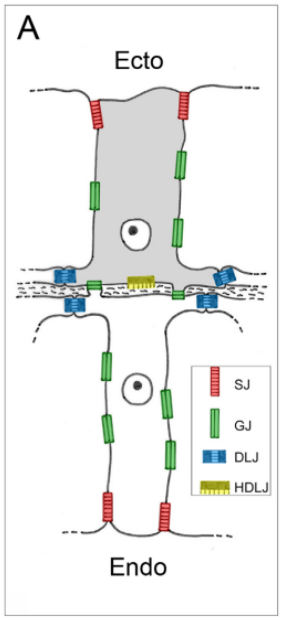

Figure 1.2: Gap junction connectivity between epitheliomuscular cells in epithelia, reproduced from [92].

1.1.2 Nervous system

Hydra has a nervous system that is composed of hundreds to thousands of neurons, with no centralized brain but instead a diffuse nerve net [28]. Early extracellular recordings reported multiple types of electrical activity in *Hydra* such as contraction bursts (CB), rhythmic potentials (RP) and prelocomotion bursts (PLB) [80, 81, 82, 83]. However, these studies can neither clearly distinguish electrical signals from neurons with those from muscle cells, nor accurately locate neurons over the *Hydra* body. Recent genetic advances using recently developed *Hydra* genetic lines that express the calcium indicator GCaMP6 has enabled the observation and identification of neural activities at higher resolution. With such calcium imaging techniques, at least three non-overlapping neural circuits have been identified and located: CB, located in the ectoderm over the whole body column but concentrated at the peduncle (peduncle ring); RP1, located in the ectoderm; and RP2, located in the endoderm [36] (Figure 1.3). CB neurons spontaneously exhibit periodic bursting activity, accompanying the contraction bursts motions of *Hydra*; RP neurons (RP1 and RP2) exhibit a rhythmic firing activity, but until now no persuasive quantitative evidence shows that RP

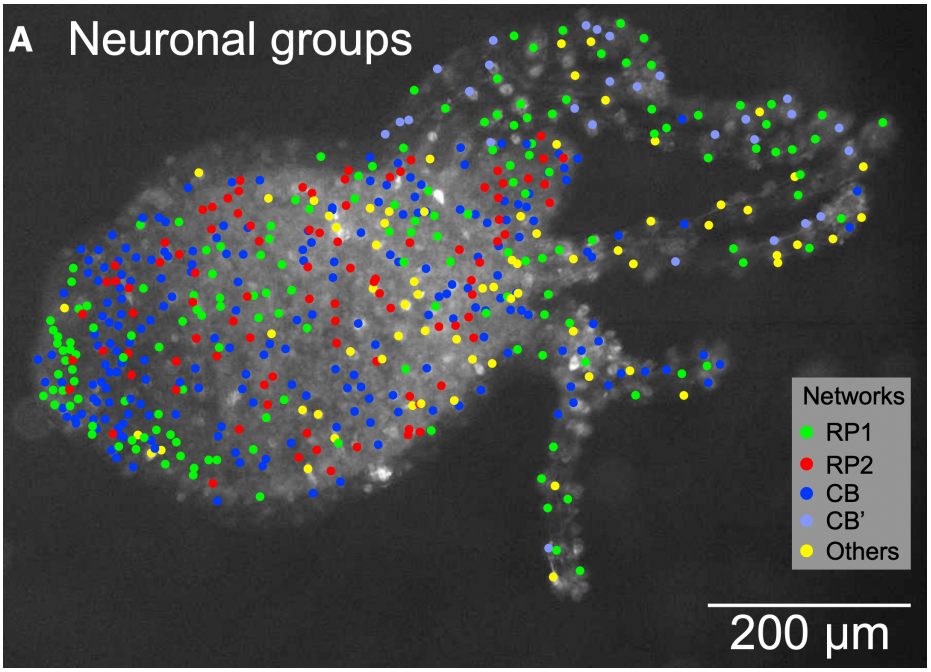

Figure 1.3: Topographical distribution of neurons in *Hydra*, reproduced from [36].

neurons have a direct correlation with behavior consistent with direct muscle activation [36, 6]. The global activation of the CB network is recorded to be initiated from the tentacles and the hypostomal end, propagating downwards to the foot through electrical coupling at a speed of centimeters per second [82, 57, 58, 60]. The activities of CB and RP1 have been shown to be slightly anticorrelated, suggesting that a potential mutual or one-way inhibition may exist between them [36, 80, 79, 100, 101].

1.1.3 Behaviors and muscle activity

Hydra exhibits a variety of well-characterized behaviors including longitudinal contraction, elongation, bending, nodding, tentacle movements, and some compound behaviors such as somersaulting, mouth opening and feeding [99, 46, 24]. Using calcium imaging of the muscle layers in *Hydra*, Szymanski and Yuste [99] observe that a specific spatiotemporal pattern of the muscle activity, either global or local, drives each behavior. These muscle activities have two distinct forms: a rapid global activation that drives whole-body contraction, and slow

local propagating waves of activation, which can be classified as body column waves, bending waves, nodding waves and mouth opening waves, depending on the initiation location and behaviors with which they are correlated. These observations suggest that the dynamics of the muscle layer itself forms an important and nontrivial component of the transformation from nerve firing to behavior.

1.1.4 Responses to environment and external stimuli

Behaviors and corresponding neural activity of *Hydra* have been shown to have a apparent correlation with some environmental factors and to be sensitive to external stimuli. Light stimuli directly inhibit CB pacemakers, and increase RP firing frequency when stimuli are on the entire *Hydra* body or locally on its base region. After repeated interruptions, CB's firing frequency is drastically increased, and its light response is decreased [80, 82, 83, 91, 88]. Both single electric shocks and strong mechanical stimulation can cause single contractions but markedly reduce endogenous CB activity thereafter, while enhancing the RP activity for a long time [82, 83, 91, 7]. CB frequence is influenced by external osmolarity; increased osmolarity decreases the frequency of CBs, suggesting that CB may be driven by the need for water regulation, potentially via mechanosensory feedback [12, 114]. A model based on this hypothesis to explain the bursting dynamics of CB will be introduced in this dissertation. Other factors such as food, temperature and glutathione, a nutritional extract, are also found to affect neural activity and behaviors [82, 83, 107, 88, 90].

1.2 Models of calcium dynamics

In almost every cell type, the concentration of cytosolic Ca^{2+} exhibits complex spatiotemporal behaviors. as intracellular oscillations with a time constant ranging from seconds to minutes, which can be organized into intercellular calcium waves [32]. Such calcium dynamics plays important roles in many physiological processes, including signal conduction, regulation of energy balance and coordination of muscle contraction [2, 42]. Hence there is a rich literature of mathematical modeling to quantitatively characterize these dynamics and their function.

Models of calcium dynamics include both models of nonexcitable cells, where cytosolic Ca^{2+} tends to be independent of the cell membrane potential, and excitable cells, where Ca^{2+} dynamics is usually strongly linked to Ca^{2+} through voltage-gated channels and thus the membrane potential [32].

1.2.1 Nonexcitable cells

Calcium dynamics of nonexcitable cells often share a toolbox of biophysical mechanisms that includes some common components, such as:

- a G protein-coupled receptor (GPCR) which binds an agonist and initiates the Ca^{2+} signaling pathway [75];
- the sarco/endoplasmic reticulum Ca^{2+}-ATPase (SERCA) which transports calcium from the cytosol to the sarcoplasmic reticulum (SR) or endoplasmic reticulum (ER) [76];
- the plasma membrane Ca^{2+} ATPase (PMCA) which removes calcium from the cell [56];
- internal calcium channels which release calcium from the ER/SR to the cytosol, including inositol trisphosphate receptor (IPR) which is activated by IP_3 [77], and ryanodine receptor (RyR) which is inhibited by the alkaloid ryanodine [37].

All these components have been modeled at levels ranging from simplified to very complex mathematical models. A relatively simple model including these elements (Figure 1.4) can be formulated as Equation 1.1 [32]

$$\begin{aligned} \frac{\mathrm{d}c}{\mathrm{d}t} &= J_{\mathrm{IPR}} + J_{\mathrm{leak}} - J_{\mathrm{serca}} + J_{\mathrm{in}} - J_{\mathrm{pm}} \\ \frac{\mathrm{d}c_e}{\mathrm{d}t} &= \gamma(-J_{\mathrm{IPR}} - J_{\mathrm{leak}} + J\mathrm{serca}) \end{aligned} \tag{1.1}$$

where c and c_e denote the Ca^{2+} concentrations in the cytoplasm and ER respectively, γ denotes the volume ratio between cytoplasm and ER, and J_x denotes the influxes of Ca^{2+} through specific channels/pumps.

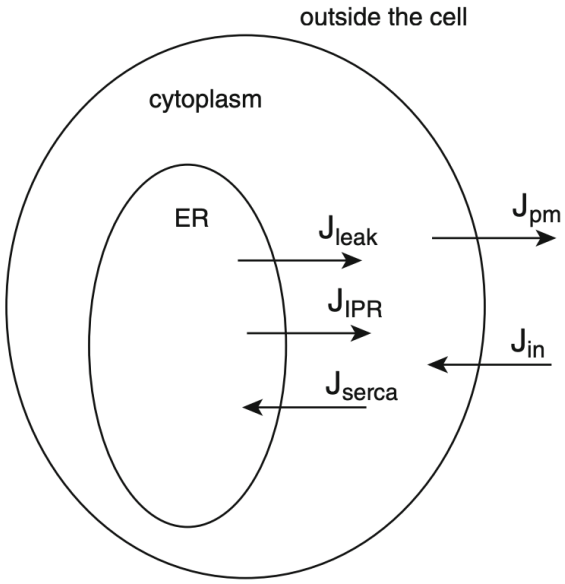

Figure 1.4: A simple model of Ca^{2+} signaling, reproduced from [32].

Specific models have been built for various types of nonexcitable cells, such as *Xenopus* oocytes [5, 39, 108, 40], hepatocytes [27, 69, 67, 33], pancreatic and parotid acinar cells [70, 94, 93], astrocytes [34, 62, 29], and smooth muscle cells [109, 26, 23, 113, 44, 59], with different detailed components and parameter sets depending on their specific physiological structures and recordings.

1.2.2 Excitable cells

In excitable cells, Ca^{2+} dynamics is strongly coupled with the membrane potential, which affects the driving force for Ca^{2+} entry by opening and closing voltage-gated Ca^{2+} channels. Dynamics of membrane potential is commonly modeled by the classic cell circuit diagram following Hodgkin and Huxley as Equation 1.2 [49]

$$C_m \frac{\mathrm{d}V}{\mathrm{d}t} + \sum I_{\text{ionic}} = 0 \tag{1.2}$$

where V denotes membrane potential, C_m is the capacitance of the cell membrane, and the sum is over all ionic currents across the cell membrane.

The Ca^{2+} dynamics can be formulated as Equation 1.3 [32]

$$\frac{dc}{dt} = -\frac{I_{Ca}}{2Fw} + \sum \text{all other } Ca^{2+} \text{ fluxes} \tag{1.3}$$

where c denotes the cytosolic Ca^{2+} concentration, I_{Ca} denotes the flux through the voltage-gated Ca^{2+} channel, F is the Faraday's constant, and w is the volume of the cell.

Previous studies have built numerous models for different types of excitable cells, such as cardiac muscle cells [74, 96, 112, 48, 45], skeletal muscle cells [22, 8, 9, 10, 73], and uterine muscle cells [85, 104, 25, 115, 103].

1.2.3 Intercellular calcium waves

Calcium dynamics can travel between cells and form intercellular calcium waves. Depending on their propagation speed and range, these can be classified as slow diffusive or wave-form propagation in a local region, or a fast propagating calcium synchronization which is usually regenerative and global [31, 87]. These waves commonly propagate through gap junctions, which can not only diffuse Ca^{2+} and the second messenger IP_3, but also serve as pathways for electrical coupling of membrane potentials [52].

Although some previous models assume that the calcium wave depends on the diffusion of Ca^{2+} through gap junctions [50], the effect of Ca^{2+} diffusion has been shown to be very small and generally negligible due to the heavy buffering of Ca^{2+} [55]. Instead, gap-junctional diffusion of IP_3 is considered to be the major drive in the propagation of slow calcium waves, and has been adopted in many previous models [95, 35, 51, 65, 43].

Other models focus on the electrical coupling property of gap junctions and have successfully simulated fast calcium synchronization [53, 68, 66].

1.3 Models of bursting

Bursting is a firing pattern of neurons whereby rapid spike sequences are followed by quiescent periods. In his book *Dynamical Systems in Neuroscience*, Eugene Izhikevich pointed out a common fast-slow dynamics underlying bursting: a bursting pattern consists of two dynamics with different time scales: a fast spiking oscillation within each single burst (*in-*

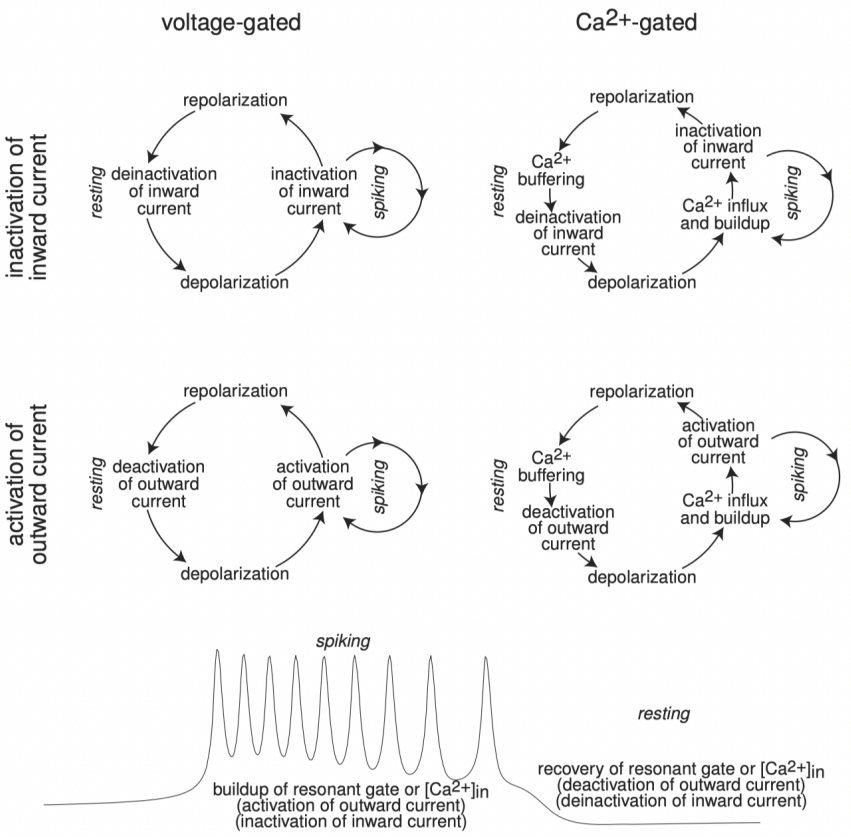

Figure 1.5: Four major classes of bursting models that are based on ionic mechanisms, reproduced from [54]

*tra*burst oscillation), and a slow modulating oscillation over bursts (*inter*burst oscillation). These are typically due to the interplay of two interacting processes: a fast process that initiates and sustains the firing of the neuron, and a slow process that slowly accumulates a signal that eventually terminates the firing [54].

Previous models typically focus on ionic mechanisms to explain this fast-slow dynamics, which can be grouped into four major classes: voltage-gated inactivation of an inward current [16, 78, 30], voltage-gated activation of an outward current [110, 16], Ca^{2+}-gated inactivation of an inward current[3, 47, 21], and Ca^{2+}-gated activation of an outward current [105, 98, 3, 47] (Figure 1.5).

Specifically, CB neurons of *Hydra* exhibit a "circle/circle" or "parabolic" bursting pattern, where the interspike intervals decrease then increase during each burst, taking a form

of parabola [38, 97]. Parabolic bursting is a prominent feature of the ganglion R_{15} neurons of the mollusk *Aplysia*, which has been well studied by numerous modeling studies [84, 1, 86, 20, 21, 13, 14, 18, 19, 15, 116]. These models of parabolic bursting can be reduced to some canonical forms. For instance, if the equilibrium of the slow subsystem is a stable focus, the canonical model Equation 1.4 [54] has the following form:

$$\begin{aligned} \dot{v} &= I + v^2 + u_1, \\ \dot{u}_1 &= -\mu_1 u_2, \\ \dot{u}_2 &= -\mu_2(u_2 - u_1), \end{aligned} \tag{1.4}$$

where v denotes the re-scaled membrane potential of the neuron, u_1 and u_2 are variables that represent a slow amplifying process that facilitates the firing of the neuron and a resonant process that provides negative feedback, respectively.

Due to the specific features of the *Hydra* CB firing pattern, such as its extremely large interspike intervals, its high irregularity, and its strong correlation with the environment, we build a model for it by assuming that the slow processes come from the osmolarity-driven muscle stress change instead of the typical ionic mechanisms. Details will be introduced in chapter 3.

Bibliography

[1] WB Adams. Slow depolarizing and hyperpolarizing currents which mediate bursting in aplysia neurone r15. *The Journal of physiology*, 360(1):51–68, 1985.

[2] Gregory C Amberg and Manuel F Navedo. Calcium dynamics in vascular smooth muscle. *Microcirculation*, 20(4):281–289, 2013.

[3] B Amini, JW Clark Jr, and CC Canavier. Calcium dynamics underlying pacemaker-like and burst firing oscillations in midbrain dopaminergic neurons: a computational study. *Journal of Neurophysiology*, 82(5):2249–2261, 1999.

[4] Peter AV Anderson. Epithelial conduction: its properties and functions. *Progress in neurobiology*, 15(3):161–203, 1980.

[5] Alireza Atri, Jeff Amundson, David Clapham, and James Sneyd. A single-pool model for intracellular calcium oscillations and waves in the xenopus laevis oocyte. *Biophysical Journal*, 65(4):1727–1739, 1993.

[6] Krishna N Badhiwala, Daniel L Gonzales, Daniel G Vercosa, Benjamin W Avants, and Jacob T Robinson. Microfluidics for electrophysiology, imaging, and behavioral analysis of hydra. *Lab on a Chip*, 18(17):2523–2539, 2018.

[7] Krishna N Badhiwala, Abby S Primack, Celina Juliano, and Jacob T Robinson. Multiple neuronal networks coordinate hydra mechanosensory behavior. *bioRxiv*, pages 2020–10, 2021.

[8] SM Baylor and S Hollingworth. Model of sarcomeric ca2+ movements, including atp ca2+ binding and diffusion, during activation of frog skeletal muscle. *The Journal of general physiology*, 112(3):297–316, 1998.

[9] SM Baylor, S Hollingworth, and WK Chandler. Comparison of simulated and measured calcium sparks in intact skeletal muscle fibers of the frog. *The Journal of general physiology*, 120(3):349–368, 2002.

[10] Stephen M Baylor and Stephen Hollingworth. Intracellular calcium movements during excitation–contraction coupling in mammalian slow-twitch and fast-twitch muscle fibers. *Journal of General Physiology*, 139(4):261–272, 2012.

[11] Dale J Benos and Robert D Prusch. Osmoregulation in fresh-waterhydra. *Comparative Biochemistry and Physiology Part A: Physiology*, 43(1):165–171, 1972.

[12] Dale J Benos and Robert D Prusch. Osmoregulation in hydra: Column contraction as a function of external osmolality. *Comparative Biochemistry and Physiology Part A: Physiology*, 44(4):1397–1400, 1973.

[13] Richard Bertram. A computational study of the effects of serotonin on a molluscan burster neuron. *Biological Cybernetics*, 69(3):257–267, 1993.

[14] Richard Bertram. Reduced-system analysis of the effects of serotonin on a molluscan burster neuron. *Biological cybernetics*, 70(4):359–368, 1994.

[15] Robert J Butera, John W Clark, Carmen C Canavier, Douglas A Baxter, and John H Byrne. Analysis of the effects of modulatory agents on a modeled bursting neuron: Dynamic interactions between voltage and calcium dependent systems. *Journal of computational neuroscience*, 2(1):19–44, 1995.

[16] Robert J Butera Jr, John Rinzel, and Jeffrey C Smith. Models of respiratory rhythm generation in the pre-botzinger complex. i. bursting pacemaker neurons. *Journal of neurophysiology*, 82(1):382–397, 1999.

[17] RD Campbell, RK Josephson, WE Schwab, and NB Rushforth. Excitability of nerve-free hydra. *Nature*, 262(5567):388–390, 1976.

[18] CC Canavier, DA Baxter, JW Clark, and JH Byrne. Nonlinear dynamics in a model neuron provide a novel mechanism for transient synaptic inputs to produce long-term alterations of postsynaptic activity. *Journal of neurophysiology*, 69(6):2252–2257, 1993.

[19] CC Canavier, DA Baxter, JW Clark, and JH Byrne. Multiple modes of activity in a model neuron suggest a novel mechanism for the effects of neuromodulators. *Journal of neurophysiology*, 72(2):872–882, 1994.

[20] CC Canavier, JW Clark, and JH Byrne. Routes to chaos in a model of a bursting neuron. *Biophysical journal*, 57(6):1245–1251, 1990.

[21] CC Canavier, JW Clark, and JH Byrne. Simulation of the bursting activity of neuron r15 in aplysia: role of ionic currents, calcium balance, and modulatory transmitters. *Journal of Neurophysiology*, 66(6):2107–2124, 1991.

[22] MB Cannell and DG Allen. Model of calcium movements during activation in the sarcomere of frog skeletal muscle. *Biophysical Journal*, 45(5):913–925, 1984.

[23] Pengxing Cao, Xiahui Tan, Graham Donovan, Michael J Sanderson, and James Sneyd. A deterministic model predicts the properties of stochastic calcium oscillations in airway smooth muscle cells. *PLoS computational biology*, 10(8):e1003783, 2014.

[24] Jason A Carter, Callen Hyland, Robert E Steele, and Eva-Maria S Collins. Dynamics of mouth opening in hydra. *Biophysical journal*, 110(5):1191–1201, 2016.

[25] Amy L Cochran and Yingxin Gao. A model and simulation of uterine contractions. *Mathematics and Mechanics of Solids*, 20(5):540–564, 2015.

[26] Huguette Croisier, Xiahui Tan, Jose F Perez-Zoghbi, Michael J Sanderson, James Sneyd, and Bindi S Brook. Activation of store-operated calcium entry in airway smooth muscle cells: insight from a mathematical model. *PloS one*, 8(7):e69598, 2013.

[27] KSR Cuthbertson and TR Chay. Modelling receptor-controlled intracellular calcium oscillators. *Cell calcium*, 12(2-3):97–109, 1991.

[28] Charles N David. A quantitative method for maceration of hydra tissue. *Wilhelm Roux'Archiv für Entwicklungsmechanik der Organismen*, 171(4):259–268, 1973.

[29] Audrey Denizot, Misa Arizono, U Valentin Nägerl, Hédi Soula, and Hugues Berry. Simulation of calcium signaling in fine astrocytic processes: Effect of spatial properties on spontaneous activity. *PLoS computational biology*, 15(8):e1006795, 2019.

[30] Alain Destexhe, Diego Contreras, Terrence J Sejnowski, and Mircea Steriade. A model of spindle rhythmicity in the isolated thalamic reticular nucleus. *Journal of neurophysiology*, 72(2):803–818, 1994.

[31] Genevieve Dupont, Laurent Combettes, and Luc Leybaert. Calcium dynamics: spatio-temporal organization from the subcellular to the organ level. *International review of cytology*, 261:193–245, 2007.

[32] Geneviève Dupont, Martin Falcke, Vivien Kirk, and James Sneyd. *Models of calcium signalling*, volume 43. Springer, 2016.

[33] Geneviève Dupont, O Koukoui, C Clair, Christophe Erneux, Stéphane Swillens, and Laurent Combettes. Ca2+ oscillations in hepatocytes do not require the modulation of insp3 3-kinase activity by ca2+. *FEBS letters*, 534(1-3):101–105, 2003.

[34] Geneviève Dupont, Emmanuel Fabrice Loomekandja Lokenye, and RA John Challiss. A model for ca2+ oscillations stimulated by the type 5 metabotropic glutamate receptor: an unusual mechanism based on repetitive, reversible phosphorylation of the receptor. *Biochimie*, 93(12):2132–2138, 2011.

[35] Geneviève Dupont, THIERRY TORDJMANN, Caroline Clair, Stéphane Swillens, MICHEL CLARET, and Laurent Combettes. Mechanism of receptor-oriented intercellular calcium wave propagation in hepatocytes. *The FASEB Journal*, 14(2):279–289, 2000.

[36] Christophe Dupre and Rafael Yuste. Non-overlapping neural networks in hydra vulgaris. *Current Biology*, 27(8):1085–1097, 2017.

[37] Makoto Endo, Minoru Tanaka, and Yasuo Ogawa. Calcium induced release of calcium from the sarcoplasmic reticulum of skinned skeletal muscle fibres. *Nature*, 228(5266):34–36, 1970.

[38] G Bard Ermentrout and Nancy Kopell. Parabolic bursting in an excitable system coupled with a slow oscillation. *SIAM journal on applied mathematics*, 46(2):233–253, 1986.

[39] M Falcke, JL Hudson, P Camacho, and James D Lechleiter. Impact of mitochondrial ca2+ cycling on pattern formation and stability. *Biophysical Journal*, 77(1):37–44, 1999.

[40] Christopher P Fall, John M Wagner, Leslie M Loew, and Richard Nuccitelli. Cortically restricted production of ip3 leads to propagation of the fertilization ca2+ wave along the cell surface in a model of the xenopus egg. *Journal of theoretical biology*, 231(4):487–496, 2004.

[41] Brigitte Galliot. Hydra, a fruitful model system for 270 years. *International Journal of Developmental Biology*, 56(6-7-8):411–423, 2012.

[42] Carlotta Giorgi, Alberto Danese, Sonia Missiroli, Simone Patergnani, and Paolo Pinton. Calcium dynamics as a machine for decoding signals. *Trends in cell biology*, 28(4):258–273, 2018.

[43] Mati Goldberg, Maurizio De Pittà, Vladislav Volman, Hugues Berry, and Eshel Ben-Jacob. Nonlinear gap junctions enable long-distance propagation of pulsating calcium waves in astrocyte networks. *PLoS computational biology*, 6(8), 2010.

[44] Jose M Gonzalez-Fernandez and Bard Ermentrout. On the origin and dynamics of the vasomotion of small arteries. *Mathematical biosciences*, 119(2):127–167, 1994.

[45] Joseph L Greenstein and Raimond L Winslow. Integrative systems models of cardiac excitation–contraction coupling. *Circulation research*, 108(1):70–84, 2011.

[46] Shuting Han, Ekaterina Taralova, Christophe Dupre, and Rafael Yuste. Comprehensive machine learning analysis of hydra behavior reveals a stable basal behavioral repertoire. *Elife*, 7:e32605, 2018.

[47] Ronald M Harris-Warrick and Robert E Flamm. Multiple mechanisms of bursting in a conditional bursting neuron. *Journal of Neuroscience*, 7(7):2113–2128, 1987.

[48] R Hinch, JL Greenstein, and RL Winslow. Multi-scale models of local control of calcium induced calcium release. *Progress in biophysics and molecular biology*, 90(1-3):136–150, 2006.

[49] Alan L Hodgkin and Andrew F Huxley. A quantitative description of membrane current and its application to conduction and excitation in nerve. *The Journal of physiology*, 117(4):500, 1952.

[50] Thomas Höfer, Antonio Politi, and Reinhart Heinrich. Intercellular ca2+ wave propagation through gap-junctional ca2+ diffusion: a theoretical study. *Biophysical journal*, 80(1):75–87, 2001.

[51] Thomas Höfer, Laurent Venance, and Christian Giaume. Control and plasticity of intercellular calcium waves in astrocytes: a modeling approach. *Journal of Neuroscience*, 22(12):4850–4859, 2002.

[52] JD Huizinga, LWC Liu, MG Blennerhassett, Lars Thuneberg, and A Molleman. Intercellular communication in smooth muscle. *Experientia*, 48(10):932–941, 1992.

[53] Mohammad S Imtiaz, Christopher P Katnik, David W Smith, and Dirk F van Helden. Role of voltage-dependent modulation of store ca2+ release in synchronization of ca2+ oscillations. *Biophysical journal*, 90(1):1–23, 2006.

[54] Eugene M Izhikevich. *Dynamical systems in neuroscience*. MIT press, 2007.

[55] M Saleet Jafri and Joel Keizer. Diffusion of inositol 1, 4, 5-trisphosphate but not ca2+ is necessary for a class of inositol 1, 4, 5-trisphosphate-induced ca2+ waves. *Proceedings of the National Academy of Sciences*, 91(20):9485–9489, 1994.

[56] Thomas P Jensen, Lucy E Buckby, and Ruth M Empson. Expression of plasma membrane ca2+ atpase family members and associated synaptic proteins in acute and cultured organotypic hippocampal slices from rat. *Developmental brain research*, 152(2):129–136, 2004.

[57] Robert K Josephson. Conduction and contraction in the column of hydra. *Journal of Experimental Biology*, 47(1):179–190, 1967.

[58] Robert K Josephson and Martin Macklin. Electrical properties of the body wall of hydra. *The Journal of General Physiology*, 53(5):638–665, 1969.

[59] Adam Kapela, Anastasios Bezerianos, and Nikolaos M Tsoukias. A mathematical model of ca2+ dynamics in rat mesenteric smooth muscle cell: agonist and no stimulation. *Journal of theoretical biology*, 253(2):238–260, 2008.

[60] G Kass-Simon. Longitudinal conduction of contraction burst pulses from hypostomal excitation loci inhydra attenuata. *Journal of comparative physiology*, 80(1):29–49, 1972.

[61] G KASSSIMON. Multiple excitation sites and straight-line conduction in contraction burst system of hydra. In *AMERICAN ZOOLOGIST*, 1970.

[62] Muhammad Uzair Khalid, Aapo Tervonen, Iina Korkka, Jari Hyttinen, and Kerstin Lenk. Geometry-based computational modeling of calcium signaling in an astrocyte. In *EMBEC & NBC 2017*, pages 157–160. Springer, 2017.

[63] William M Kier. The diversity of hydrostatic skeletons. *Journal of Experimental Biology*, 215(8):1247–1257, 2012.

[64] John C Kinnamon and Jane A Westfall. Types of neurons and synaptic connections at hypostome-tentacle junctions in hydra. *Journal of Morphology*, 173(1):119–128, 1982.

[65] Michèle Koenigsberger, Roger Sauser, Mathieu Lamboley, Jean-Louis Bény, and Jean-Jacques Meister. Ca2+ dynamics in a population of smooth muscle cells: modeling the recruitment and synchronization. *Biophysical journal*, 87(1):92–104, 2004.

[66] Michèle Koenigsberger, Dominique Seppey, Jean-Louis Bény, and Jean-Jacques Meister. Mechanisms of propagation of intercellular calcium waves in arterial smooth muscle cells. *Biophysical journal*, 99(2):333–343, 2010.

[67] Ursula Kummer, Lars F Olsen, C Jane Dixon, Anne K Green, Erich Bornberg-Bauer, and Gerold Baier. Switching from simple to complex oscillations in calcium signaling. *Biophysical journal*, 79(3):1188–1195, 2000.

[68] JMAM Kusters, WPM van Meerwijk, Dirk L Ypey, Alexander PR Theuvenet, and CCAM Gielen. Fast calcium wave propagation mediated by electrically conducted excitation and boosted by cicr. *American Journal of Physiology-Cell Physiology*, 294(4):C917–C930, 2008.

[69] Ann Zahle Larsen, Lars Folke Olsen, and Ursula Kummer. On the encoding and decoding of calcium signals in hepatocytes. *Biophysical chemistry*, 107(1):83–99, 2004.

[70] Andrew P LeBeau, David I Yule, Guy E Groblewski, and James Sneyd. Agonist-dependent phosphorylation of the inositol 1, 4, 5-trisphosphate receptor: a possible mechanism for agonist-specific calcium oscillations in pancreatic acinar cells. *The Journal of general physiology*, 113(6):851–872, 1999.

[71] Lucas Leclère and Eric Röttinger. Diversity of cnidarian muscles: function, anatomy, development and regeneration. *Frontiers in cell and developmental biology*, 4:157, 2017.

[72] J Lepault, AW McDowall, and CJP Grimmelikhuijzen. Intercellular junctions in nerve-free hydra. *Cell and tissue research*, 209(2):217–224, 1980.

[73] Weifan Liu and Sarah D Olson. Compartment calcium model of frog skeletal muscle during activation. *Journal of Theoretical Biology*, 364:139–153, 2015.

[74] Ching-hsing Luo and Yoram Rudy. A dynamic model of the cardiac ventricular action potential. i. simulations of ionic currents and concentration changes. *Circulation research*, 74(6):1071–1096, 1994.

[75] Louis M Luttrell. Transmembrane signaling by g protein-coupled receptors. *Transmembrane Signaling Protocols*, pages 3–49, 2006.

[76] David H MacLennan, William J Rice, and N Michael Green. The mechanism of ca2+ transport by sarco (endo) plasmic reticulum ca2+-atpases. *Journal of Biological Chemistry*, 272(46):28815–28818, 1997.

[77] Don-On Daniel Mak and J Kevin Foskett. Inositol 1, 4, 5-trisphosphate receptors in the endoplasmic reticulum: a single-channel point of view. *Cell calcium*, 58(1):67–78, 2015.

[78] David A McCormick and John R Huguenard. A model of the electrophysiological properties of thalamocortical relay neurons. *Journal of neurophysiology*, 68(4):1384–1400, 1992.

[79] CB McCullough. Pacemaker interaction in hydra. *American zoologist*, 5(3):499–504, 1965.

[80] LM Passano and CB McCullough. The light response and the rhythmic potentials of hydra. *Proceedings of the National Academy of Sciences of the United States of America*, 48(8):1376, 1962.

[81] LM Passano and CB McCullough. Pacemaker hierarchies controlling the behaviour of hydras. *Nature*, 199(4899):1174–1175, 1963.

[82] LM Passano and CB McCullough. Co-ordinating systems and behaviour in hydra: I. pacemaker system of the periodic contractions. *Journal of Experimental Biology*, 41(3):643–664, 1964.

[83] LM Passano and CB McCullough. Co-ordinating systems and behaviour in hydra ii. the rhythmic potential system. *Journal of Experimental Biology*, 42(2):205–231, 1965.

[84] Richard E Plant and M Kim. On the mechanism underlying bursting in the aplysia abdominal ganglion r15 cell. *Mathematical Biosciences*, 26(3-4):357–375, 1975.

[85] Sandy Rihana, Jeremy Terrien, Guy Germain, and Catherine Marque. Mathematical modeling of electrical activity of uterine muscle cells. *Medical & biological engineering & computing*, 47(6):665–675, 2009.

[86] John Rinzel and Young Seek Lee. Dissection of a model for neuronal parabolic bursting. *Journal of mathematical biology*, 25(6):653–675, 1987.

[87] Stephan Rohr. Role of gap junctions in the propagation of the cardiac action potential. *Cardiovascular research*, 62(2):309–322, 2004.

[88] Norman B Rushforth. Inhibition of contraction responses of hydra. *American zoologist*, 5(3):505–513, 1965.

[89] Norman B Rushforth. Behavioral and electrophysiological studies of hydra. i. analysis of contraction pulse patterns. *The Biological Bulletin*, 140(2):255–273, 1971.

[90] Norman B Rushforth and Donald S Burke. Behavioral and electrophysiological studies of hydra. ii. pacemaker activity of isolated tentacles. *The Biological Bulletin*, 140(3):502–519, 1971.

[91] Norman B Rushforth, Allison L Burnett, and Richard Maynard. Behavior in hydra: contraction responses of hydra pirardi to mechanical and light stimuli. *Science*, 139(3556):760–761, 1963.

[92] Anna Seybold, Willi Salvenmoser, and Bert Hobmayer. Sequential development of apical-basal and planar polarities in aggregating epitheliomuscular cells of hydra. *Developmental biology*, 412(1):148–159, 2016.

[93] J Sneyd, K Tsaneva-Atanasova, JIE Bruce, SV Straub, DR Giovannucci, and DI Yule. A model of calcium waves in pancreatic and parotid acinar cells. *Biophysical journal*, 85(3):1392–1405, 2003.

[94] James Sneyd, Andrew LeBeau, and David Yule. Traveling waves of calcium in pancreatic acinar cells: model construction and bifurcation analysis. *Physica D: Nonlinear Phenomena*, 145(1-2):158–179, 2000.

[95] JAMES Sneyd, BT Wetton, ANDREW C Charles, and MICHAEL J Sanderson. Intercellular calcium waves mediated by diffusion of inositol trisphosphate: a two-dimensional model. *American Journal of Physiology-Cell Physiology*, 268(6):C1537–C1545, 1995.

[96] Christian Soeller and Mark B Cannell. Analysing cardiac excitation–contraction coupling with mathematical models of local control. *Progress in biophysics and molecular biology*, 85(2-3):141–162, 2004.

[97] C Soto-Trevino, N Kopell, and D Watson. Parabolic bursting revisited. *Journal of mathematical biology*, 35(1):114–128, 1996.

[98] Ian M Stanford, Roger D Traub, and John GR Jefferys. Limbic gamma rhythms. ii. synaptic and intrinsic mechanisms underlying spike doublets in oscillating subicular neurons. *Journal of neurophysiology*, 80(1):162–171, 1998.

[99] John R Szymanski and Rafael Yuste. Mapping the whole-body muscle activity of hydra vulgaris. *Current Biology*, 29(11):1807–1817, 2019.

[100] Cloe Taddei-Ferretti and S Chillemi. Modulation of hydra attentuata rhythmic activity. *Biological cybernetics*, 56(4):225–235, 1987.

[101] Cloe Taddei-Ferretti and Carlo Musio. The neural net of hydra and the modulation of its periodic activity. In *International Work-Conference on Artificial Neural Networks*, pages 123–137. Springer, 1999.

[102] Ulrich Technau and Robert E Steele. Evolutionary crossroads in developmental biology: Cnidaria. *Development*, 138(8):1447–1458, 2011.

[103] Craig P Testrow, Arun V Holden, Anatoly Shmygol, and Henggui Zhang. A computational model of excitation and contraction in uterine myocytes from the pregnant rat. *Scientific reports*, 8(1):1–14, 2018.

[104] Wing-Chiu Tong, Cecilia Y Choi, Sanjay Karche, Arun V Holden, Henggui Zhang, and Michael J Taggart. A computational model of the ionic currents, ca2+ dynamics and action potentials underlying contraction of isolated uterine smooth muscle. *PloS one*, 6(4), 2011.

[105] Roger D Traub, Robert K Wong, Richard Miles, and Hillary Michelson. A model of a ca3 hippocampal pyramidal neuron incorporating voltage-clamp data on intrinsic conductances. *Journal of neurophysiology*, 66(2):635–650, 1991.

[106] Abraham Trembley. *Mémoires pour servir à l'histoire d'un genre de ploypes d'eau douce, à bras en forme de cornes*, volume 1. Durand, 1744.

[107] Constantine N Tzouanas, Soonyoung Kim, Krishna N Badhiwala, Benjamin W Avants, and Jacob T Robinson. Hydra vulgaris shows stable responses to thermal stimulation despite large changes in the number of neurons. *Iscience*, 24(6):102490, 2021.

[108] John Wagner, Yue-Xian Li, John Pearson, and Joel Keizer. Simulation of the fertilization ca2+ wave in xenopus laevis eggs. *Biophysical journal*, 75(4):2088–2097, 1998.

[109] Inga Y Wang, Yan Bai, Michael J Sanderson, and James Sneyd. A mathematical analysis of agonist-and kcl-induced ca2+ oscillations in mouse airway smooth muscle cells. *Biophysical journal*, 98(7):1170–1181, 2010.

[110] X-J Wang. Fast burst firing and short-term synaptic plasticity: a model of neocortical chattering neurons. *Neuroscience*, 89(2):347–362, 1999.

[111] Jane A Westfall, John C Kinnamon, and David E Sims. Neuro-epitheliomuscular cell and neuro-neuronal gap junctions inhydra. *Journal of neurocytology*, 9(6):725–732, 1980.

[112] George SB Williams, Gregory D Smith, Eric A Sobie, and M Saleet Jafri. Models of cardiac excitation–contraction coupling in ventricular myocytes. *Mathematical biosciences*, 226(1):1–15, 2010.

[113] AYK Wong and GA Klassen. A model of calcium regulation in smooth muscle cell. *Cell calcium*, 14(3):227–243, 1993.

[114] Wataru Yamamoto and Rafael Yuste. Whole-body imaging of neural and muscle activity during behavior in hydra vulgaris: effect of osmolarity on contraction bursts. *Eneuro*, 7(4), 2020.

[115] Maxime Yochum, Jérémy Laforêt, and Catherine Marque. An electro-mechanical multiscale model of uterine pregnancy contraction. *Computers in biology and medicine*, 77:182–194, 2016.

[116] Xintian Yu, John H Byrne, and Douglas A Baxter. Modeling interactions between electrical activity and second-messenger cascades in aplysia neuron r15. *Journal of neurophysiology*, 91(5):2297–2311, 2004.

Chapter 2

A COMPLETE BIOMECHANICAL MODEL OF HYDRA CONTRACTILE BEHAVIORS, FROM NEURAL DRIVE TO MUSCLE TO MOVEMENT

This chapter contains work done in collaboration with Dr. Joshua Swore, Mr. Shashank Sharma, Dr. John Szymanski, Dr. Rafael Yuste, Dr. Thomas Daniel, Dr. Michael Regnier, Dr. Martha Bosma and Dr. Adrienne Fairhall. We have submitted the following text for publication and it is currently under review. I wrote the following text and all of my collaborators contributed editing. In the course of this project, I implemented research, analyzed data, built the model and interpreted the results.

2.1 Abstract

How does neural activity drive muscles to produce behavior? The recent development of genetic lines in *Hydra* that allow complete calcium imaging of both neuronal and muscle activity, as well as systematic machine learning quantification of behaviors, makes this small cnidarian an ideal model system to understand and model the complete transformation from neural firing to body movements. As a first step to achieve this, we have built a neuromechanical model of *Hydra*'s fluid-filled hydrostatic skeleton, incorporating its neuronal activity, muscle activity and body column biomechanics. Our model is based on experimental measurements of neuronal and muscle activity, and assumes gap junctional coupling among muscle cells and calcium-dependent force generation by muscles. With these assumptions, we can robustly reproduce a basic set of *Hydra*'s behaviors. We can further explain puzzling experimental observations, including the dual timescale kinetics observed in muscle activation and the engagement of ecto- and endodermal muscle in different behaviors. This work delineates the spatiotemporal control space of *Hydra* movement and can serve as a template for future efforts to systematically decipher the transformations in the neural basis of behavior.

2.2 Introduction

To generate behaviors, neural activity is transformed through the biomechanics of the body. There have been exciting developments of predictive models that incorporate musculoskeletal dynamics in an array of vertebrate and invertebrate animals [18, 97, 22, 119], including humans [20, 98]. Neuromechanical approaches have been taken to describe the movements of *C. elegans* [105, 91, 52, 30, 60, 61], larval *Drosophila* [77, 104, 134] and leech [123, 110], which all act as muscular hydrostats. In cnidarians, a 2D model of the medusa form of jellyfish *Aurelia aurita* neuronal network and muscles simulates swimming and turning behaviors [92]. In octopus, Yekutieli et al. have simulated the biomechanics and control of reaching movements [130, 131]. However, generally these models are limited in their completeness by the inability to observe the system in its entirety, with simultaneous spatial and temporal patterns of neural activity, muscular activation and whole animal behavior.

Small model systems pose the opportunity to develop relatively complete models of the transformations from neural activity to behavior, taking into account not only the biomechanics of the body but also the biophysics of muscle activation. As an active medium, muscle tissue has its own dynamics that can contribute significantly to this transformation. The small freshwater cnidarian *Hydra* offers a unique and unprecedented inroad into this problem. Along with *Hydra*'s simple body structure, recently developed genetic lines now allow the direct imaging of calcium-based activity in both neurons [25, 5] and muscle cells [112, 129] during behavior. This system thus presents an opportunity to account for the transformation from neural firing to behavior by modeling both body and active muscle dynamics, which determine how neural activation mediates behavioral outputs.

2.2.1 Anatomy and behaviors of Hydra

Hydra's anatomy is that of a fluid-filled body column consisting of two body layers, the ectodermal and endodermal epithelia, separated and supported by an acellular gelatinous layer, the mesoglea (Fig. 1.1) [71, 13, 117]. The epithelial layers consist of a sheet of epitheliomuscular cells, innervated by separate nerve nets [25]. The ectodermal and endodermal epitheliomuscular cells respectively display longitudinal and circumferential processes called

myonemes, producing contractions oriented in corresponding directions [71]. These layers, together with the enclosed fluid, form a hydrostatic skeleton in which the force of muscle contraction is transmitted throughout the body column by internal pressure [59].

Movement in *Hydra* is controlled by a diffuse nerve net. With perhaps the earliest evolved nervous system [29, 63], *Hydra*'s uncoupled ectodermal and endodermal nerve nets [115] lack a centralized "brain" or ganglia, yet their firing activity underlies a rich repertoire of behaviors. These include contraction bursts, active elongation, nodding, bending and two forms of locomotion [121, 103, 95, 96, 112, 39]. However, how neural activity drives behavior is not understood. Early extracellular recordings identified several distinct electrical events in *Hydra*: contraction bursts (CB), rhythmic potentials (RP) and pre-locomotion bursts (PLB) [93, 94, 95, 96]. Recent work has clearly identified three separate functional nerve subnetworks responsible for these electrical events [25]. However, only one of these, the contraction burst (CB) network, is directly correlated with a motor output, namely whole-body contraction [25]. What causes the CB nerve net to fire is still not known, although it is influenced by environmental conditions including osmolarity [75, 80, 81, 8, 7, 124, 66, 126, 129] and temperature [122], as well as microbes [88, 62]. Aside from the CB, the precise association of neural activity with behavior has not yet been mapped out.

2.2.2 Neural control of behavior in Hydra

At what length scale and with what precision does the firing of nerve cells influence movement? These factors depend on how activation is conveyed through muscles, and how the resulting network of muscular contractions interacts with the biomechanics of the body. Due to gap junctional coupling [127, 40], the epitheliomuscular network is able to propagate excitation [95, 55, 56, 3] even when *Hydra*'s nerve cells have been removed [12, 72]. Several studies have suggested that contraction pulses can be conducted by the epithelium in *Hydra* [55, 56, 58, 57, 102]; conduction in nerve-free epithelia has also been demonstrated in other hydrozoans such as Siphonophores, *Sarsia* and *Euphysa* [78, 79]. By imaging calcium signals in the endo- and ectodermal epithelial layers, Szymanski and Yuste [112] reported two distinct forms of muscle layer activation: a rapid global activation that drives whole-body

contraction, and slow waves of local activation, including body column waves, that initiate anywhere in the body column, and bending waves, initiating in a region of the peduncle and that correlate with bending.

Furthermore, as noted, *Hydra* has a fluid hydrostatic skeleton, and its endodermal and ectodermal muscle fibres are oriented in orthogonal directions. One would expect, therefore, that contraction is effected by activating the longitudinal ectodermal layer, while extension is due to activation of the circumferentially oriented endodermal muscles. However, Szymanski and Yuste [112] showed, counterintuitively, that the two muscle layers activate together during contraction bursts–despite the fact that the CB neural network is localized to the ectoderm, and the muscle layers presumably then act against one another during contraction. How can we resolve the generation and transformation of this activation pattern into the observed behavior? All of these observations suggest that the dynamics of the muscle layer itself form an important and nontrivial component of the transformation from nerve firing to behavior.

Here, we construct a model of *Hydra* that includes sufficient biophysical and biomechanical detail to simulate the complete transformation from measured neural activity to muscle activity to behavior. We aimed to address the following specific questions: (i) What are the mechanisms that support the observed dual time scales of muscle activation, and how does *Hydra* use these different dynamics in behavior? (ii) During contraction bursts, although only neurons in the ectodermal nerve net fire [25], both muscle layers are activated [112], and thus work against one another. What explains this dual-layer activation and how can body contraction be achieved with opposing muscle drive? (iii) Can we quantitatively reproduce basic behaviors [39], including contraction, elongation and bending?

To answer these questions, we implemented a multi-layered model (Fig. 2.1) to transform neural activity to movement. Our models are constrained both by observations from calcium imaging and by the use of physiologically plausible mechanisms consistent with the recently developed RNAseq database [109]. To model calcium dynamics in the epitheliomuscular cell network, we postulate the coexistence of a fast cellular electrically mediated pathway and a slow IP_3-driven pathway. We assume that these activation signals are transmitted through the epithelial layers by gap junctions [64, 47, 76, 1]. These two mechanisms permit

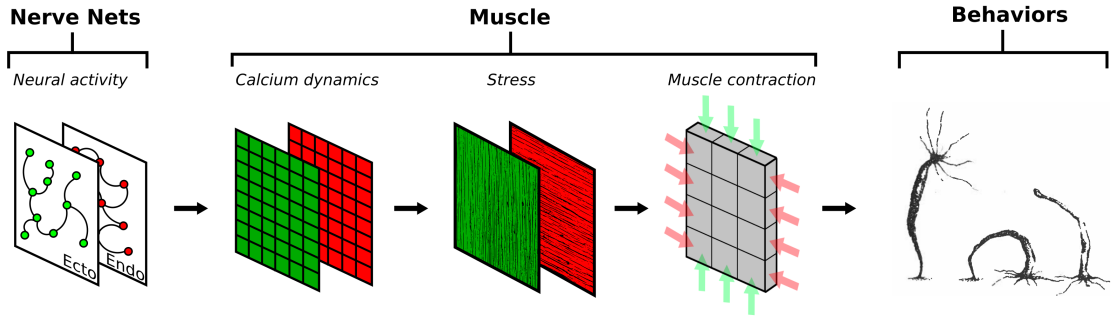

Figure 2.1: Framework of our project. Neural activity patterns trigger calcium dynamics in the muscle layers, which are transformed into contractile forces in the longitudinal (ectoderm; green) and circumferential (endoderm; red) directions, here indicated by the direction of fibres in the muscle layers. This provides the active force to drive a viscoelastic biomechanical model of the Hydra body column, simulating behaviors.

the coexistence of the fast electrically driven contractions as well as slow waves responsible for bending; the model predicts that these dynamics are triggered by distinct signals. We show that an intermediate level of gap junctional coupling between the ecto- and the endodermal epithelium can share contraction activation between the two muscle layers, but isolate slow wave activity to the ectoderm, consistent with observation. We next convert calcium dynamics to force generation. In order to account for *Hydra*'s movement dynamics, it was necessary to hypothesize that the relationship between calcium and force has more persistent dynamics in the endoderm than in the ectoderm, essentially suggesting slower relaxation times for endodermal muscles. Finally, we convert the simulated epithelial calcium dynamics to strain, which provides an active force input into a biomechanical model of the fluid-filled hydrostat. While previous hydrostatic models generally model the body by actuating longitudinal segments [43], here all forces are applied in the fluid-enclosing shell. We use this model to show that the simulated muscle activation, when driven by neural activity inferred from calcium imaging, can account quantitatively for the measured behaviors of contraction, elongation and bending.

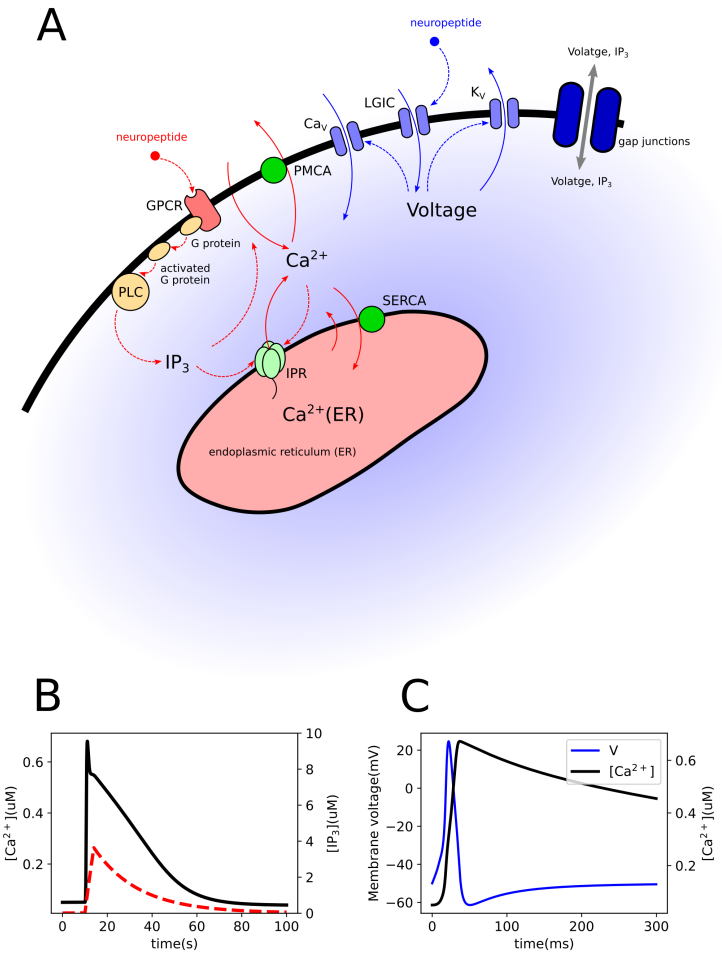

Figure 2.2: Single cell dynamics. (A) Intracellular calcium signaling model including two pathways: (i) in the *slow pathway* (red), neuropeptides bind a G protein-coupled receptor (GPCR) and activate a G protein, which activates phospholipase C (PLC) and hydrolyzes phosphatidylinositol bisphosphate (PIP2) into inositol 1,4,5-trisphosphate (IP_3), which plays a role of the second messenger for calcium signaling. IP_3 can bind to IP_3 receptors (IPR) on the endoplasmic reticulum (ER) membrane and thus cause the release of Ca^{2+} from the ER. Ca^{2+} is extruded to the extracellular space through plasma membrane Ca^{2+} ATPase (PMCA) and is recycled to the ER through sarco/endoplasmic reticulum Ca^{2+}-ATPase (SERCA) [29, 23]. (ii) the *fast pathway* (blue) is initiated by the binding of neuropeptides on ionotropic receptors, which activate ligand-gated ion channels (LGIC) and depolarize the cellular membrane [35]. The elevated membrane potential activates calcium channels (L-type/T-type), triggering a large influx of Ca^{2+} from the extracellular space and invoking a further depolarization. Meanwhile, the high membrane potential inactivates calcium channels and activates potassium channels, resulting in membrane repolarization [45]. (B) Simulated slow dynamics showing change of Ca^{2+} and IP_3 concentrations. (C) Simulated fast dynamics showing change of membrane potential and Ca^{2+} concentration.

2.3 Results

2.3.1 Slow and fast intracellular calcium pathways explains dual timescales dynamics

We first show how the muscle system can exhibit two activation patterns with distinct timescales. The mechanisms of muscle activation are rooted in the biophysics of the single muscle cells and their interactions; thus we begin by modeling the intracellular dynamics of a single *Hydra* muscle cell.

Muscle contraction is controlled by calcium dynamics, where calcium elevation has two possible sources: (i) IP_3-induced Ca^{2+} release from the endoplasmic reticulum/sarcoplasmic reticulum (ER/SR) calcium store, and (ii) Ca^{2+} influx from the extracellular space through L-type/T-type calcium channels [49, 10, 45, 67]. We will refer to these two calcium signaling pathways as the "slow" and "fast" pathways respectively, based on their typical time scales. Both IP_3-related calcium release [54] and electrical excitability [48] are observed in epitheliomuscular cells, and the genes of related component proteins like IP_3 receptor, L-type/T-type calcium channels, PMCA, SERCA, etc. are identified to express in *Hydra*'s genome (see Materials and Methods for details).

Models of smooth muscle frequently treat only one of these pathways. Some models of calcium signaling consider only the slow pathway, ignoring membrane ion channels [21, 74, 108, 41], while others consider only the fast pathway, neglecting the dynamics of the internal calcium stores; examples include models for uterine smooth muscle [99, 120, 16, 132, 118], gastric smooth muscle [17], urinary bladder smooth muscle [83] and pancreatic β-cells [28]. While some models integrate both pathways by incorporating both influx through ion channels and Ca^{2+} release from stores [51, 68, 64, 1], modeling the two pathways separately and simulating calcium dynamics at different time scales is rare [27, 37]. However, since calcium imaging in *Hydra* clearly reveals dynamics with different time scales (short-lasting and fast-propagated calcium transients in CB; long-lasting, slow calcium waves in bending and nodding [112]), we incorporate the necessary components for both slow and fast pathways in our model for *Hydra* epitheliomuscular cells.

Neurons are believed to connect to and stimulate muscles via neuropeptides. While electron microscope (EM) observations have shown evidence of dense core vesicles in *Hydra* tis-

sue [127], these are not associated with postsynaptic structure typical of synapses. The neuropeptides Hydra-RFamides and Hydra-KVamide (expressed in the peduncle region) may play roles in neuromuscular transmission [133, 42, 35]. The neuropeptide Hym-176C can induce ectodermal contraction and is selectively expressed in ectodermal peduncle neurons [133, 109, 90, 62]. Non-selective cation channels HyNaCs were identified in epitheliomuscular cells, which are directly activated by Hydra-RFamides I and II and can depolarize the cellular membrane potential [26, 35]. These findings indicate that neural control may be achieved by the binding of these neuropeptides by receptors in muscle cells. In our model, we propose that two different types of neuropeptides trigger different muscular Ca^{2+} pathways, enabling differential control of distinct spatiotemporal dynamics in the muscle layers, potentially by distinct neurons [29] (Fig. 2.2A).

The simulated slow and fast dynamics are shown in Fig. 2.2B and Fig. 2.2C, respectively, and show that the timescale of the calcium dynamics triggered in slow pathway is much larger than that in fast pathway, consistent with the observations from calcium imaging. Ca^{2+} fluxes and ion current traces are shown in the Supplementary Information Fig. S1.

2.3.2 Various muscle activation patterns can be simulated by dual-functional coupling of intercellular gap junctions

We then extend the single cell model to a multicellular model by incorporating intercellular communication. We construct a muscle sheet (Fig. 2.3A) composed of 60×30 30 μm × 30 μm cells, as measured in an example small *Hydra* (Supplementary Information Fig. S2), with each cell modeled as described above. While cell shape may vary during contraction, for modeling simplicity we do not take this deformation into consideration. Neighboring cells are taken to be electrically coupled, which we assume here to be via gap junctions. Gap junctions have been observed in EM studies [115] both between cells in the same layer, and also penetrating the mesoglea to connect the ectoderm and endoderm [40, 128, 115]. Further, single-cell RNA sequence analysis in *Hydra* shows multiple innexin types in both epithelial cells and neurons [109].

Gap junctions propagate signals by (i) allowing the diffusion of Ca^{2+} as well as second

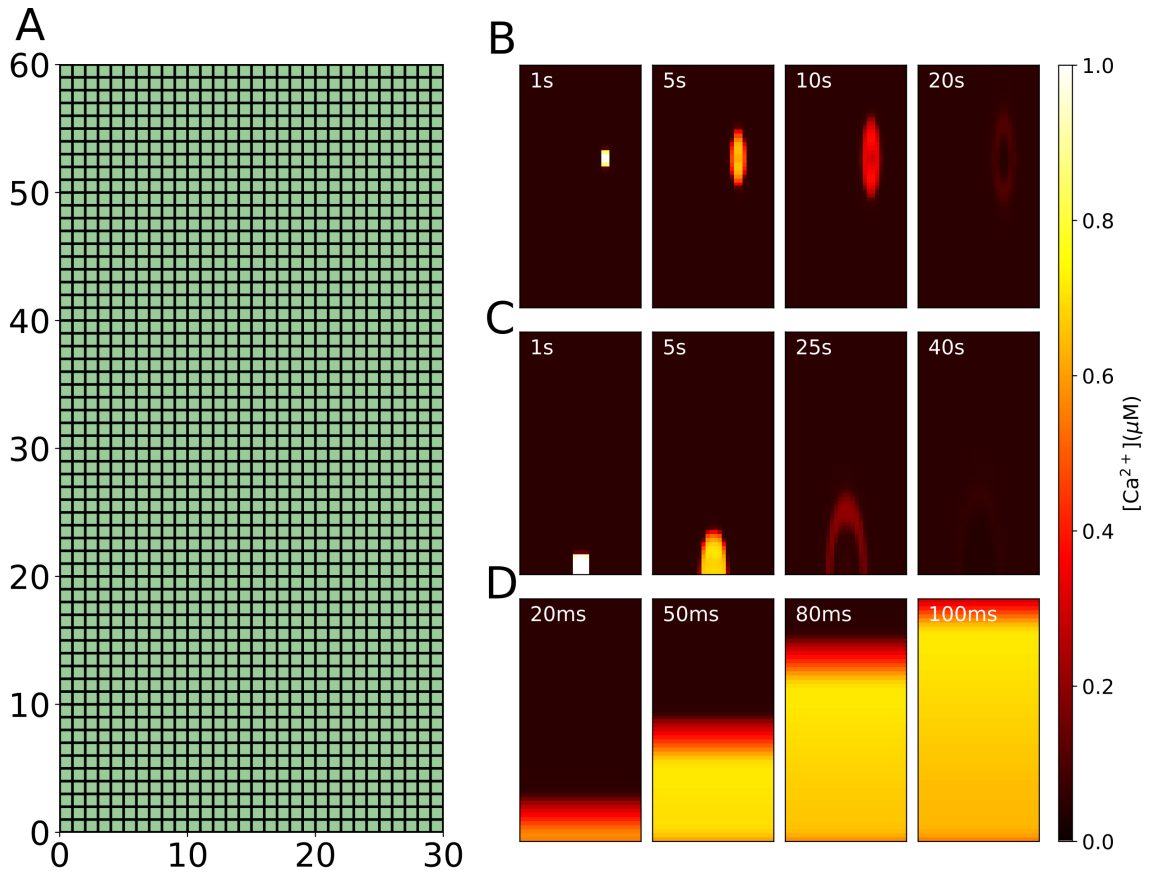

Figure 2.3: Muscle sheet dynamics. (A) We simulate multicellular dynamics by coupling single cell models to their neighbors by gap junctions. (B) Simulation of the body column wave. (C) Simulation of the bending wave. (D) Simulation of the contraction pulse (fast wave).

messengers like IP_3; and (ii) conducting electrical signals [3, 50, 15]. We hypothesize that the two different observed forms of wave propagation in *Hydra* (slow waves and fast calcium synchronization) both occur through different epithelial activation patterns. For slow waves, the propagation of IP_3, but not Ca^{2+} (which is so heavily buffered that its effective intercellular diffusion is negligible [53, 47, 64, 23]), through gap junctions is believed to be the primary trigger of intercellular calcium waves (ICW) [73][111, 24, 46, 47, 31], whose propagation timescale is thus driven by diffusion. The fast wave of calcium synchronization has generally been modelled through electrical conduction by gap junctions [51, 69, 65].

Based on this setting, we simulate several different muscle activation patterns, by assuming the necessary neural stimulation for each pattern and applying it to trigger specific muscle cells directly:

Body-column wave

We hypothesize that the initiation of body-column waves arises from neuromuscular junctions at which neurons release a neuropeptide that locally triggers the slow pathway in muscle cells randomly located in the body column. To simulate these waves, we randomly select a small (2×2) region of cells in the sheet and stimulate their slow pathways. The elevated IP_3 in the stimulated cells diffuses to the neighboring cells and triggers the slow dynamics there, resulting in slow calcium waves propagating through the corresponding local domains. The example result of the simulation are shown in Fig. 2.3B.

Bending wave

A second type of slow wave initiates at the peduncle and slowly propagates in the oral direction through the ectoderm [112]. This asymmetrical calcium activity in the ectoderm is believed to cause bending. To simulate the bending wave, we stimulate the slow pathway in a 4×4 cell-patch located in the peduncle of the ectoderm sheet of our model; propagation is due as above to gap junctional IP_3 diffusion (Fig. 2.3C). To obtain a wave as observed in data, it is necessary to assume that gap junctional coupling is anisotropic, larger longitudinally than circumferentially (see Supplementary Information).

To quantitatively compare the speed of the simulated waves with experimental data, we identified the wavefront of the bending wave in our model as shown in Fig. 2.5G, from which the average propagation speed can be calculated as around 0.9 cells/s. The length of our biomechanical model is in the range of 0.6mm (fully contracted) - 1.7mm (elongated), based on which the length of each cell can be calculated as 9.8 μm (contracted) - 28.8μm (elongated), so the propagation speed is in the range of 9 μm/s - 26.5 μm/s. In [112], the propagation speed of the bending wave was calibrated as 13 $\pm$ 0.7 μm/s, which falls in the range of the simulation. The speed of the fast wavefront is computed as shown in Fig. 2.5H, giving 0.7 cells/ms, or 6 mm/s when the model is in the contracted state. This is of the same order as the propagation speed measured from calcium imaging (4.6-5 mm/s) in [112]. The dependence of these speeds on choices of parameters such as gap junctional coupling coefficients, stimulation strength and rates of receptors are explored in the Supplementary Materials (Fig. S3-5).

Fast wave (contraction pulse)

Hydra's contraction burst (CB) is driven by the firing of a unique subnetwork of the ectodermal nerve net [25] that is distributed across the body but particularly concentrated in a ring in the peduncle. Each contraction pulse causes a global calcium synchronization activating all muscle cells in both ectoderm and endoderm. Measurements in [112] showed that the contraction pulses initiate in the peduncular epithelium and propagate to the rest of the body column. Here we assume these neurons to be the primary source of activation; although as we show later, the distribution of these neurons is not critical to the dynamics. We initiate the fast wave by simulating inputs from a ring of neurons in the peduncle onto the connected muscle cells: we stimulate the fast pathway dynamics in the bottom row (1×30) of the ectodermal sheet. Elevated membrane potentials propagate rapidly to the remainder of the cells via their electrical coupling, giving global calcium synchronization, as shown in Fig. 2.3D.

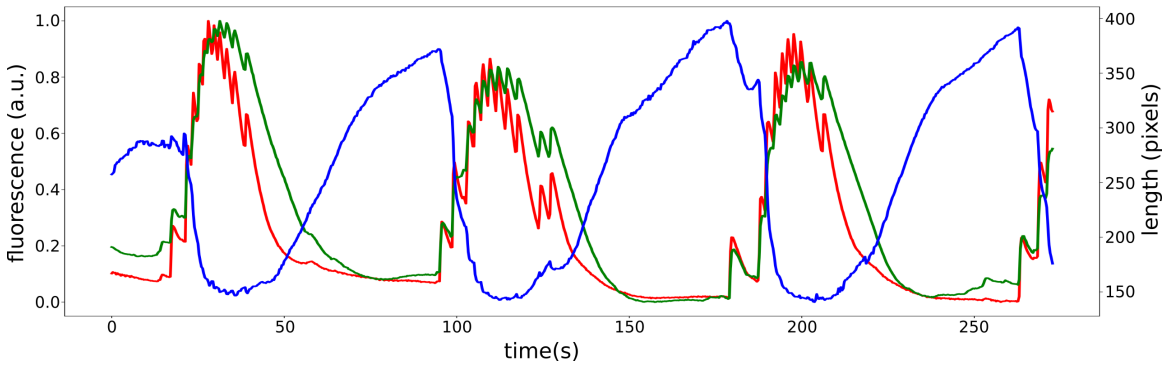

Figure 2.4: Recorded fluorescence from calcium imaging showing simultaneous activation of ectoderm (green) and endoderm (red) during contractions, shown by computing the corresponding time-varying length (blue) of *Hydra*.

2.3.3 Sparse cross-layer gap junctions explain synchronous fast wave and isolated slow wave between ecto- and endoderm

During a contraction burst, neuronal activity is confined to the ectoderm, indicating that CB neurons are localized to the ectoderm [25], while both the ectoderm and the endoderm show an almost synchronous fast wave of epitheliomuscular calcium (Fig. 2.4); in contrast, body column waves and bending waves are only observed in the ectoderm [112].

We propose that the synchronization of fast waves in the two layers is due to electrical coupling through the observed cross-layer gap junctions which penetrate the mesoglea: when cells in the ectoderm are electrically activated, the action potential can propagate through the gap junction and trigger activity in the endodermal epithelium. Cross-layer gap junctions should then also allow a flow of IP_3. However, there is no evidence that slow waves in ectoderm propagate to the endoderm [112]. How can we resolve this? One possibility is that the epitheliomuscular cells of the endoderm do not have the slow activation pathway. Another possibility is that the biophysics of calcium activation is the same, but the physical properties of coupling can lead to this differential filtering.

We test the idea that physical coupling can explain these findings, ie. that the ability of sparsely distributed cross-layer gap junctions to transmit global fast waves but block local slow waves is due simply to their density (Fig. 2.5A). By varying the connectivity ratio (density) of the cross-layer gap junctions in our model, we indeed found when the

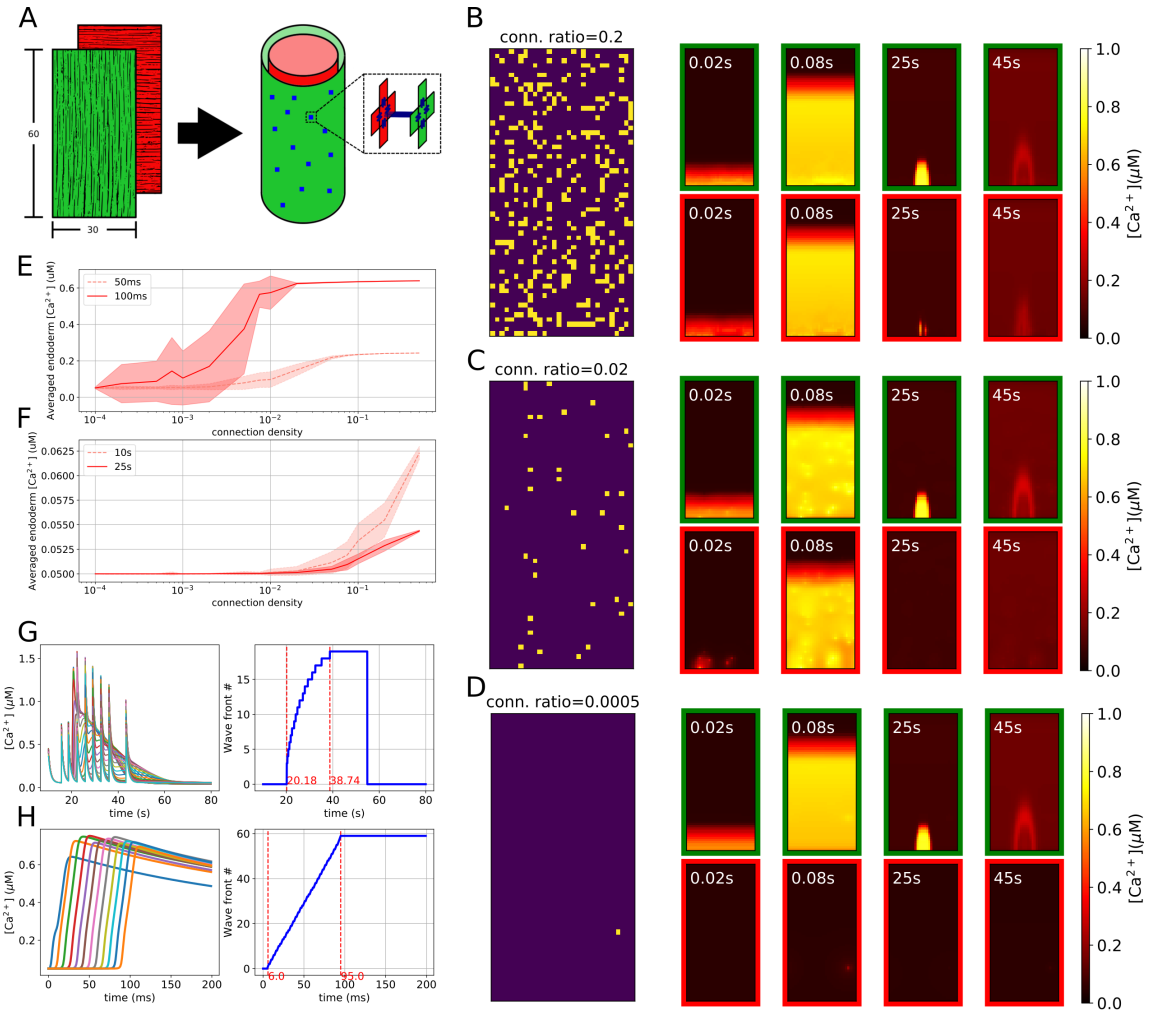

Figure 2.5: Body column settings and dynamics. (A) The layout of the body column model. Green and red represent the ectodermal and endodermal layers respectively, in which the myonemes are aligned in longitudinal and circumferential directions respectively, as represented by the fibre directions. Blue dots represent cross-layer gap junctions. (B-D) Connectivity patterns and calcium patterns of ectoderm (green border) and endoderm (red border) in simulations with different connectivity ratios, where the ratios are separately 20% (B), 2% (C) and 0.05% (D). In connectivity patterns each bright spot represents a gap-junctional connection at that position. (E-F) Diagrams show cross-layer propagation for different connection densities of cross-layer gap junctions. We simulate 20 epochs for each density; we take snapshots at 50ms and 100ms after only triggering the fast pathway (E), and 10s and 25s after only triggering the slow pathway (F), then average the $[Ca^{2+}]_i$ of the whole endoderm, plotting the mean and standard deviation of the 20 epochs for each density at these time points. (G-H) $[Ca^{2+}]_i$ traces and wavefronts along the center longitudinal line (marked in the dashed rectangle), shown for the bending wave (G) and fast wave (H). The right sides show how the wave fronts evolve with time.

connectivity ratio is high, both fast and slow waves can propagate between the two layers; when the ratio is low neither of the two waves propagate; and there is a intermediate range in which only the fast wave crosses the layer (Fig. 2.5B-D).

To further probe the effect of cross-layer gap junction density on the propagation of trans-mesoglea calcium waves, we quantitatively analyzed the relationship between the averaged calcium concentration of the endodermal muscle sheet and the connection density, after stimulating the ectodermal muscle cells' fast (Fig. 2.5E) and slow (Fig. 2.5F) pathway. As shown, for both slow wave and fast waves, a higher connection density of cross-layer gap junctions allows stronger calcium wave propagation from the stimulated ectoderm to the endoderm. When the connection density is very low or very high, the standard deviation is small. In intermediate ranges, there is considerable variability, depending on the specific placement of cross-layer connections. Overall, for an intermediate range of connection densities, only fast waves can cross layers and slow waves are limited to the directly stimulated ectodermal layer.

As noted, it is also possible that the endodermal epithelial cells do not express the slow dynamics of the ectoderm; however for simplicity we will use the same single-cell model for all epithelial cells along with this proposed mechanism for sharing of muscle activation in subsequent simulations.

2.3.4 Transforming calcium dynamics to muscle contraction

Given the modeled calcium dynamics and activation patterns of the whole-body muscle system, we next compute how they generate contraction.

Calcium to force

In smooth muscle, a rise of $[Ca^{2+}]_i$ (intracellular calcium concentration) leads to a rise of calmodulin, leading to increased activation of MLCK (myosin light-chain kinase), phosphorylation of myosin, and thus contraction [23]. The Hai-Murphy model of smooth muscle [36] uses four forms of the crossbridge to simulate the force-production process, where Ca^{2+} plays a role in MLCK activation. The Hai-Murphy model includes the "latch-state" of the

crossbridge, which allows the maintenance of steady-state stress of muscle even if the Ca^{2+} concentration has decreased. Modified Hai-Murphy models have been used to simulate contractions in arteriole [125] and uterine [82, 132] smooth muscle. In our work, we applied a modified version of the Hai-Murphy model, following [132] and [82], to transform $[Ca^{2+}]_i$ into active stress.

Force to contraction

To further convert the stress into *Hydra* movement, as our final step, we need to construct a model that resembles the hydrostatic skeleton of *Hydra* and can simulate the biomechanics of the body, driven by the transformed stress.

We construct our model using the COMSOL Multiphysics 5.3a. We approximate the anatomy of *Hydra* with a simplified biomechanical model that contains two domains: the body shell and the enclosed fluid. The body shell, which represents the combination of the ectoderm and endoderm layers and the mesoglea, is composed of a half spherical shell at the hypostome and a half spherical shell at the peduncle, connected by a uniform body column cylinder shell (Fig. 2.6). In order to manipulate the biomechanical model at high resolution, we divide the body shell into 10 (radial) by 20 (longitudinal) elements. The body shell and enclosed fluid together form a hydrostatic skeleton.

While the COMSOL architecture as described handles the passive biomechanical properties, we apply time-varying active stresses generated by the output of the calcium signaling models; the ectodermal model drives longitudinal external stresses, while the endodermal output drives stress in the circular direction. We obtain the active stress from the calcium signaling model as described above, and average the stress of neighboring 9 cells, coarse-graining the original 30×60 matrix to fit the 10×20 dimensions of the biomechanical model.

Phasic ectoderm and tonic endoderm muscle types simulate the interplay of contraction and elongation

Calcium measurements in the ectoderm and endoderm pose two major questions. How does the observed co-activation of the opposing ectodermal and endodermal contracting

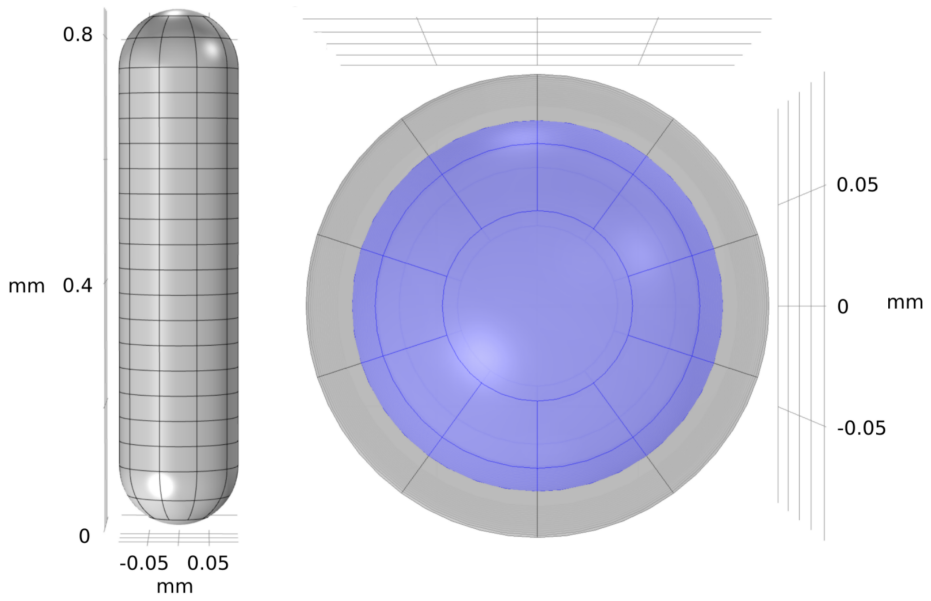

Figure 2.6: Geometry of the biomechanical model from a side view (left) and top view (right). Gray represents the muscle shell domain, while the enclosed fluid is shown as purple.

forces result in a total effect of longitudinal contraction of *Hydra*, instead of opposing each other? Further, why do we see no calcium signal in the endoderm during elongation between contractions (Fig. 2.4)? Indeed, when we directly apply the transformed stress from calcium dynamics on the biomechanical model, the predicted stresses do act in opposition, preventing normal contraction (not shown).

We propose as a potential resolution to this condundrum that ectoderm and endoderm may exhibit different Ca-stress relationships. Different muscle properties can be accounted for within the Hai-Murphy formulation, which can account either for fast-acting phasic behavior as for "fast" myosin isoforms, or tonic contraction via the latch-bridge mechanism, as for "slow" isoforms [38]. By assuming that the ectoderm is phasic and endoderm is tonic, and under the hypothesis that ectoderm can generate a larger maximum stress than that of endoderm (inspired by the observations that the myonemes in ectoderm are longer than those in endoderm [71]), we can successfully simulate the interplay of contraction and elongation. When CB neurons fire, both layers are activated and the ectoderm initially dominates, driving a longitudinal contraction. When CB firing ceases and $[Ca^{2+}]_i$ drops in

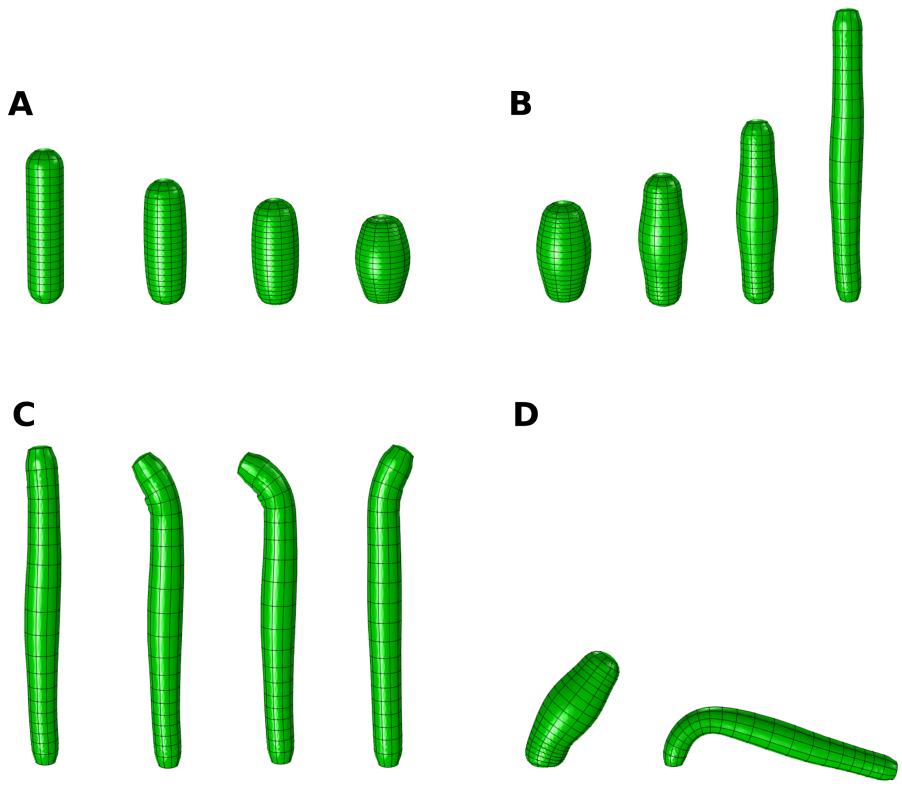

Figure 2.7: Different behaviors simulated by the model. (A) contraction (B) elongation (C) nodding (D) bending.

both layers, the hypothesized slow dynamics of the endoderm allow it to maintain the stress longer without ongoing neuronal stimulation, thus dominating in *Hydra*'s elongation phase.

2.3.5 Integration: simulating the transformation from neural activity to behaviors

With the bottom-up pipeline described above, we are now capable of simulating the observed behaviors of *Hydra*, using different spatiotemporal neural firing patterns to drive muscle activation.

Fig. 2.7 shows our simulation of several typical behaviors of *Hydra*. We simulate contraction and elongation as described above. We simulate bending by stimulating the slow pathways of a small localized group of ectodermal cells at the peduncle, which triggers the bending wave as shown in Fig. 2.3, generating local contraction which causes *Hydra* to bend

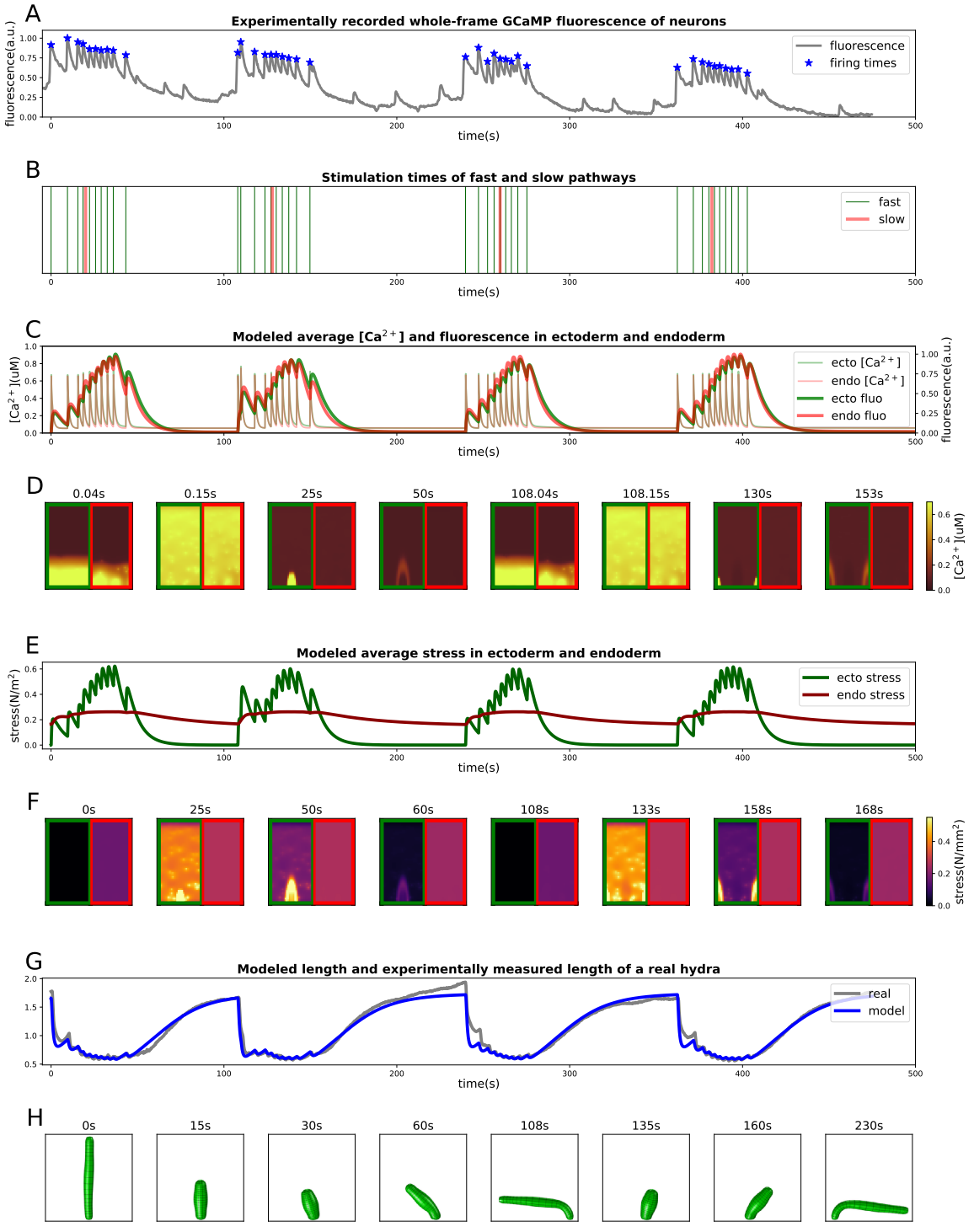

Figure 2.8: Pipeline of the simulation from neural activity to behaviors. (*A*-*B*) NGCaMP fluorescence trace: stars mark estimated times of neural firing (*A*) and consequently, stimulation times for the model (*B*). (*C*-*D*) Averaged $[Ca^{2+}]_i$ and fluorescence intensities in ectoderm and endoderm (*C*) and $[Ca^{2+}]_i$ patterns of some moments (*D*). (*E*-*F*) Averaged active stress in ectoderm and endoderm (*E*) and stress patterns of some moments (*F*). (*G*-*H*) Comparison between length evolution of the model and from a *Hydra* (*G*) recording and some stills of the final simulated behaviors from the model (*H*).

towards the stimulated side. This demonstrates that activation of the slow and fast pathways can coexist without interfering with each other, as the contraction event in the fast pathway does not saturate the calcium dynamics. For nodding, a separate nerve net, called the sub-tentacular network [25], is found to be correlated with nodding behavior. Here we assume that this network simply stimulates the slow pathways of a small set of ectodermal cells in the sub-hypostomal region. This is similar to bending behavior but with an opposite location. Our model is thus able to generate a "bending" of the hypostome towards the stimulated side.

Next, we attempt to reproduce naturalistic behavioral sequences of *Hydra*. Left undisturbed, *Hydra* undergoes repeated cycles of contraction and elongation, combined with bending. From videos of the neuronal GCaMP *Hydra*, we extract behavior, characterized by the animal's skeletonized body length (see Materials and Methods). We use the integrated GCaMP fluorescence trace to infer the firing times of the CB neurons (Fig. 2.8A), and additionally include sparse triggering times for the bending waves (Fig. 2.8B). With this stimulation, we compute the calcium dynamics underlying fast and slow bending waves in the epithelial sheets (Fig. 2.8C, D); the simulated fluorescence traces match the observed curves in Fig. 2.4. After encoding the calcium concentration into stress (Fig. 2.8E, F)), we use it to drive the biomechanical model, successfully exhibiting a series of behaviors that mimic the real *Hydra* (Fig. 2.8H). The simulated length changes show very good quantitative agreement with the dynamics of contraction and elongation of the animal (Fig. 2.8G).

2.4 Discussion

In this work, we have succeeded in implementing a model framework that predicts behaviors from neural firing patterns. Here we review the assumptions, required mechanisms and limitations of our model. We began with a biophysical model for single muscle cell dynamics that is grounded in known molecular mechanisms; we then linked muscle cells into a network via gap junctional coupling, which successfully simulated multiple-timescale calcium activation dynamics observed in GCaMP imaging experiments in *Hydra*. Such multiple-timescale calcium signaling has also been observed in arterial smooth muscles [37]. We then used this model to generate active stress to drive a passive biomechanical model of

the body. This model successfully simulated *Hydra* behaviors including contraction bursts, bending and elongation. These two components together form a model that can exhibit different behaviors with given neuronal stimulation, and can thus serve as a testbed for reverse engineering the neural activity that underlies more complex *Hydra* behaviors.

In order to match observed activity and behavior, we raised and addressed a series of questions. We accounted for the two distinct time scales of calcium patterns in imaging experiments by assuming that there are two different calcium pathways (ionotropic and metabotropic) in each single muscle cell, then captured the different propagation speeds through the dual functions (electrical coupling and chemical diffusion) of gap junctions. By assuming sparsely distributed cross-layer gap junctions between ectoderm and endoderm, we succeeded in producing synchronized fast waves in the two layers along with the isolation of slow waves to the ectoderm. To explain how *Hydra* can longitudinally contract although the two counteraligned muscle layers are simultaneously activated, we postulated that muscles of ectoderm and endoderm have different properties (phasic and tonic). This further explains how *Hydra* can elongate with no apparent endodermal calcium activation (Fig. 2.4). Putting these factors together, we successfully simulated cycles of contraction, elongation and bending.

Despite this success, there are many details and limitations that need to be explored further. For instance, how and which groups of neurons generate activity patterns and transmit these distinct inputs to the muscle is still unclear. We have considered a simplified structure of *Hydra*, and neglected the effects of the surrounding water, whose viscosity and buoyancy may influence natural behavior [89, 87, 101]. Furthermore, our model only assumes feedforward transformations from neural activity to behaviors, although it is likely important to understand how behavior influences neural firing through mechanosensation and other forms of sensory feedback.

2.4.1 Electrical signaling in nerve net and muscle

Our model addresses the question of whether electrical activity during contraction bursts is transmitted through the nerve net or the muscle layer. We propose that hypostomal

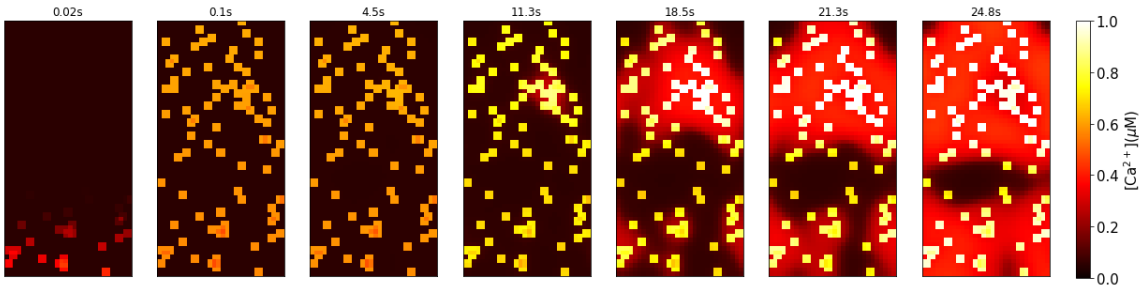

Figure 2.9: Modeled calcium activation pattern under sequential stimulation of the fast pathways of randomly chosen 2×2 groups of muscle cells in the body column with no gap junctional electrical conductance.

neurons play a role of integrating information from the environment: following a decision to fire, the signal is propagated through the sparsely distributed CB nerve subnet to the peduncle ring of motor neurons, which acts as the primary drive of contraction. This architecture is supported by the observed propagation of fast calcium activation from the peduncle towards oral side [112], the expression of Hym-176C in the peduncle [133] and the previous observation of electrical conduction in the nerve-free *Hydra* epithelia [12].

However, we believe that during contraction, synchronous drive from the nerve net is supplemented by the electrical coupling property of muscle cells themselves. The CB neurons are sparsely distributed in the body column; it is unlikely that the CB neurons directly innervate all muscle cells, although it is possible that each neuron drives a small group of them. We simulated the dynamics that result from setting the electrical conductance between muscles to zero and stimulating random small groups of muscle cells with an imaginary electrical wave purely in the nerve net; this leads to slowly growing nodes of excitation via the slow chemical diffusion of IP_3 (Fig. 2.9). Thus we believe that electrical coupling of muscle cells is needed to explain the rapid synchronization of calcium activity in the epithelium [6]. The distributed network of CB neurons are likely necessary to integrate and generate the contraction activity, and may contribute to the robustness of contraction.

We also demonstrated that sparse electrical coupling between the muscle layers is a mechanism that can account for the coactivation of longitudinal and circumferential contraction during contraction bursts. While it is counterintuitive that these muscles would activate together, this may have a functional role; as suggested in [112], the resulting stresses

on the body may serve to regularly squeeze absorbed water out of the body walls.

Hydra has two additional known synchronously firing networks, the "rhythmic potentials" RP1 and RP2. We have found no correlation of RP firing with instantaneous length changes; thus it is unlikely that the RP networks directly control muscle contraction. However, it has been suggested the "radial contraction" behavior is particularly related to RP2 [25]. The ectodermal RP1 nerve net may inhibit CB neurons therefore suppressing contraction bursts, based on the fact that its frequency is inversely proportional to contraction bursts [93, 86, 25]. Previous studies proposed a mutual post-inhibitory rebound relationship between CB and RP neurons [113, 114], but the mechanism of how CB and RP interact with each other has not yet been identified.

2.4.2 Feedback from behavior and the environment

Our model simulates the transformation from neural stimulation to behaviors as a purely feedforward control pipeline, but there are several ways in which feedback may play a role. The rules that govern the generation of the neural activity are still an open question.

Many previous studies have postulated that contraction bursts play a role of osmoregulation [75, 81, 124, 8, 9, 129]. EM studies show that intercellular vacuoles in *Hydra* tissue may contribute to hyposmotic fluid formation, so that contraction bursts may regulate the osmotic pressure by periodically squeezing the fluid from vacuoles to the enteron [7]. Based on these observations, it is reasonable to assume that periodic neural activity is mediated by osmotic pressure through mechanosensation [6]. Besides osmolarity, recent experiments also show that temperature can influence the CB firing rate [122].

A further source of potential feedback that we have neglected is that between the movement of the animal and the dynamics of diffusion. In the model, we assumed that the speed of IP_3 diffusion is faster in the longitudinal direction than in the circular direction, in order to account for the different propagation speeds of bending waves in longitudinal and circular directions, in units of cells per second. While it is possible that the density of longitudinally oriented gap junctions may be larger than that of circularly oriented ones, it is also possible that the propagation speeds in the two directions are the same, but since bending

waves are usually initiated when *Hydra* is contracted and cells are squeezed longitudinally, the wave may travel through more cells longitudinally than circumferentially. In order to incorporate this, one would need to model the relationship between the coefficient of IP_3 diffusion and the local cell shape. Implementing such feedback between the biophysics of the muscle layer and the geometry of the biomechanical model would require considerable engineering effort. In general, however, accounting for any of these effects is possible by extending the framework of our model.

2.4.3 Body plan simplicity

Our biomechanical model simplifies *Hydra* to a hollow cylinder with two spherical ends. However, *Hydra*'s body column deviates from cylindrical, slimming toward the peduncle. Furthermore, cells across the body are heterogenous in size and shape. Recent work indicates that there is variation in the Young's modulus of the body column, and suggests that this can affect somersaulting behavior [89]. Future work could explore more precisely how the body wall mechanics transform neural signals and muscle forces into behavior. Further, we do not attempt to model the tentacles, whose sensory input likely contributes significantly to *Hydra*'s movement, and whose adhesion to surfaces frequently affects body movement. Modeling such details will be necessary to obtain detailed quantitative agreement between the model and additional aspects of behavior, including the effects of water, that present in fully natural 3D behaviors. Our goal here was to capture the most significant factors of the biomechanics that underlie the behaviors of *Hydra* that have to date been recorded simultaneously with calcium imaging, excluding higher order complexities. We hope our model will serve as a starting point for further work to capture the full richness of *Hydra*'s natural behavior.

2.5 Materials and Methods

2.5.1 Single cell model

The differential equations that describe the calcium dynamics in a single cell are shown in Eq. 2.1,

$$\frac{\mathrm{d}C}{\mathrm{d}t} = J_{\mathrm{IPR}} + J_{\mathrm{leak}} - J_{\mathrm{SERCA}} - J_{\mathrm{PMCA}} + J_{\mathrm{in}} - \alpha I_{\mathrm{Ca}} \tag{2.1a}$$

$$\frac{\mathrm{d}S}{\mathrm{d}t} = \beta(-J_{\mathrm{IPR}} - J_{\mathrm{leak}} + J_{\mathrm{SERCA}}) \tag{2.1b}$$

$$\frac{\mathrm{d}P}{\mathrm{d}t} = v_{\mathrm{PLC}\beta} - k_{\mathrm{deg}}P + P_{\mathrm{coupling}} \tag{2.1c}$$

$$\frac{\mathrm{d}V}{\mathrm{d}t} = -\frac{1}{C_m}\left(I_{\mathrm{Ca}} + I_{\mathrm{K}} + I_{\mathrm{L}} + I_{\mathrm{stim}}\right) + V_{\mathrm{coupling}} \tag{2.1d}$$

where C is the cytosolic Ca^{2+} concentration; S is the ER Ca^{2+} concentration; P is the cytosolic IP_3 concentration; and V is the membrane potential. Detailed expressions of terms and equilibrium conditions are included in the Supplementary Information; the corresponding parameters can be found in Table S1.

Triggering of the slow pathway is simulated by elevating $v_{\mathrm{PLC}\beta}$ from 0.002 to 1 μM/s for 4 s; triggering of the fast pathway is simulated by a 10 ms current I_{stim}. Though the dynamics of both fast and slow pathways are formulated with the same set of equations, one does not interfere with the other when activated – when only the fast pathway is on, the elevated $[Ca^{2+}]_i$ cannot activate IPR alone with a low $[IP_3]_i$; when only the slow pathway is on, since the dynamics is in the inner cytosol [47, 23], the membrane potential remains subthreshold and the voltage-gated channels remain inactivated [64]. Both slow and fast pathways are active during the initiation of bending during contraction bursts, but as shown in the simulation results, they simply overlap one other, giving a natural activation pattern and motion.

2.5.2 Multicellular model

Each cell is treated as a compartment. To model the role of gap junctions in propagating electrical signals and diffusing IP_3, neighbouring cells within a layer and the cells at the same location in the endoderm and ectoderm are connected by coupling terms $V_{\mathrm{coupling}} = \sum_{k\in\mathrm{neighbors}} g_c(V_k - V)$ and $P_{\mathrm{coupling}} = \sum_{k\in\mathrm{neighbors}} g_{\mathrm{IP_3}}(P_k - P)$ (incorporated in Eq. 2.1). While all neighboring cells within a layer are coupled, cells with the same indices in the two layers are connected probabilistically, with a defined connection density as the ratio.

The sensitivity analysis showing how parameters affect the wave propagation is included in the Supplementary Information text and figures: Fig. S3 shows the effects of stimulation strength, Fig. S4 shows the effects of coupling coefficients, Fig. S5 shows the effects of some intracellular parameters.

2.5.3 Force generation

We apply the Hai-Murphy model [36] to transform calcium concentration to force, described by Eq. 2.2,

$$\frac{\mathrm{d}M}{\mathrm{d}t} = -k_1 M + k_2 Mp + k_7 AM, \tag{2.2a}$$

$$\frac{\mathrm{d}Mp}{\mathrm{d}t} = k_1 M - (k_2 + k_3) Mp + k_4 AMp, \tag{2.2b}$$

$$\frac{\mathrm{d}AMp}{\mathrm{d}t} = k_3 Mp - (k_4 + k_5) AMp + k_6 AM, \tag{2.2c}$$

$$\frac{\mathrm{d}AM}{\mathrm{d}t} = k_5 AMp - (k_6 + k_7) AM. \tag{2.2d}$$

where M, Mp, AMp and AM represent the ratios of four possible states of the myoneme, respectively unattached and unphosphorylated (M), unattached and phosphorylated (Mp), attached and phosphorylated (AMp), unattached and phosphorylated (AM). The final active stress is $F_a = K_F(AMp + AM)$.

The proposed difference between ectoderm and endoderm is reflected by different parameters of the Hai-Murphy model, primarily represented by the difference of k_7, which is the detachment rate of the "latch-bridge" state of myoneme: its value for endoderm (tonic muscle) is set to be much larger than that for ectoderm (phasic muscle), allowing the endoderm to maintain the contraction for a longer time than the ectoderm; also, k_1 of the endoderm is more sensitive to calcium concentration than that of the ectoderm, so endoderm activates more readily.

The values of these parameters can be found in Supplementary Information Table S2. The match between the length change of the model and Hydra data in Fig. 2.8F is primarily achieved by tuning these Hai-Murphy model parameters.

2.5.4 Biomechanics

We build our biomechanical model on COMSOL Multiphysics 5.3a, based on the finite-element method. To define the passive properties of *Hydra* body, we define the body shell of our model as an incompressible hyperelastic material which follows a Neo-Hookean model [100]. Hyperelastic materials exhibit a nonlinear stress-strain behavior and can respond elastically under very large strains [11]. Muscle tissues are often well-described [32, 106, 14] and modeled [4, 33, 116] using hyperelastic properties. The passive biomechanical properties were mostly modeled based on Hill's three element model [44]. Since biological soft tissues have hyperplasticity or viscoelasticity [84], we use hyperelastic material parameters to model the *Hydra* muscle shell and further incorporated viscoelasticity by including a Kelvin-Voigt model into the body shell material. For the enclosed fluid, we use the COMSOL simulation environment's preset material "Water", with a moving mesh. The elastic modulus and viscosity are set based on previous experimental measurements [13]. The interaction between the body shell and enclosed fluid is simulated by the Fluid-Structure Interaction (FSI) module of COMSOL.

To integrate the biophysical Ca model with the COMSOL-based biomechanical model, we use the LiveLink$^{\text{TM}}$ *for* MATLAB extension of COMSOL: we save the Python simulation results of stress into .csv files, then use MATLAB to load them and call API of the LiveLink to apply the resulting stress to the biomechanical model built on COMSOL; then finally run the biomechanical simulation on COMSOL.

The parameters used in the COMSOL model are shown in Supplementary Information Table S3. Our biomechanical settings (represented by Lamé parameters) assume a 10 kPa elastic modulus and 20 μm shell thickness, which are consistent with Kücken et al.[66]'s 11 kPa and 20 μm, and do not conflict with the parameters (4.94 kPa ectodermal, 4.39 kPa endodermal, in absence of mesoglea) measured by Carter et al. [13]. For simplicity, we treat the muscle shell as incompressible, without taking its inner vacuoles and water excretion [7] into specific consideration, thus we set the Poisson's ratio as 0.499 (not 0.5 for numerical simulation restriction), rather than 0.25 as in Kücken et al. [66].

Configurations for the COMSOL solver are shown in Table S4. Sensitivity analysis

showing how some parameters affect the length change of the biomechanical model during the simulation is shown in Fig. S7.

2.5.5 Model constraints: gene-expression database

To validate choices of biophysical mechanisms including channels, receptors and pumps, we queried gene expression databases for proposed components. We identified candidate genes by FASTA using the NCBI protein database and then used BLAST [2] to search for these genes in the databases *Hydra* 2.0 genome, Augustus Gene Models and Juliano aepLRv2. The Broad *Hydra* Single-Cell Portal [109] further allowed us to identify body regions with corresponding gene expression. We limited ourselves to mechanisms that were consistent with these data bases.

2.5.6 Fluorescence encoding

We adopt a modified SBM model from [34] to simulate fluorescence traces from $[Ca^{2+}]_i$, in which GCaMP6s has five different binding states depending on how many Ca^{2+} ions are binding, and the fluorescence can be produced by all binding states to different extents. Since fluorescence encoding is independent from our neuromechanical modeling and we lack single-cellular-level accurate data with which to fit the model, we roughly tuned the parameters to produce qualitatively reasonable traces for comparison.

2.5.7 Hydra cultures and imaging

All Hydra lines were maintained at 18℃ and fed newly hatched *Artemia nauplii* two to three times per week. *Hydra* expressing the calcium indicator GCaMP6 in the ectoderm of the animal were used for imaging experiments. We used a modified imaging preparation from [25]. All imaging took place under a ZEISS Axio Zoom.V16 equipped with Zeiss AxioCam 506 monochrome camera for fluorescent imaging, PlanNeoFluar Z 2.3X objective lens and a GFP fluorescent filter set. The imaging arena consisted of a microscope slide, 50 to 100 μm spacer and a cover slip. The use of the spacer allowed us to keep the animals in focus by preventing motion in the z direction while still allowing free motion in the x and y

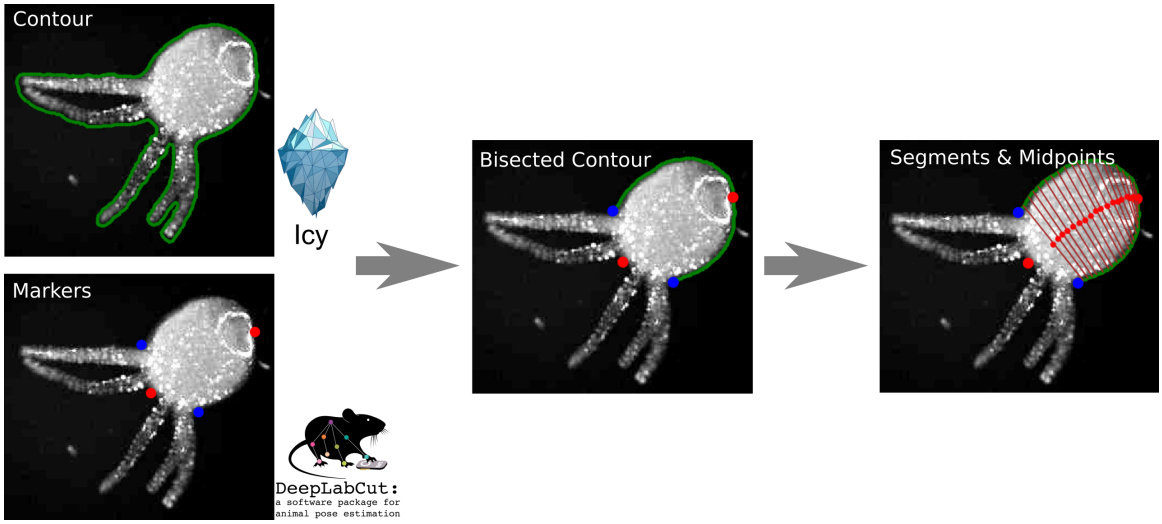

Figure 2.10: Pipeline of the video analysis.

directions. Animals were recorded in the arena for 30-60 minutes at a sampling rate of 4 to 10 frames per second.

2.5.8 Video analysis

We used image analysis to estimate integrated fluorescence in the neuronal and muscle GCAMP lines (in contrast to single neuron tracking [70]) as well as to accurately characterize *Hydra*'s body configuration. Acquired movies were processed using a combination of ImageJ [107], the Icy Imaging software suite [19], DeepLabCut [85] and custom scripts, with a pipeline shown in Fig. 2.10. ImageJ was used to adjust the contrast from background noise which is essential to accurately extract contours of the *Hydra*. Noise was reduced using median filtering (despeckle plugin). Icy Imaging was then used to extract the contours of individual frames using the Active Contours plugin. We can then integrate fluorescence signals within the contour. We then used DeepLabCut to track 4 reasonably well-identified body locations: the center of the hypostome, the center of the peduncle, and the points of intersection of the left- and rightmost tentacles with the body column (the "armpits"). The tracked "armpits" from DeepLabCut were used to exclude the tentacles from the Icy contour. We then used the peduncle to bisect the contour, and proportionally segment the

two contour halves. Connecting the midpoints of the segmentation points allowed us to extract the curved midline of the *Hydra* body in each frame.

2.5.9 Model reduction

While all of the parameters included in our model are based on previous work and lie within physiological ranges, such a biophysical level model inevitably includes many parameters. Therefore, we explored reducing the dimensionality of our model by fitting Green's functions, which can represent spatiotemporal patterns as an impulse response to neural input. This had some success in capturing qualitative aspects of the responses but as a linear method, cannot capture nonlinear interactions between activations. Details of this analysis are shown in the Supplementary Information text, Fig. S8, Fig. S9 and Table S5.

2.6 Acknowledgement

This project is supported by NSF CRCNS 1822550, NSF 2203119 and a Simons Collaboration for the Global Brain grant to A.L.F.. R.Y. was supported by the Burroughs Wellcome Fund 2018 Collaborative Research Travel Grant and the Vannevar Bush Faculty Award (ONR N000142012828). MBL research was supported in part by competitive fellowship funds from the H. Keffer Hartline, Edward F. MacNichol, Jr. Fellowship Fund, The E. E. Just Endowed Research Fellowship Fund, Lucy B. Lemann Fellowship Fund, Frank R. Lillie Fellowship Fund Fellowship Fund, the Fries Trust Research Award, Hartline MacNichol Research Award, L. & A. Colvin Summer Research Fellowship, and John M. Arnold Fellowship Research Award of the Marine Biological Laboratory in Woods Hole, MA. M.M.B., A.L.F. and J.S. were supported by the University of Washington's Royalty Research Fund. M.R. and T.L.D. were supported in part by the University of Washington Center for Translational Muscle Research (1 P30 AR074990). We thank Rob Steele, Celina Juliano and Jacob Robinson for valuable discussions. We thank the MBL Whitman Center for supporting the Hydra lab in the summers of 2017, 2018 and 2019.

Bibliography

[1] Md Ashfaq Ahmed, Sharmila Venugopal, and Ranu Jung. Engaging biological oscillators through second messenger pathways permits emergence of a robust gastric slow-wave during peristalsis. *bioRxiv*, 2021.

[2] Stephen F Altschul, Warren Gish, Webb Miller, Eugene W Myers, and David J Lipman. Basic local alignment search tool. *Journal of molecular biology*, 215(3):403–410, 1990.

[3] Peter AV Anderson. Epithelial conduction: its properties and functions. *Progress in neurobiology*, 15(3):161–203, 1980.

[4] Mohd Ansari, Sang Kyo Lee, Chong Du Cho, et al. Hyperelastic muscle simulation. In *Key Engineering Materials*, volume 345, pages 1241–1244. Trans Tech Publ, 2007.

[5] Krishna N Badhiwala, Daniel L Gonzales, Daniel G Vercosa, Benjamin W Avants, and Jacob T Robinson. Microfluidics for electrophysiology, imaging, and behavioral analysis of hydra. *Lab on a Chip*, 18(17):2523–2539, 2018.

[6] Krishna N Badhiwala, Abby S Primack, Celina Juliano, and Jacob T Robinson. Multiple neuronal networks coordinate hydra mechanosensory behavior. *bioRxiv*, pages 2020–10, 2021.

[7] Dale J Benos, R Gary Kirk, William P Barba, and Marcia M Goldner. Hyposmotic fluid formation in hydra. *Tissue and Cell*, 9(1):11–22, 1977.

[8] Dale J Benos and Robert D Prusch. Osmoregulation in fresh-waterhydra. *Comparative Biochemistry and Physiology Part A: Physiology*, 43(1):165–171, 1972.

[9] Dale J Benos and Robert D Prusch. Osmoregulation in hydra: Column contraction as a function of external osmolality. *Comparative Biochemistry and Physiology Part A: Physiology*, 44(4):1397–1400, 1973.

[10] Michael J Berridge. Smooth muscle cell calcium activation mechanisms. *The Journal of physiology*, 586(21):5047–5061, 2008.

[11] Allan F Bower. *Applied mechanics of solids*. CRC press, 2009.

[12] RD Campbell, RK Josephson, WE Schwab, and NB Rushforth. Excitability of nerve-free hydra. *Nature*, 262(5567):388–390, 1976.

[13] Jason A Carter, Callen Hyland, Robert E Steele, and Eva-Maria S Collins. Dynamics of mouth opening in hydra. *Biophysical journal*, 110(5):1191–1201, 2016.

[14] Grégory Chagnon, Marie Rebouah, and Denis Favier. Hyperelastic energy densities for soft biological tissues: a review. *Journal of Elasticity*, 120(2):129–160, 2015.

[15] George J Christ, David C Spray, Marwan El-Sabban, Lisa K Moore, and Peter R Brink. Gap junctions in vascular tissues: evaluating the role of intercellular communication in the modulation of vasomotor tone. *Circulation Research*, 79(4):631–646, 1996.

[16] Amy L Cochran and Yingxin Gao. A model and simulation of uterine contractions. *Mathematics and Mechanics of Solids*, 20(5):540–564, 2015.

[17] Alberto Corrias and Martin L Buist. A quantitative model of gastric smooth muscle cellular activation. *Annals of biomedical engineering*, 35(9):1595–1607, 2007.

[18] TL Daniel. Invertebrate swimming: integrating internal and external mechanics. *Symposia of the Society for Experimental Biology*, 49:61—89, 1995.

[19] Fabrice De Chaumont, Stéphane Dallongeville, Nicolas Chenouard, Nicolas Hervé, Sorin Pop, Thomas Provoost, Vannary Meas-Yedid, Praveen Pankajakshan, Timothée Lecomte, Yoann Le Montagner, et al. Icy: an open bioimage informatics platform for extended reproducible research. *Nature methods*, 9(7):690–696, 2012.

[20] Friedl De Groote and Antoine Falisse. Perspective on musculoskeletal modelling and predictive simulations of human movement to assess the neuromechanics of gait. *Proceedings of the Royal Society B*, 288(1946):20202432, 2021.

[21] Gary W De Young and Joel Keizer. A single-pool inositol 1, 4, 5-trisphosphate-receptor-based model for agonist-stimulated oscillations in ca2+ concentration. *Proceedings of the National Academy of Sciences*, 89(20):9895–9899, 1992.

[22] S. L. Delp and J. P. Loan. A computational framework for simulating and analyzing human and animal movement. *Computing in Science Engineering*, 2(5):46–55, 2000.

[23] Geneviève Dupont, Martin Falcke, Vivien Kirk, and James Sneyd. *Models of calcium signalling*, volume 43. Springer, 2016.

[24] Geneviève Dupont, THIERRY TORDJMANN, Caroline Clair, Stéphane Swillens, MICHEL CLARET, and Laurent Combettes. Mechanism of receptor-oriented intercellular calcium wave propagation in hepatocytes. *The FASEB Journal*, 14(2):279–289, 2000.

[25] Christophe Dupre and Rafael Yuste. Non-overlapping neural networks in hydra vulgaris. *Current Biology*, 27(8):1085–1097, 2017.

[26] Stefan Dürrnagel, Björn H Falkenburger, and Stefan Gründer. High ca2+ permeability of a peptide-gated deg/enac from hydra. *Journal of General Physiology*, 140(4):391–402, 2012.

[27] Patrick A Fletcher and Yue-Xian Li. An integrated model of electrical spiking, bursting, and calcium oscillations in gnrh neurons. *Biophysical journal*, 96(11):4514–4524, 2009.

[28] Leonid E Fridlyand, DA Jacobson, A Kuznetsov, and Louis H Philipson. A model of action potentials and fast ca2+ dynamics in pancreatic β-cells. *Biophysical journal*, 96(8):3126–3139, 2009.

[29] Toshitaka Fujisawa and Eisuke Hayakawa. Peptide signaling in hydra. *International Journal of Developmental Biology*, 56(6-7-8):543–550, 2012.

[30] Padraig Gleeson, David Lung, Radu Grosu, Ramin Hasani, and Stephen D Larson. c302: a multiscale framework for modelling the nervous system of caenorhab-

ditis elegans. *Philosophical Transactions of the Royal Society B: Biological Sciences*, 373(1758):20170379, 2018.

[31] Mati Goldberg, Maurizio De Pittà, Vladislav Volman, Hugues Berry, and Eshel Ben-Jacob. Nonlinear gap junctions enable long-distance propagation of pulsating calcium waves in astrocyte networks. *PLoS computational biology*, 6(8), 2010.

[32] Laure-Lise Gras, David Mitton, Philippe Viot, and Sébastien Laporte. Hyper-elastic properties of the human sternocleidomastoideus muscle in tension. *Journal of the mechanical behavior of biomedical materials*, 15:131–140, 2012.

[33] LL Gras, D Mitton, P Viot, S Laporte, et al. Modelling of human muscle behaviour with a hyper-elastic constitutive law. *Computer Methods in Biomechanics and Biomedical Engineering*, 13(S1):63–64, 2010.

[34] David S Greenberg, Damian J Wallace, Kay-Michael Voit, Silvia Wuertenberger, Uwe Czubayko, Arne Monsees, Takashi Handa, Joshua T Vogelstein, Reinhard Seifert, Yvonne Groemping, et al. Accurate action potential inference from a calcium sensor protein through biophysical modeling. *BioRxiv*, page 479055, 2018.

[35] Stefan Gründer and Marc Assmann. Peptide-gated ion channels and the simple nervous system of hydra. *Journal of Experimental Biology*, 218(4):551–561, 2015.

[36] Chi-Ming Hai and Richard A Murphy. Cross-bridge phosphorylation and regulation of latch state in smooth muscle. *American Journal of Physiology-Cell Physiology*, 254(1):C99–C106, 1988.

[37] Nadia Halidi, Francois-Xavier Boittin, Jean-Louis Bény, and Jean-Jacques Meister. Propagation of fast and slow intercellular ca2+ waves in primary cultured arterial smooth muscle cells. *Cell calcium*, 50(5):459–467, 2011.

[38] Shaojie Han, John E Speich, Thomas J Eddinger, Krystina M Berg, Amy S Miner, Chris Call, and Paul H Ratz. Evidence for absence of latch-bridge formation in muscular saphenous arteries. *American Journal of Physiology-Heart and Circulatory Physiology*, 291(1):H138–H146, 2006.

[39] Shuting Han, Ekaterina Taralova, Christophe Dupre, and Rafael Yuste. Comprehensive machine learning analysis of hydra behavior reveals a stable basal behavioral repertoire. *Elife*, 7:e32605, 2018.

[40] Arthur R Hand and Stephen Gobel. The structural organization of the septate and gap junctions of hydra. *The Journal of cell biology*, 52(2):397–408, 1972.

[41] Gregory Handy, Marsa Taheri, John A White, and Alla Borisyuk. Mathematical investigation of ip 3-dependent calcium dynamics in astrocytes. *Journal of computational neuroscience*, 42(3):257–273, 2017.

[42] Georg Nørgaard Hansen, Michael Williamson, and Cornelis JP Grimmelikhuijzen. Two-color double-labeling in situ hybridization of whole-mount hydra using rna probes for five different hydra neuropeptide preprohormones: evidence for colocalization. *Cell and tissue research*, 301(2):245–253, 2000.

[43] Evan G Hemingway and Oliver M O'Reilly. Continuous models for peristaltic locomotion with application to worms and soft robots. *Biomechanics and Modeling in Mechanobiology*, 20(1):5–30, 2021.

[44] Archibald Vivian Hill. The heat of shortening and the dynamic constants of muscle. *Proceedings of the Royal Society of London. Series B-Biological Sciences*, 126(843):136–195, 1938.

[45] David C Hill-Eubanks, Matthias E Werner, Thomas J Heppner, and Mark T Nelson. Calcium signaling in smooth muscle. *Cold Spring Harbor perspectives in biology*, 3(9):a004549, 2011.

[46] Thomas Höfer, Antonio Politi, and Reinhart Heinrich. Intercellular ca2+ wave propagation through gap-junctional ca2+ diffusion: a theoretical study. *Biophysical journal*, 80(1):75–87, 2001.

[47] Thomas Höfer, Laurent Venance, and Christian Giaume. Control and plasticity of intercellular calcium waves in astrocytes: a modeling approach. *Journal of Neuroscience*, 22(12):4850–4859, 2002.

[48] Molly A Holman and Peter AV Anderson. Voltage-activated ionic currents in myoepithelial cells isolated from the sea anemone calliactis tricolor. *Journal of experimental biology*, 161(1):333–346, 1991.

[49] Arie Horowitz, Constance B Menice, Regent Laporte, and Kathleen G Morgan. Mechanisms of smooth muscle contraction. *Physiological reviews*, 76(4):967–1003, 1996.

[50] JD Huizinga, LWC Liu, MG Blennerhassett, Lars Thuneberg, and A Molleman. Intercellular communication in smooth muscle. *Experientia*, 48(10):932–941, 1992.

[51] Mohammad S Imtiaz, Christopher P Katnik, David W Smith, and Dirk F van Helden. Role of voltage-dependent modulation of store ca2+ release in synchronization of ca2+ oscillations. *Biophysical journal*, 90(1):1–23, 2006.

[52] Eduardo J Izquierdo and Randall D Beer. From head to tail: a neuromechanical model of forward locomotion in caenorhabditis elegans. *Philosophical Transactions of the Royal Society B: Biological Sciences*, 373(1758):20170374, 2018.

[53] M Saleet Jafri and Joel Keizer. Diffusion of inositol 1, 4, 5-trisphosphate but not ca2+ is necessary for a class of inositol 1, 4, 5-trisphosphate-induced ca2+ waves. *Proceedings of the National Academy of Sciences*, 91(20):9485–9489, 1994.

[54] Christopher J Johnson, Florian Razy-Krajka, and Alberto Stolfi. Expression of smooth muscle-like effectors and core cardiomyocyte regulators in the contractile papillae of ciona. *EvoDevo*, 11(1):1–18, 2020.

[55] Robert K Josephson. Conduction and contraction in the column of hydra. *Journal of Experimental Biology*, 47(1):179–190, 1967.

[56] Robert K Josephson and Martin Macklin. Electrical properties of the body wall of hydra. *The Journal of General Physiology*, 53(5):638–665, 1969.

[57] G Kass-Simon. Longitudinal conduction of contraction burst pulses from hypostomal excitation loci inhydra attenuata. *Journal of comparative physiology*, 80(1):29–49, 1972.

[58] G KASSSIMON. Multiple excitation sites and straight-line conduction in contraction burst system of hydra. In *AMERICAN ZOOLOGIST*, 1970.

[59] William M Kier. The diversity of hydrostatic skeletons. *Journal of Experimental Biology*, 215(8):1247–1257, 2012.

[60] Jimin Kim, Julia A Santos, Mark J Alkema, and Eli Shlizerman. Whole integration of neural connectomics, dynamics and bio-mechanics for identification of behavioral sensorimotor pathways in caenorhabditis elegans. *bioRxiv*, page 724328, 2019.

[61] Jimin Kim and Eli Shlizerman. Deep reinforcement learning for neural control. *arXiv preprint arXiv:2006.07352*, 2020.

[62] Alexander Klimovich, Stefania Giacomello, Åsa Björklund, Louis Faure, Marketa Kaucka, Christoph Giez, Andrea P Murillo-Rincon, Ann-Sophie Matt, Doris Willoweit-Ohl, Gabriele Crupi, et al. Prototypical pacemaker neurons interact with the resident microbiota. *Proceedings of the National Academy of Sciences*, 117(30):17854–17863, 2020.

[63] Alexander V Klimovich and Thomas CG Bosch. Rethinking the role of the nervous system: lessons from the hydra holobiont. *BioEssays*, 40(9):1800060, 2018.

[64] Michèle Koenigsberger, Roger Sauser, Mathieu Lamboley, Jean-Louis Bény, and Jean-Jacques Meister. Ca2+ dynamics in a population of smooth muscle cells: modeling the recruitment and synchronization. *Biophysical journal*, 87(1):92–104, 2004.

[65] Michèle Koenigsberger, Dominique Seppey, Jean-Louis Bény, and Jean-Jacques Meister. Mechanisms of propagation of intercellular calcium waves in arterial smooth muscle cells. *Biophysical journal*, 99(2):333–343, 2010.

[66] Michael Kücken, Jordi Soriano, Pramod A Pullarkat, Albrecht Ott, and Ernesto M Nicola. An osmoregulatory basis for shape oscillations in regenerating hydra. *Biophysical journal*, 95(2):978–985, 2008.

[67] Ivana Y Kuo and Barbara E Ehrlich. Signaling in muscle contraction. *Cold Spring Harbor perspectives in biology*, 7(2):a006023, 2015.

[68] JMAM Kusters, MM Dernison, WPM Van Meerwijk, DL Ypey, APR Theuvenet, and CCAM Gielen. Stabilizing role of calcium store-dependent plasma membrane calcium channels in action-potential firing and intracellular calcium oscillations. *Biophysical journal*, 89(6):3741–3756, 2005.

[69] JMAM Kusters, WPM van Meerwijk, Dirk L Ypey, Alexander PR Theuvenet, and CCAM Gielen. Fast calcium wave propagation mediated by electrically conducted excitation and boosted by cicr. *American Journal of Physiology-Cell Physiology*, 294(4):C917–C930, 2008.

[70] Thibault Lagache, Alison Hanson, Adrienne Fairhall, and Rafael Yuste. Robust single neuron tracking of calcium imaging in behaving hydra. *bioRxiv*, 2020.

[71] Lucas Leclère and Eric Röttinger. Diversity of cnidarian muscles: function, anatomy, development and regeneration. *Frontiers in cell and developmental biology*, 4:157, 2017.

[72] J Lepault, AW McDowall, and CJP Grimmelikhuijzen. Intercellular junctions in nerve-free hydra. *Cell and tissue research*, 209(2):217–224, 1980.

[73] Luc Leybaert and Michael J Sanderson. Intercellular ca2+ waves: mechanisms and function. *Physiological reviews*, 92(3):1359–1392, 2012.

[74] Yue-Xian Li and John Rinzel. Equations for insp3 receptor-mediated [ca2+] i oscillations derived from a detailed kinetic model: a hodgkin-huxley like formalism. *Journal of theoretical Biology*, 166(4):461–473, 1994.

[75] SYLVIA J LILLY. Osmoregulation and ionic regulation in hydra. *Journal of Experimental Biology*, 32(2):423–439, 1955.

[76] Alessandro Loppini, Matthias Braun, Simonetta Filippi, and Morten Gram Pedersen.

Mathematical modeling of gap junction coupling and electrical activity in human β-cells. *Physical biology*, 12(6):066002, 2015.

[77] Jane Loveless, Konstantinos Lagogiannis, and Barbara Webb. Modelling the mechanics of exploration in larval drosophila. *PLoS computational biology*, 15(7):e1006635, 2019.

[78] GO Mackie. Conduction in the nerve-free epithelia of siphonophores. *American Zoologist*, 5(3):439–453, 1965.

[79] GO Mackie and LM Passano. Epithelial conduction in hydromedusae. *The Journal of general physiology*, 52(4):600–621, 1968.

[80] Martin Macklin and Robert K Josephson. The ionic requirements of transepithelial potentials in hydra. *The Biological Bulletin*, 141(2):299–318, 1971.

[81] Martin Macklin, Thomas Roma, and Kevin Drake. Water excretion by hydra. *Science*, 179(4069):194–195, 1973.

[82] Charles D Maggio, Scott R Jennings, Jennifer L Robichaux, Peter C Stapor, and James M Hyman. A modified hai–murphy model of uterine smooth muscle contraction. *Bulletin of mathematical biology*, 74(1):143–158, 2012.

[83] Chitaranjan Mahapatra, Keith L Brain, and Rohit Manchanda. A biophysically constrained computational model of the action potential of mouse urinary bladder smooth muscle. *PloS one*, 13(7), 2018.

[84] Johannes Martinek, Yvonne Stickler, Martin Reichel, Winfried Mayr, and Frank Rattay. A novel approach to simulate hodgkin–huxley-like excitation with comsol multiphysics. *Artificial organs*, 32(8):614–619, 2008.

[85] Alexander Mathis, Pranav Mamidanna, Kevin M Cury, Taiga Abe, Venkatesh N Murthy, Mackenzie Weygandt Mathis, and Matthias Bethge. Deeplabcut: markerless pose estimation of user-defined body parts with deep learning. *Nature neuroscience*, 21(9):1281–1289, 2018.

[86] CB McCullough. Pacemaker interaction in hydra. *American zoologist*, 5(3):499–504, 1965.

[87] William MacDonald Megill. *The biomechanics of jellyfish swimming*. PhD thesis, University of British Columbia, 2002.

[88] Andrea P Murillo-Rincon, Alexander Klimovich, Eileen Pemöller, Jan Taubenheim, Benedikt Mortzfeld, René Augustin, and Thomas CG Bosch. Spontaneous body contractions are modulated by the microbiome of hydra. *Scientific reports*, 7(1):1–9, 2017.

[89] Suyash Naik, Manu K Unni, Devanshu Sinha, Shatruhan Singh Rajput, Chandramouli Reddy Puli, Apratim Chatterji, Shivprasad Patil, and Sanjeev Galande. Differential tissue stiffness of body column facilitates locomotion of hydra on solid substrates. *bioRxiv*, 2020.

[90] Yukihiko Noro, Seungshic Yum, Chiemi Nishimiya-Fujisawa, Christina Busse, Hiroshi Shimizu, Katsuhiko Mineta, Xiaoming Zhang, Thomas W Holstein, Charles N David, Takashi Gojobori, et al. Regionalized nervous system in hydra and the mechanism of its development. *Gene Expression Patterns*, 31:42–59, 2019.

[91] Erick Olivares, Eduardo J Izquierdo, and Randall D Beer. A neuromechanical model of multiple network rhythmic pattern generators for forward locomotion in c. elegans. *Frontiers in computational neuroscience*, 15:10, 2021.

[92] Fabian Pallasdies, Sven Goedeke, Wilhelm Braun, and Raoul-Martin Memmesheimer. From single neurons to behavior in the jellyfish aurelia aurita. *Elife*, 8:e50084, 2019.

[93] LM Passano and CB McCullough. The light response and the rhythmic potentials of hydra. *Proceedings of the National Academy of Sciences of the United States of America*, 48(8):1376, 1962.

[94] LM Passano and CB McCullough. Pacemaker hierarchies controlling the behaviour of hydras. *Nature*, 199(4899):1174–1175, 1963.

[95] LM Passano and CB McCullough. Co-ordinating systems and behaviour in hydra: I. pacemaker system of the periodic contractions. *Journal of Experimental Biology*, 41(3):643–664, 1964.

[96] LM Passano and CB McCullough. Co-ordinating systems and behaviour in hydra ii. the rhythmic potential system. *Journal of Experimental Biology*, 42(2):205–231, 1965.

[97] A. Rajagopal, C. L. Dembia, M. S. DeMers, D. D. Delp, J. L. Hicks, and S. L. Delp. Full-body musculoskeletal model for muscle-driven simulation of human gait. *IEEE Transactions on Biomedical Engineering*, 63(10):2068–2079, 2016.

[98] Lei Ren, Richard K Jones, and David Howard. Predictive modelling of human walking over a complete gait cycle. *Journal of biomechanics*, 40(7):1567–1574, 2007.

[99] Sandy Rihana, Jeremy Terrien, Guy Germain, and Catherine Marque. Mathematical modeling of electrical activity of uterine muscle cells. *Medical & biological engineering & computing*, 47(6):665–675, 2009.

[100] RSl Rivlin. Large elastic deformations of isotropic materials. i. fundamental concepts. *Philosophical Transactions of the Royal Society of London. Series A, Mathematical and Physical Sciences*, 240(822):459–490, 1948.

[101] Dave Rudolf and David Mould. An interactive fluid model of jellyfish for animation. In *International Conference on Computer Vision, Imaging and Computer Graphics*, pages 59–72. Springer, 2009.

[102] Norman B Rushforth. Behavioral and electrophysiological studies of hydra. i. analysis of contraction pulse patterns. *The Biological Bulletin*, 140(2):255–273, 1971.

[103] Norman B Rushforth, Allison L Burnett, and Richard Maynard. Behavior in hydra: contraction responses of hydra pirardi to mechanical and light stimuli. *Science*, 139(3556):760–761, 1963.

[104] Panagiotis Sakagiannis, Anna-Maria Jürgensen, and Martin Paul Nawrot. A realistic locomotory model of drosophila larva for behavioral simulations. *bioRxiv*, 2021.

[105] Kazuma Sakamoto, Zu Soh, Michiyo Suzuki, Yuichi Iino, and Toshio Tsuji. Forward and backward locomotion patterns in c. elegans generated by a connectome-based model simulation. *Scientific Reports*, 11(1):1–13, 2021.

[106] PA Sarma, RM Pidaparti, PN Moulik, and RA Meiss. Non-linear material models for tracheal smooth muscle tissue. *Bio-medical materials and engineering*, 13(3):235–245, 2003.

[107] Caroline A Schneider, Wayne S Rasband, and Kevin W Eliceiri. Nih image to imagej: 25 years of image analysis. *Nature methods*, 9(7):671–675, 2012.

[108] Stefan Schuster, Marko Marhl, and Thomas Höfer. Modelling of simple and complex calcium oscillations: From single-cell responses to intercellular signalling. *European Journal of Biochemistry*, 269(5):1333–1355, 2002.

[109] Stefan Siebert, Jeffrey A Farrell, Jack F Cazet, Yashodara Abeykoon, Abby S Primack, Christine E Schnitzler, and Celina E Juliano. Stem cell differentiation trajectories in hydra resolved at single-cell resolution. *Science*, 365(6451):eaav9314, 2019.

[110] BA Skierczynski, RJA Wilson, WB Kristan Jr, and R Skalak. A model of the hydrostatic skeleton of the leech. *Journal of theoretical biology*, 181(4):329–342, 1996.

[111] JAMES Sneyd, BT Wetton, ANDREW C Charles, and MICHAEL J Sanderson. Intercellular calcium waves mediated by diffusion of inositol trisphosphate: a two-dimensional model. *American Journal of Physiology-Cell Physiology*, 268(6):C1537–C1545, 1995.

[112] John R Szymanski and Rafael Yuste. Mapping the whole-body muscle activity of hydra vulgaris. *Current Biology*, 29(11):1807–1817, 2019.

[113] Cloe Taddei-Ferretti and S Chillemi. Modulation of hydra attentuata rhythmic activity. *Biological cybernetics*, 56(4):225–235, 1987.

[114] Cloe Taddei-Ferretti and Carlo Musio. The neural net of hydra and the modulation of

its periodic activity. In *International Work-Conference on Artificial Neural Networks*, pages 123–137. Springer, 1999.

[115] Yasuharu Takaku, Jung Shan Hwang, Alexander Wolf, Angelika Böttger, Hiroshi Shimizu, Charles N David, and Takashi Gojobori. Innexin gap junctions in nerve cells coordinate spontaneous contractile behavior in hydra polyps. *Scientific reports*, 4:3573, 2014.

[116] CY Tang, G Zhang, and CP Tsui. A 3d skeletal muscle model coupled with active contraction of muscle fibres and hyperelastic behaviour. *Journal of biomechanics*, 42(7):865–872, 2009.

[117] Ulrich Technau and Robert E Steele. Evolutionary crossroads in developmental biology: Cnidaria. *Development*, 138(8):1447–1458, 2011.

[118] Craig P Testrow, Arun V Holden, Anatoly Shmygol, and Henggui Zhang. A computational model of excitation and contraction in uterine myocytes from the pregnant rat. *Scientific reports*, 8(1):1–14, 2018.

[119] Lena H Ting and Hillel J Chiel. Muscle, biomechanics, and implications for neural control. *Neurobiology of Motor Control: Fundamental Concepts and New Directions*, pages 365–416, 2017.

[120] Wing-Chiu Tong, Cecilia Y Choi, Sanjay Karche, Arun V Holden, Henggui Zhang, and Michael J Taggart. A computational model of the ionic currents, ca2+ dynamics and action potentials underlying contraction of isolated uterine smooth muscle. *PloS one*, 6(4), 2011.

[121] Abraham Trembley. *Mémoires pour servir à l'histoire d'un genre de ploypes d'eau douce, à bras en forme de cornes*, volume 1. Durand, 1744.

[122] Constantine N Tzouanas, Soonyoung Kim, Krishna N Badhiwala, Benjamin W Avants, and Jacob T Robinson. Hydra vulgaris shows stable responses to thermal stimulation despite large changes in the number of neurons. *Iscience*, 24(6):102490, 2021.

[123] Martin Wadepuhl and Wolf-Jürgen Beyn. Computer simulation of the hydrostatic skeleton. the physical equivalent, mathematics and application to worm-like forms. *Journal of theoretical biology*, 136(4):379–402, 1989.

[124] Nancy Wanek, Beverly A Marcum, Hsueh-Tze Lee, Margaret Chow, and Richard D Campbell. Effect of hydrostatic pressure on morphogenesis in nerve-free hydra. *Journal of Experimental Zoology*, 211(3):275–280, 1980.

[125] Inga Wang, Antonio Z Politi, Nessy Tania, Yan Bai, Michael J Sanderson, and James Sneyd. A mathematical model of airway and pulmonary arteriole smooth muscle. *Biophysical journal*, 94(6):2053–2064, 2008.

[126] Rui Wang, Tapan Goel, Kate Khazoyan, Ziad Sabry, Heng J Quan, Patrick H Diamond, and Eva-Maria S Collins. Mouth function determines the shape oscillation pattern in regenerating hydra tissue spheres. *Biophysical journal*, 117(6):1145–1155, 2019.

[127] Jane A Westfall. Ultrastructural evidence for a granule-containing sensory-motor-interneuron in hydra littoralis. *Journal of ultrastructure research*, 42(3-4):268–282, 1973.

[128] Richard L Wood and Aileen M Kuda. Formation of junctions in regeneratin hydra: Gap junctions. *Journal of ultrastructure research*, 73(3):350–360, 1980.

[129] Wataru Yamamoto and Rafael Yuste. Whole-body imaging of neural and muscle activity during behavior in hydra vulgaris: effect of osmolarity on contraction bursts. *Eneuro*, 7(4), 2020.

[130] Yoram Yekutieli, Roni Sagiv-Zohar, Ranit Aharonov, Yaakov Engel, Binyamin Hochner, and Tamar Flash. Dynamic model of the octopus arm. i. biomechanics of the octopus reaching movement. *Journal of neurophysiology*, 94(2):1443–1458, 2005.

[131] Yoram Yekutieli, Roni Sagiv-Zohar, Binyamin Hochner, and Tamar Flash. Dynamic model of the octopus arm. ii. control of reaching movements. *Journal of neurophysiology*, 94(2):1459–1468, 2005.

[132] Maxime Yochum, Jérémy Laforêt, and Catherine Marque. An electro-mechanical multiscale model of uterine pregnancy contraction. *Computers in biology and medicine*, 77:182–194, 2016.

[133] Seungshic Yum, Toshio Takahashi, Osamu Koizumi, Yuki Ariura, Yoshitaka Kobayakawa, Shirou Mohri, and Toshitaka Fujisawa. A novel neuropeptide, hym-176, induces contraction of the ectodermal muscle in hydra. *Biochemical and biophysical research communications*, 248(3):584–590, 1998.

[134] Aref Arzan Zarin, Brandon Mark, Albert Cardona, Ashok Litwin-Kumar, and Chris Q Doe. A multilayer circuit architecture for the generation of distinct locomotor behaviors in drosophila. *Elife*, 8:e51781, 2019.

SUPPLEMENTARY INFORMATION

Single cell model details

Here we give the details of the single cell model (Eq. 1 of the main text), and annotate their sources. Differential equations are solved using the Euler method with a step size of 0.2 ms.

Expressions

Ca^{2+} flux through IPR [3]:

$$J_{\mathrm{IPR}} = k_{\mathrm{IPR}} \frac{C^2 P^2 R}{(C^2 + K_{\mathrm{a}}^2)(P^2 + K_{\mathrm{IP}}^2)} (S - C)$$
$$\frac{\mathrm{d}R}{\mathrm{d}t} = k_R \left(\frac{K_{\mathrm{i}}^2}{K_{\mathrm{i}}^2 + C^2} - R \right)$$

Ca^{2+} flux leaking from ER [3]:

$$J_{\mathrm{leak}} = k_{\mathrm{leak}} (S - C)$$

Ca^{2+} flux through the SERCA pump [3]:

$$J_{\mathrm{SERCA}} = k_{\mathrm{SERCA}} C$$

Ca^{2+} flux through PMCA pump [3]:

$$J_{\mathrm{PMCA}} = k_{\mathrm{PMCA}} C$$

Ca^{2+} entry fluxes from the extracellular space [3]:

$$J_{\mathrm{in}} = v_{\mathrm{in}} + v_r \frac{P^2}{K_r^2 + P^2}$$

Current through voltage-gated Ca^{2+} channels [1]:

$$
\begin{aligned}
I_{\mathrm{Ca}} &= g_{\mathrm{Ca}} m^2 h (V - E_{\mathrm{Ca}}) \\
\frac{\mathrm{d}m}{\mathrm{d}t} &= \frac{m_\infty - m}{\tau_m} \\
\frac{\mathrm{d}h}{\mathrm{d}t} &= \frac{h_\infty - h}{\tau_h} \\
m_\infty &= \frac{1}{1 + \exp(-\frac{V+25}{10})} \\
\tau_m &= \frac{0.001}{\exp\left(-\frac{V+23}{20}\right) + \exp\left(\frac{V+23}{20}\right)} + 0.00005 \\
h_\infty &= \frac{1}{1 + \exp(\frac{V+28}{5})} \\
\tau_h &= \frac{0.03}{\exp\left(-\frac{V}{20}\right) + \exp\left(\frac{V}{20}\right)} + 0.021
\end{aligned}
$$

Current through voltage-gated K^+ channels [1]:

$$
\begin{aligned}
I_{\mathrm{K}} &= g_{\mathrm{K}} n^4 (V - E_{\mathrm{K}}) \\
\frac{\mathrm{d}n}{\mathrm{d}t} &= \frac{n_\infty - n}{\tau_n} \\
n_\infty &= \frac{1}{1 + \exp(-\frac{V+18.5}{23})} \\
\tau_n &= \frac{0.0015}{\exp\left(-\frac{V+10}{25}\right) + \exp\left(\frac{V+10}{25}\right)} + 0.015
\end{aligned}
$$

Leak current:

$$
I_{\mathrm{L}} = g_{\mathrm{L}} (V - E_{\mathrm{L}})
$$

Parameters

The related parameters are shown in Table S1.

Calcium fluxes and ion currents

Fig. S1 includes the supplementary plots of Fig. 3B and 3C of the main text, showing the calcium fluxes and ion currents related to the dynamics.

Equilibrium requirements

To maintain the cell in the equilibrium state with no external stimulation, several equilibrium conditions need to be held at the initiation.

The equilibrium of membrane currents:

$$I_{\mathrm{Ca}} + I_{\mathrm{K}} + I_{\mathrm{L}} = 0$$

The equilibrium of Ca^{2+} fluxes through the cell membrane:

$$J_{\mathrm{in}} - J_{\mathrm{PMCA}} - \alpha I_{\mathrm{Ca}} = 0$$

The equilibrium of Ca^{2+} fluxes through the ER membrane:

$$J_{\mathrm{IPR}} + J_{\mathrm{leak}} - J_{\mathrm{SERCA}} = 0$$

Initial values of the dynamical variables are set as equilibrium values of these equations.

Multicellular model details

Calibration of the size of muscle sheets

To simulate calcium signaling in the whole-body muscle sheets, we construct ectodermal and endodermal networks of *Hydra* epitheliomuscular cells. The number of muscle cells of *Hydra* varies considerably with body size [5]. For a representative *Hydra* of length of 1.38 mm, we counted 62 cells longitudinally and 30 (15×2) - 34 (17×2) cells circumferentially, depending on the longitudinal location (Fig. S2). We approximate the body column as a cylinder composed of 30×60 square cells, of which the side length is 30 μm; the lateral sheet edges are connected and the topmost and bottommost cell rows are taken to be isolated from the environment. Cells within a layer are connected to their neighbours via gap junctions.

Sensitivity analysis of stimulation strength

As shown in Table S1, we set the stimulation strength of the slow pathway ($v_{\mathrm{PLC}\beta}$) as 1.0 μM/s and that of the fast pathway (I_{stim}) as 0.02 mA/cm^2. To explore how these values affect the results, we sweep them over an order of magnitude (0.1 - 1.0 for the slow wave; 0.004 - 0.04 for the fast wave) and plot how these inputs influence the longitudinal [Ca^{2+}] propagation, given stimulation of a local (2×2 cells) domain at the center of a 30×60 muscle sheet (Fig. S3). The wavefront index is defined as the maximum index of cells whose [Ca^{2+}] concentration is higher than a threshold (0.055 μM). The results show a clear phase transition of fast wave propagation when I_{stim} is between 0.016 - 0.02 mA/cm^2, which does not appear in the slow wave.

When the stimulation strengths are small, both the slow pathway and fast pathway propagate in a form of diffusion (not shown); when the strengths are large, the slow pathway gradually exhibits a diffusive-wave propagation pattern, while the fast pathway suddenly transitions to a regenerative-wave propagation pattern when the input strength exceeds a threshold.

Effects of gap-junctional coupling coefficients on wave propagation

We explore the effects of the gap-junctional coupling coefficients g_{IP_3} and g_{c} (in units of s^{-1}) by tuning their values along with longitudinal and circular directions and visualizing how they will affect the propagation range of the slow waves and the propagation speed of the fast waves, with the values of all other parameters fixed. Both are again initiated by stimulating a domain of 2×2 cells at the center of a 30×60 muscle sheet (Fig. S4). In both cases, a larger coupling coefficient facilitates the propagation in that direction, and reduces the propagation in the orthogonal direction. The default values used in our simulation are: $g_{\mathrm{c}} = 1000$ s^{-1} for both longitudinal and circular directions; $g_{\mathrm{IP}_3} = 2$ s^{-1} for the longitudinal direction and 0.1 s^{-1} for the circular direction.

The reason that use different criteria to measure the slow and fast waves is due to the different natures between them: the amplitude of slow wave is significantly decaying with the propagation distance and ceases at some point, and we found the average speed (which

is strongly affected by how we set the threshold to define wavefront) is not a good metric to measure the strength of wave propagation, instead, the farthest wavefront which shows "how far" the wave can propagate can perfectly reflect that; as for the fast wave, since it's global which means it finally activates all cells, the farthest wavefront is just the border of the sheet which is trivial, so the speed which shows "how fast" the wave can reach the border plays a good metric.

Effects of intracellular parameters on wave propagation

Besides the coupling coefficients, some intracellular parameters that influence the strength or duration of the calcium dynamics can also affect wave propagation. We select some significant parameters here and explore their effects by sweeping them and measure the effects on propagation range (slow wave) or speed (fast wave) along the longitudinal direction under local stimulation (2×2 cells at the center) (Fig. S5), with all other parameters fixed. Fig. S5A shows that both larger k_{IPR} or smaller k_{deg} can make the wave propagate farther – this is expected as a larger k_{IPR} indicates a larger calcium release from ER stores when IPR is activated by IP_3, and a smaller k_{deg} means the IP_3 decays more slowly. Both effects will cause stronger calcium dynamics and facilitate wave propagation. Fig. S5B shows that increasing either k_{SERCA} or k_{PMCA} limits the maximum wave range, which is again reasonable since both factors are proportional to the extent that Ca^{2+} is recycled (k_{SERCA}) or extruded (k_{PMCA}) from the cytosol; therefore their increase results in a reduction in cytosolic Ca^{2+} concentration and hinders wave propagation. Fig. S5C shows larger g_{Ca} greatly facilitates the propagation speed of the fast wave, which can be due to the increase of Ca^{2+} influx from the extracellular space; larger g_{K} can increase the Ca^{2+} efflux from the cytosol to extracellular space, thus reducing the strength of the calcium dynamics and hindering fast wave propagation.

Force generation model details

As given in Eq. 2 in the main text, we use the Hai-Murphy model to transform the Ca^{2+} dynamics into contracting stress patterns, and set different parameters for the ectoderm (phasic muscle) and endoderm (tonic muscle). The details of these parameters are shown

in Table S2. Parameters are tuned to fit the length change of the model to that of the corresponding measured *Hydra*, based on the ranges and values provided in [2] and [6].

Biomechanics details

The parameters of our biomechanical model, constructed in COMSOL Multiphysics 5.3a, are shown in Table S3. The configurations of the solver are shown in Table S4.

Effects of parameter variations on length change

Fig. S7 shows how some key parameters can affect the length change of the model under a series of contraction pulse stimuli, with other parameters fixed. The stimulation train is extracted from measurements of real *Hydra*.

Model reduction

To explore the high-level properties of the biophysical model, we apply a pointwise (a domain of 2×2 cells) pulse stimulation at the middle of the muscle sheet and plot the generated wave dynamics ($[Ca^{2+}]_i$) along with the center longitudinal line for both slow and fast dynamics (Fig. S8A, B). Based on the plots, we propose a Green's function form for both slow and fast waves:

$$G(\rho,t) = A\Theta\left(t-\frac{\rho}{v}\right)\left(1-e^{-\frac{t-\rho/v}{\tau_{\text{inc}}}}\right)e^{-\frac{t-\rho/v}{\tau_{\text{dec}}}}e^{-\frac{\rho}{\rho_c}}$$

where $\Theta(\cdot)$ is the Heaviside function, ρ is the distance between a point and the source, t is the time since the stimulation, A is the maximum amplitude constant, v is the velocity of the wave propagation, τ_{inc} is the time constant of the increasing phase, τ_{dec} is the time constant of the decreasing phase, ρ_c is the scaling constant of the amplitude. To represent the anisotropy of the coupling coefficients of slow waves, we define the distance as $\rho = \sqrt{(c_w x)^2 + y^2}$, where x, y are the distance between the point and the source respectively in the circular and longitudinal direction, c_w is a warping coefficient that represents the anisotropy. Warping the space is equivalent to defining directional velocities but simpler to represent.

We fit the Green's function by sweeping over the key parameters ($A, v, \tau_{\text{inc}}, \tau_{\text{dec}}, \rho_c$ and c_w) to match some selected targets: we firstly select a point on the sheet, then sweep τ_{inc}, τ_{dec} and A to fit its amplitude and the time of its increasing and decreasing phases, by picking the combination that minimizes the difference between the Green's function and the biophysical model. Then we select two points that are far from each other, then sweep v, ρ_c and c_w to fit their time difference and amplitude difference, picking the pair that gives a closest result with the biophysical model. The optimized values of these parameters are shown in Table S5, and the spatiotemporal pattern of the Green's function along with the center longitudinal line for the slow and fast dynamics are shown in (Fig. S8C, D).

Though the Green's function reproduces some characteristics of the biophysical model, its biggest limitation is it can only represent linear responses. However, our biophysical model includes strong nonlinearity in both single-cellular dynamics and the inter-cellular interactions. For instance, the refractory period of the action potential and the depletion of ER store make that when two fast waves or two slow waves collide with each other, they exhibit some extent of canceling (an example of the fast wave is shown in Fig. S9). Also, the wave-shapes of different cells differ a lot in the biophysical model simulation, so some parameters that are fitted with one or two arbitrary points are not generally accurate. Better simplification needs incorporating more nonlinearity and therefore greatly increases the problem complexity, and our attempt with Green's functions is a start that may inspire the future work.

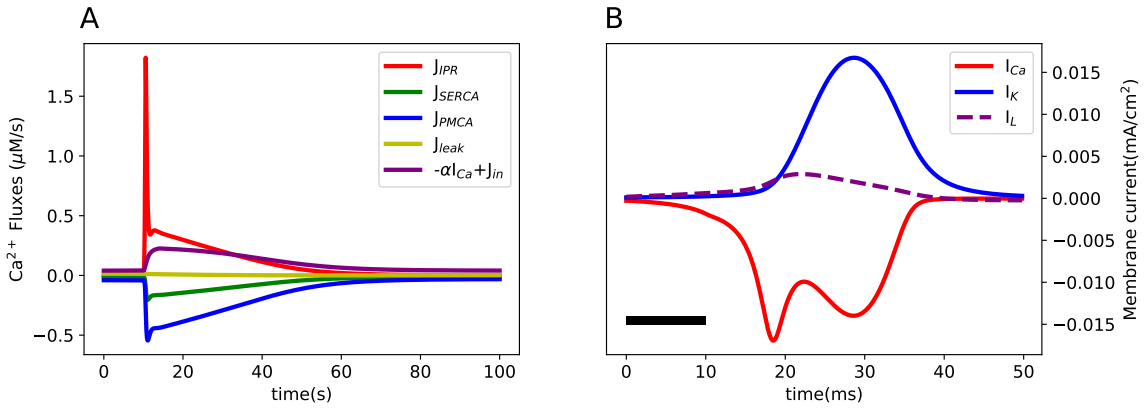

Figure S1: Calcium fluxes (A) and ion currents (B), respectively correspond to Fig. 3A and Fig. 3B in the main text.

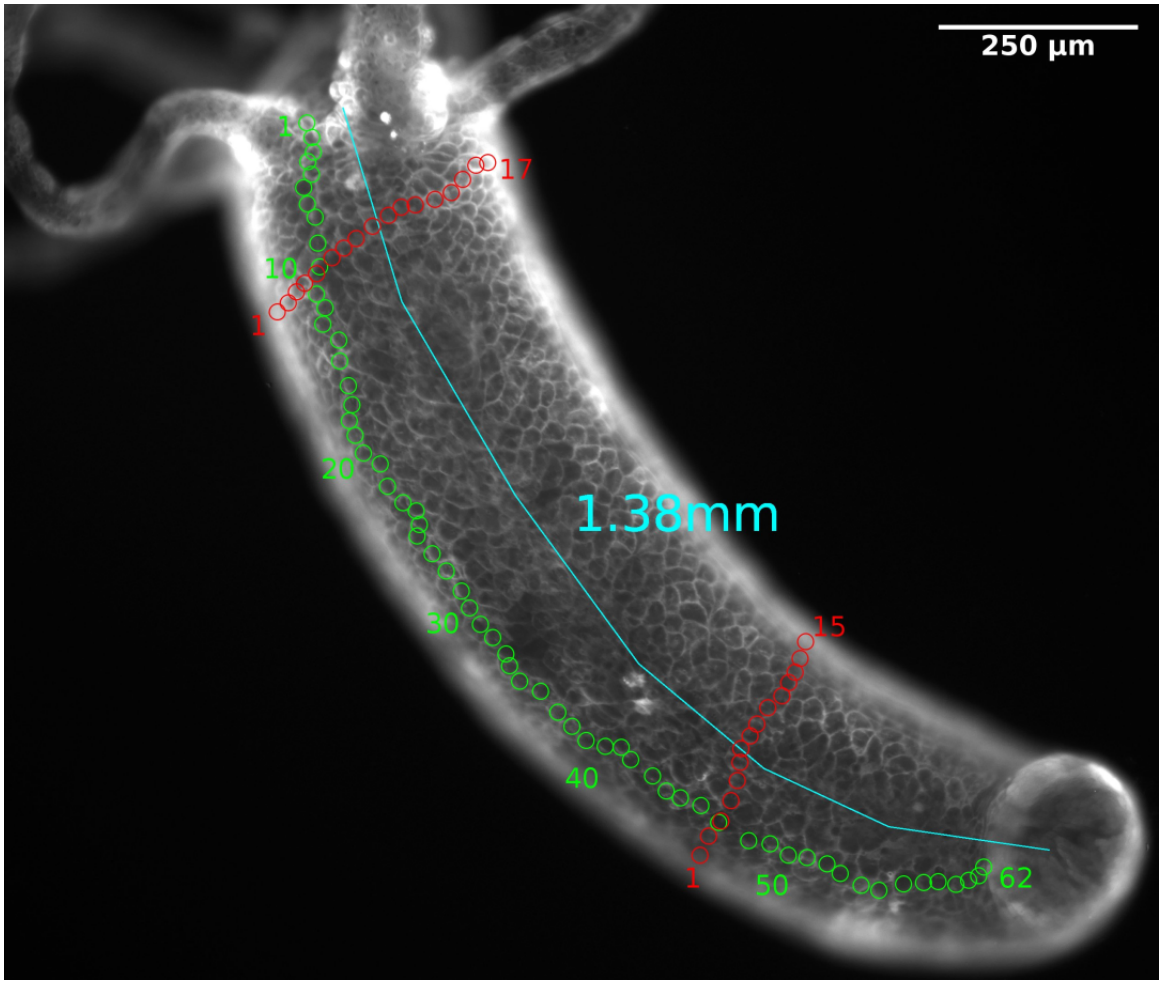

Figure S2: Cell counting and length measurement in a small *Hydra*. Green circles are the counts in longitudinal direction and red colors are the counts in circumferential direction.

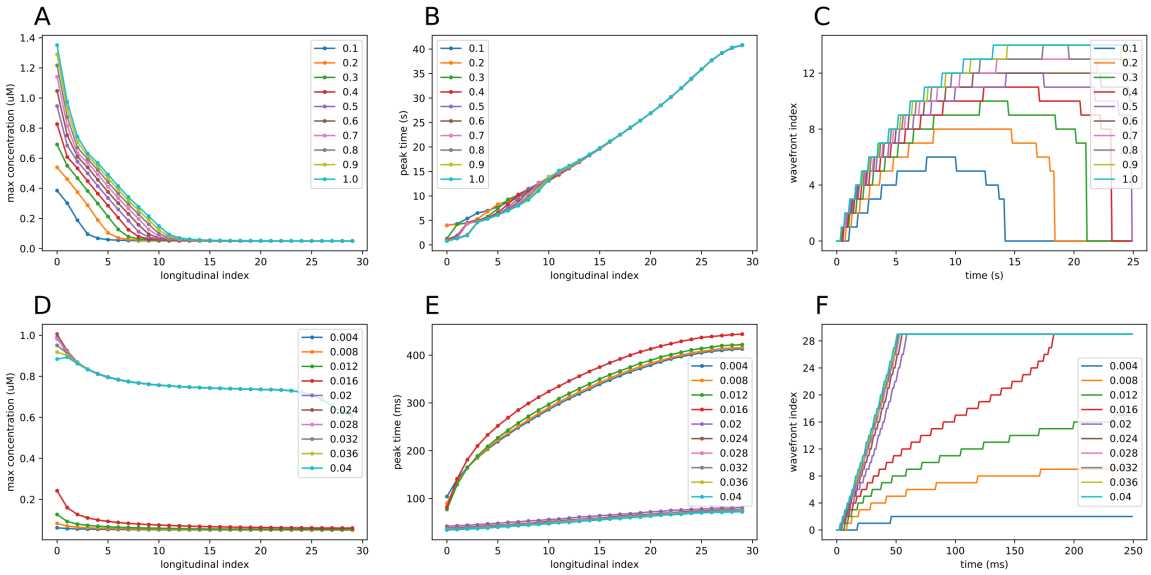

Figure S3: Observables of $[Ca^{2+}]$ propagation change with different stimulation strengths of the slow wave (A - C) and the fast wave (D - F), including the distribution of maximum concentration (amplitude) over longitudinal index (A, D), the arrival time of peaks versus the longitudinal index (B, E) and the wavefront index change over time (C, F).

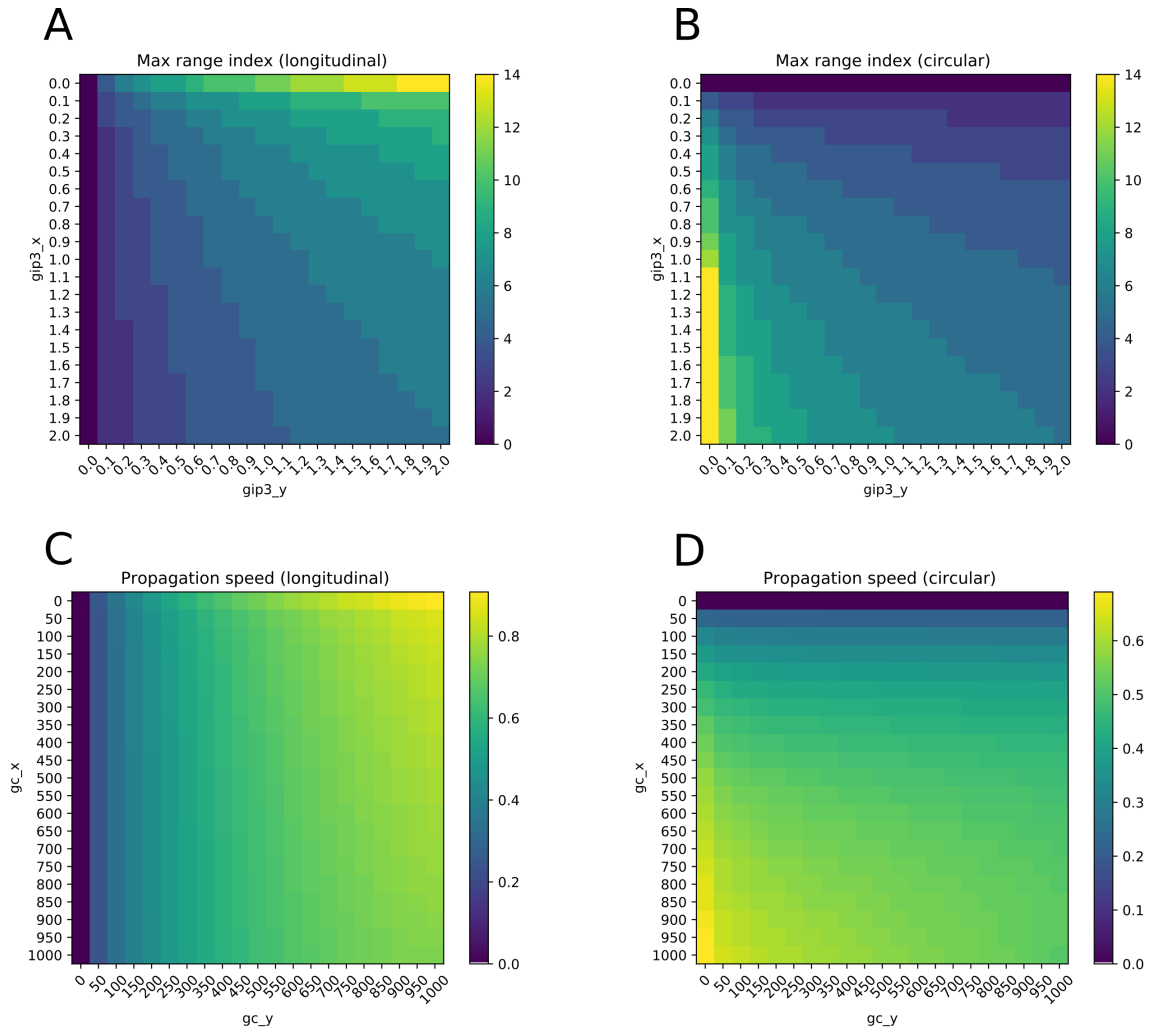

Figure S4: Effects of gap-junctional coupling coefficients on wave propagation. (A) The effect of g_{IP_3} on the longitudinal range of the slow wave. (B) The effect of g_{IP_3} on the circular range of the slow wave. (C) The effect of g_{c} on the longitudinal propagation speed of the fast wave. (D) The effect of g_{c} on the circular propagation speed of the fast wave.

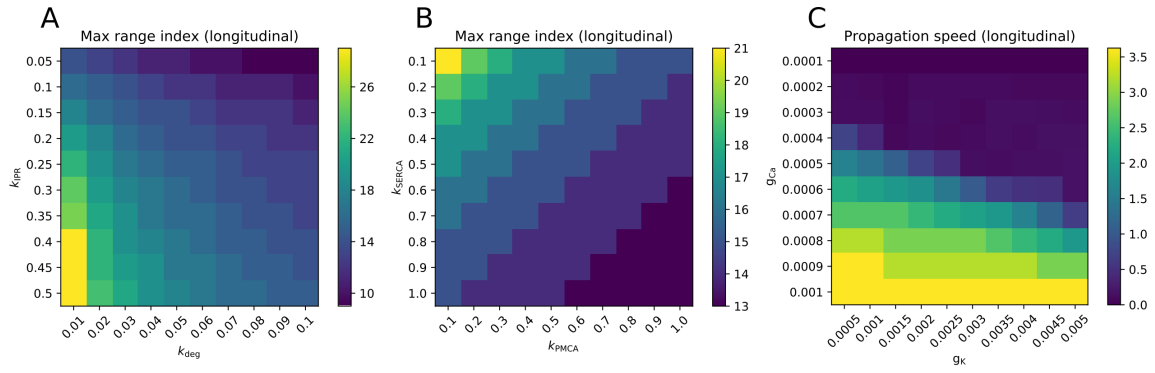

Figure S5: Effects of intracellular parameters on wave propagation. (A) Effects of sweeping k_{IPR} and k_{deg} on the longitudinal range of the slow wave. (B) Effects of sweeping k_{SERCA} and k_{PMCA} on the longitudinal range of the slow wave. (C) Effects of sweeping g_{Ca} and g_{K} on the longitudinal propagation speed of the fast wave.

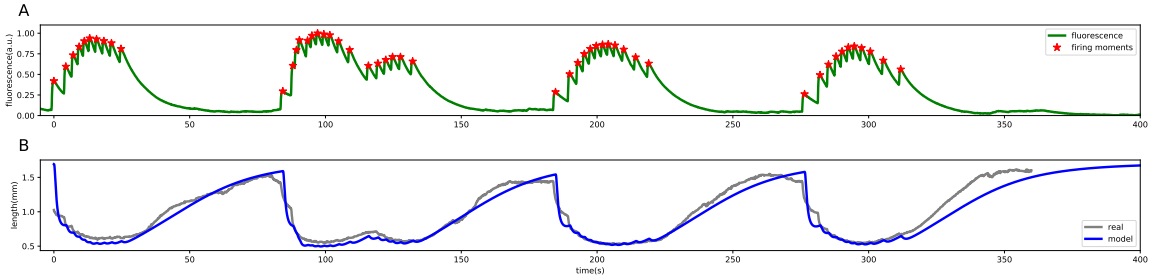

Figure S6: Simulation following another video where two bursts are consecutive. (A) whole-frame fluorescence trace and neural firing moments; (B) comparison between length evolution of the model and the real *Hydra* in the video.

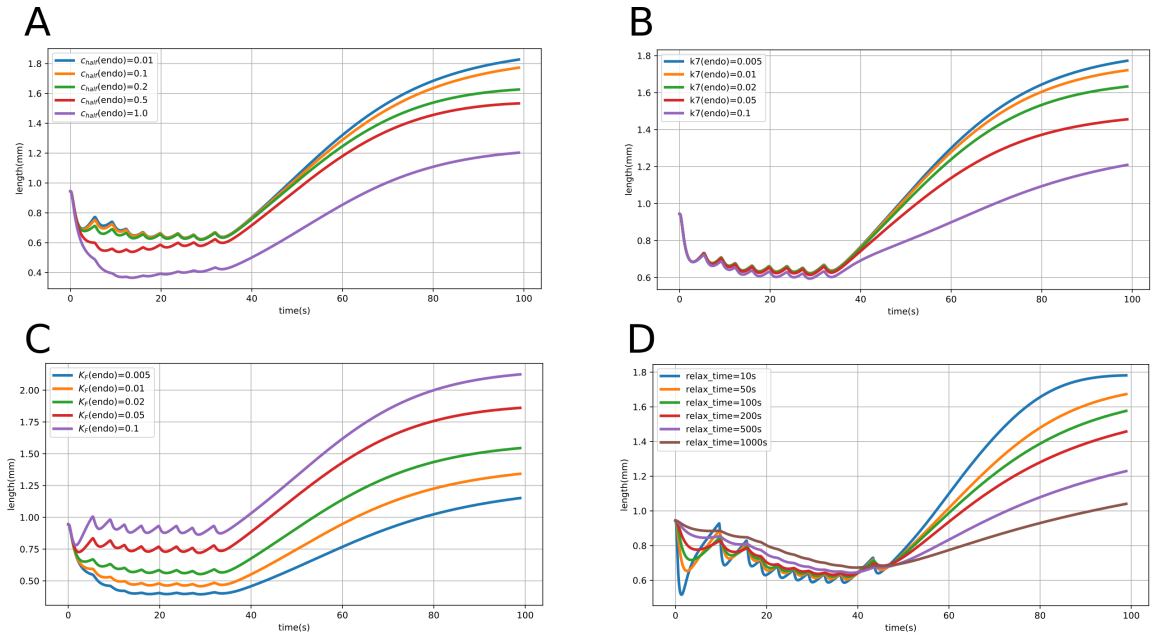

Figure S7: Effect on the length change by sweeping different parameters: (A) Endodermal c_{half}; (B) Endodermal k_7; (C) Endodermal K_F; (D) relaxation time (representing viscosity).

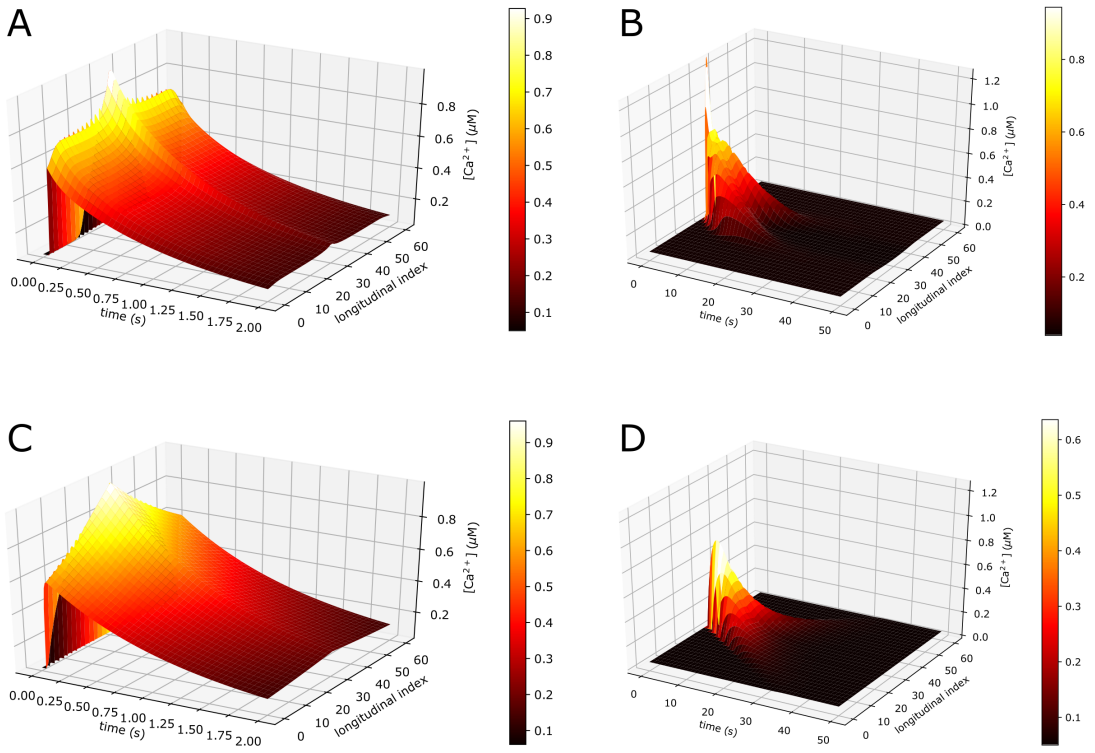

Figure S8: Spatiotemporal pattern of the impulse response of the longitudinal center-line points in the biophysical model and Green's function. (A) Biophysical model response to a fast pathway stimulation. (B) Biophysical model response to a slow pathway stimulation. (C) Green's function of the fast wave. (D) Green's function of the slow wave.

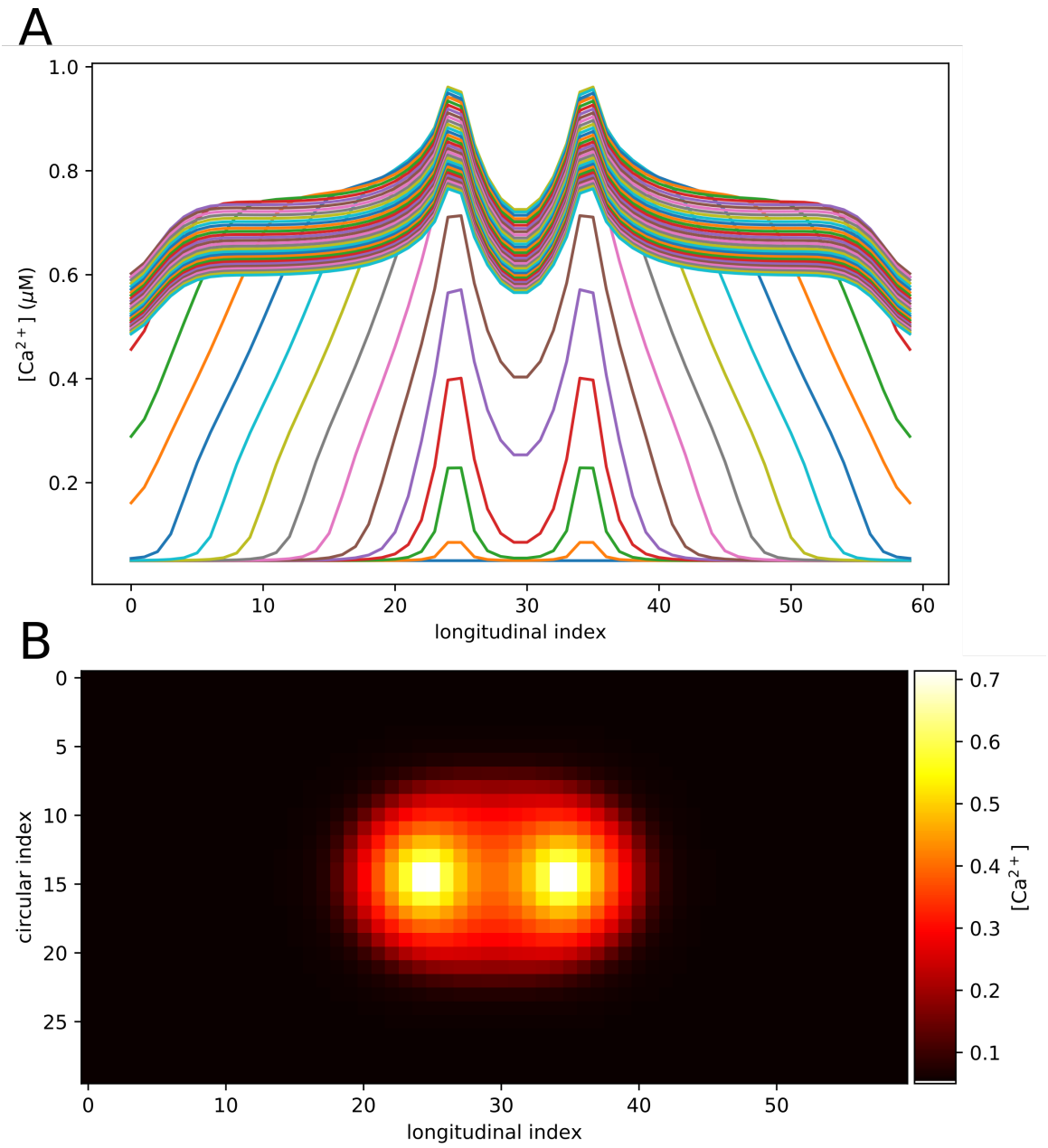

Figure S9: Nonlinearity exhibited by the interaction of two pointwise-stimulated fast waves. (A) Traces showing how $[Ca^{2+}]_i$ evolves, in which each curve represents a time point. (B) Snapshot of the muscle sheet at 25 ms after the stimulation, in which two waves cancel each other at the middle.

Table S1: Parameters used in the single cell model

Parameter	Description	Value	Unit	Source
k_{IPR}	Rate constant of Ca^{2+} release through IPR	0.2	s^{-1}	[3]*
k_R	Rate constant of IPR inactivation	4	s^{-1}	[3]
K_{a}	Half-saturation constant for Ca^{2+} activation of IPR	0.2	μM	[3]
K_{i}	Half-saturation constant for Ca^{2+} inhibition of IPR	0.2	μM	[3]
K_{IP}	Half-saturation constant for IP_3 activation of IPR	0.3	μM	[3]
k_{leak}	Rate constant of Ca^{2+} leak from ER	0.0002	s^{-1}	[3]*
k_{SERCA}	Rate constant of SERCA pump	0.3	s^{-1}	[3]*
k_{PMCA}	Rate constant of PMCA pump	0.8	s^{-1}	[3]*
v_{in}	Rate of Ca^{2+} leak across the plasma membrane	0.04	μM/s	[3]*
v_{r}	Maximal rate of activation-dependent Ca^{2+} influx	0.2	μM/s	[3]
K_{r}	Half-saturation constant for activation-dependent Ca^{2+} entry	1	μM	[3]
$v_{\mathrm{PLC}\beta}$	Rate of PLCβ	0.002 - 1.0	μM/s	[3]*
k_{deg}	Rate constant of IP_3 degradation	0.05	s^{-1}	[3]*
α	Current conversion factor	5182.13	μM·cm^2/mC	[4]
β	Ratio of the volumes of cytoplasm and ER	20	1	[3]
g_{Ca}	Maximal conductance of I_{Ca}	0.0005	S/cm^2	[4]*
E_{Ca}	Reversal potential of I_{Ca}	51	mV	[4]
g_{K}	Maximal conductance of I_{K}	0.0025	S/cm^2	[4]*
E_{K}	Reversal potential of I_{K}	-75	mV	[4]
g_{L}	Conductance of I_{L}	0.000036	S/cm^2	*
E_{L}	Reversal potential of I_{L}	-55	mV	*
C_m	Membrane capacitance per unit area	1	μF/cm^2	[4]
I_{stim}	Current through ligand-gated ion channels	0 - 0.02	mA/cm^2	[4]

* Modified or tuned in the physiological plausible range.

Table S2: Parameters used in the modified Hai-Murphy model

Parameter	Description	Value	Unit
k_1	Rate of $M \to Mp$	$\frac{C^{n_M}}{c_{\text{half}}^{n_M} + C^{n_M}}$	s^{-1}
k_2	Rate of $Mp \to M$	0.15	s^{-1}
k_3	Rate of $A + Mp \to AMp$	16 (ecto) / 0.4 (endo)	s^{-1}
k_4	Rate of $AMp \to A + Mp$	4 (ecto) / 0.05 (endo)	s^{-1}
k_5	Rate of $AMp \to AM$	k_2	s^{-1}
k_6	Rate of $AM \to AMp$	k_1	s^{-1}
k_7	Rate of $AM \to A + M$	0.75 (ecto) / 0.015 (endo)	s^{-1}
c_{half}	Half-saturation $[Ca^{2+}]_i$ for MLCK activation	0.85 (ecto) / 0.15 (endo)	μM
n^M	Hill coefficient of Ca^{2+} activation of MLCK	4	1
K_F	Proportional coefficient of active stress generation	3.3 (ecto) / 0.3 (endo)	N/mm^2

Table S3: Parameters used in the COMSOL model

Parameter	Value	Unit
Top half sphere radius	97.5	μm
Bottom half sphere radius	97.5	μm
Body cylinder height	650	μm
Thickness	19.5	μm
Density of Enclosed Fluid	1000	kg/m^3
Density of Muscle	1200	kg/m^3
Lamé parameter μ of Muscle	3.336	kPa
Lamé parameter λ of Muscle	1.664	GPa
Initial bulk modulus of muscle	1.667	GPa
Relaxation time of muscle	70	s
Temperature	293.15	K
Time step	0.1	s

Table S4: COMSOL solver configurations

Option	Value
Time stepping method	BDF
Steps taken by solver	Intermediate
Initial step	0.001 s
Maximum step	0.1 s
Maximum BDF order	2
Minimum BDF order	1
Event tolerance	0.01
Nonlinear controller	True
Singular mass matrix	Maybe
Consistent initialization	Backward Euler
Fraction of initial step fore Backward Euler	0.001
Error estimation	Exclude algebraic
Absolute tolerance global method	Scaled
Tolerance method	Factor
Tolerance factor	0.05
Update scaled absolute tolerance	True
Solver	MUMPS
Memory allocation factor	1.2
Preordering algorithm	Automatic
Row preordering	True
Reuse preordering	True
Use pivoting	On
Pivot threshold	0.1
Out-of-core	Automatic
Memory fraction for out-of-core	0.99
In-core memory method	Automatic
Minimum in-core memory	512 MB
Used fraction of total memory	0.8
Internal memory usage factor	3
Check error estimate	Automatic
Factor in error estimate	400
Iterative refinement	True
Maximum number of refinements	15
Matrix symmetry	Automatic
Matrix format	Automatic
Row equilibration	True
Null-space function	Automatic
Orthonormal block limit	10000000
Store last residual	Off
Solver log	Normal
Log sampling (wall-clock)	0.005 s
Assembly block size	1000
Stop when undefined mathematical operation is detected	True
Nonlinear method	Constant (Newton)
Damping factor	1
Limit on nonlinear convergence rate	0.9
Jacobian update	On every iteration
Termination technique	Iterations or tolerance
Number of iterations	1
Tolerance factor	0.1

Table S5: Parameters of Green's function after fitting

Parameter	Value (fast)	Value (slow)	Unit
A	0.9843	5.7737	μM
v	731	0.9	cell/s
τ_{inc}	0.008	9.3	s
τ_{dec}	1.01	3.9	s
ρ_c	55	5.2	μM
c_w	1	4.9	1

Bibliography

[1] Paul M Diderichsen and Sven O Göpel. Modelling the electrical activity of pancreatic α-cells based on experimental data from intact mouse islets. *Journal of biological physics*, 32(3-4):209–229, 2006.

[2] Shaojie Han, John E Speich, Thomas J Eddinger, Krystina M Berg, Amy S Miner, Chris Call, and Paul H Ratz. Evidence for absence of latch-bridge formation in muscular saphenous arteries. *American Journal of Physiology-Heart and Circulatory Physiology*, 291(1):H138–H146, 2006.

[3] Thomas Höfer, Laurent Venance, and Christian Giaume. Control and plasticity of intercellular calcium waves in astrocytes: a modeling approach. *Journal of Neuroscience*, 22(12):4850–4859, 2002.

[4] Chitaranjan Mahapatra, Keith L Brain, and Rohit Manchanda. A biophysically constrained computational model of the action potential of mouse urinary bladder smooth muscle. *PloS one*, 13(7), 2018.

[5] Constantine N Tzouanas, Soonyoung Kim, Krishna N Badhiwala, Benjamin W Avants, and Jacob T Robinson. Hydra vulgaris shows stable responses to thermal stimulation despite large changes in the number of neurons. *Iscience*, 24(6):102490, 2021.

[6] Maxime Yochum, Jérémy Laforêt, and Catherine Marque. An electro-mechanical multiscale model of uterine pregnancy contraction. *Computers in biology and medicine*, 77:182–194, 2016.

Chapter 3

MODELING THE OSMOTICALLY DRIVEN BURSTING DYNAMICS OF HYDRA CB NEURON

This chapter describes a neuronal model that successfully simulates the spontaneous bursting dynamics of CB neuron in *Hydra*. The research presented in this chapter is the result of a collaboration with Dr. Joshua Swore, Dr. Martha Bosma and Dr. Adrienne Fairhall. Joshua Swore and Martha Bosma implemented calcium imaging experiments and provided recording data. Adrienne Fairhall and I designed the research. I performed the data analysis, designed and built the model, interpreted the results and wrote the manuscript. A paper from this research is in preparation and ready to submit.

3.1 Abstract

The interaction of neuronal activity, behavior and environment allows biological systems to maintain dynamical stability. However, the fundamental mechanisms underlying these interactions are not always well understood due to their complexity. As an example of active stabilization, the small freshwater cnidarian *Hydra* undergoes regular contractions that have been long proposed to be related to osmoregulation, a critical process for a freshwater animal. However, the biophysical mechanisms that support these dynamics remain unknown. Electrophysiological experiments and recent calcium imaging techniques reveal a network of neurons with a specific neural activity pattern, the contraction burst, whose periodic bursting dynamics drives these body contractions. Here, we aim to model these neural dynamics. We hypothesize that neurons are driven by mechanosensation of stress induced by water absorption. With this assumption, we successfully simulate *Hydra*'s bursting dynamics and its detailed features; in particular, the parabolic pattern of interspike intervals measured experimentally are well predicted by our model. We further build a random network model composed of single neuronal models, simulate the synchronization of the network through gap junctions, and test its responses to mechanical or electrical responses. Our model re-

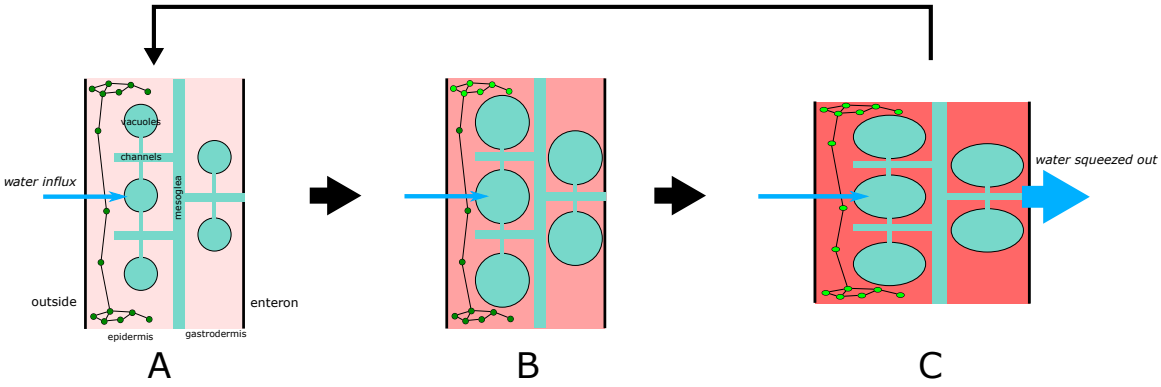

Figure 3.1: Conceptual scheme of the biological process described by the model, where colors in the muscle region represent the intensity of muscle stress. (A) Cross-section of *Hydra* body: water is constantly absorbed from outside into cell tissues and vacuoles due to the osmotic gradient; (B) when the resulting muscle stress increases over a threshold, it triggers the firing of neurons through mechanosensitive channels; (C) neural excitation stimulates muscle contraction of the whole body, which briefly further increases muscle stress and also extrudes water, reducing pressure and restoring the state to A.

veals how neuron, behavior and environment can couple to maintain a stable equilibrium, and can serve as a basis for understanding more complex behavior in *Hydra*, as well as forming a template for future work to explore similar mechanisms in more complex biological systems.

3.2 Introduction

Periodic bursting is a dynamics wherein a brief period of rapid spiking and a period of quiescence repeatedly interplay [26], playing important roles in neural coding [32], synchronization [74] and motor pattern generation [41, 40]. Observed in early electrophysiological studies [50, 51, 52, 53, 27, 28, 69, 70, 68, 71] as well as recent calcium imaging studies [19, 67, 4], a subnetwork of neurons in the small cnidarian *Hydra* exhibit a spontaneous bursting pattern. They are called the "contraction burst", or CB, network because their spiking activities always accompany, and are believed to generate, the contraction burst behavior of *Hydra* [76]. Previous work has established that the bursting dynamics of *Hydra* CB neurons are affected by mechanical, electrical, light and thermal stimuli [50, 52, 60, 71, 4, 75], and inhibited by another subnetwork of neurons (RP) in *Hydra* [42, 69, 68, 71, 19]. However, the fundamental mechanism underlying the ongoing bursting dynamics of *Hydra* CB

neurons in unknown, and a model that can provide an explanation for these dynamics would be helpful in understanding the evolution and function of bursting dynamics.

Functionally, a key characteristic of *Hydra*'s CB dynamics is its high correlation with the osmolarity of the surrounding fluid. *Hydra*'s enteron is observed to maintain a hyper-osmolarity in respect to the body tissues, and its body faces a constant water influx due to the osmotic gradient and the high permeability of the cell membranes to both salts and water [8]. To maintain a stable internal environment, *Hydra* extrudes excess water through periodic body contractions [38], of which the frequency is inversely proportional to the external osmolarity [9]. Such osmoregulation is found to play a deterministic role in *Hydra*'s tissue regeneration [24, 33, 64, 43, 78, 79, 22]. Under both light and electron microscopy, numerous intercellular vacuoles are observed in the ectoderm and the endoderm of *Hydra* body tissues, which are connected with the mesoglea and the enteron through narrow intercellular channels, and decrease markedly in size when *Hydra* is in a high osmolal solution [7]. Periodic body column contractions can "wring" the *Hydra* body by compressing the cell tissues and intercellular vacuoles to squeeze the water towards the enteron [7]. Recent calcium imaging experiments further verified the inversely proportional relationship between CB neural activity and external osmolarity, and proposed a possibility that osmolarity alters the contractions through a mechanosensory system that senses tissue pressure [80]. Mechanosensory responses were identified in nematocytes of *Hydra* [31, 73]. Examination of gene expression of mechanosensitive channels in *Hydra*'s genome database [63] reveals a wide distribution of PIEZO2 [17, 49, 21, 44, 81] in most neuron types, providing support for the hypothesis of mechanosensation as a driving force.

A notable characteristic of *Hydra* CB dynamics is that the firing frequency increases then decreases throughout each bursting event. This is known as "parabolic bursting" [20, 58, 65] or "circle/circle" bursting [26]. Parabolic bursting is a prominent feature of *Aplysia* R_{15} neurons [55, 35], which were extensively studied in a series of modeling papers from the 70s to the mid-90s [56, 54, 2, 3, 15, 16, 13, 14, 10, 11, 12]. These models can be reduced to a canonical model with a pair of variables (u_1, u_2), where u_1 is a positive feedback variable that describes activation of slow amplifying currents, and u_2 is a negative feedback variable that describes activation of slow resonant currents [26]. The competition between u_1 and

u_2 generates a slow wave oscillation that drives the neuron to spike as a parabolic bursting pattern. Thus, exploring the mechanisms underlying *Hydra* CB dynamics can be reduced to the problem of identifying the biophysical substances of the two slow competing variables in *Hydra*.

Given these findings, we build a simple model of *Hydra* CB neurons that successfully simulates their dynamics. Our model is based on the leaky integrate-and-fire (LIF) model [1], modified by the inclusion of mechanosensitive channels, of which the open probability is determined by the stress in the membrane of the neuron dendrites [66, 57]. Under this model, we propose that the two slow competing variables in Izhikevich's canonical model for parabolic bursting are given by the stress changes caused by rapid muscle contraction and slow water influx. This formulation of the relationship between stress and neuronal firing is very concise and closely matches the light and electron microscopy observations. Further, we build a gap junctionally coupled neural network model which simulates synchronization across the CB subnetwork and its responses under external mechanical and electrical stimuli. Our model successfully captures the neuronal parabolic bursting pattern and the inverse proportional relationship between CB activity and the external osmolarity, establishing a mechanistic basis for the osmoregulation function of CB dynamics and paving a route to better understand how neuron, behavior and environment can mutually interact to maintain dynamic stability.

3.3 Results

3.3.1 Proposed biological process

Based on previous experimental observations and the hypothesis of osmoregulatory drive via mechanosensation, the conceptual scheme of the biological process described by our model (Fig. 3.1) is as follows:

1. A constant diffusional water influx occurs because of the osmotic gradient between the cell tissues and the environment, which contributes to a linear increase of the stress in muscle and in the membrane of neuronal dendrites.

2. With the increase of stress, the opening probability of mechanosensitive channels increases, causing an increasing depolarizing current. When the current exceeds a threshold, the neuron fires. The excitation propagates over the neural network, and triggers the contraction of muscle cells in the whole *Hydra* body [77].

3. The body contractions result in two effects: on one hand, they compress the muscle cells, causing a transient increase of the stress in muscle and neurons, facilitating the neurons to fire; on the other hand, they squeeze the cell tissues and vacuoles, extruding the excess water to the enteron, decreasing the stress and terminating the neuronal firing.

4. When the excess water in cell tissues is fully extruded, the stress is reduced to the original level, thus the neuronal firing and body contractions cease. The initial state is restored, and the process repeats.

5. Periodical mouth opening behavior is recorded [67], which eventually expels the fluid from the body to the outside through the opened hypostome. Since its period is too long (several hours) compared to that of the contraction bursts (tens to hundreds of seconds), we don't include it into our model.

3.3.2 Muscle stress regulates neuronal activity through mechanosensitive channels

We model *Hydra* CB neuron with a modified LIF model described by Eq. 3.1:

$$\frac{\mathrm{d}V}{\mathrm{d}t} = -\frac{1}{C_m}\left(I_s + g_L(V - E_L)\right) \tag{3.1a}$$

$$I_s = g_s \cdot P_o \cdot (V - E_s) \tag{3.1b}$$

$$P_o = \frac{1}{\left(1 + k_b \exp\left[-s\left(\frac{\sigma_m}{m}\right)^q\right]\right)} \tag{3.1c}$$

where V is the membrane potential, C_m is the cell capacitance, g_L and E_L separately represent the conductance and reversal potential of the leak channel, and I_s is the current

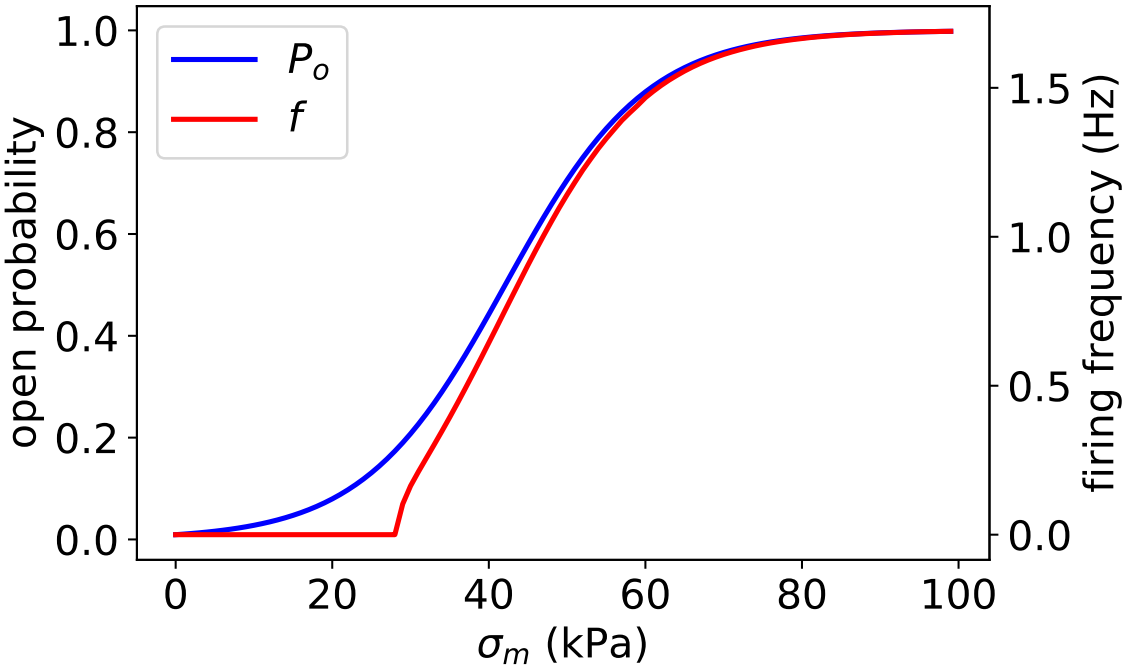

Figure 3.2: Stress dependence of open probability (P_o) and firing frequency (f).

through mechanosensitive channels, of which the conductance and reversal potential are represented as g_s and E_s respectively. The relation between the open probability (P_o) and the muscle stress (σ_m) is represented by a Boltzmann relation, in which all parameters follow Swerup-Rydqvist model [66].

Fig. 3.2 shows how P_o and the firing frequency f depend on the muscle stress, demonstrating that our model is that of a type I neuron, with a firing threshold of σ_m at around 30 kPa, and where both P_o and f increase with stress σ_m.

3.3.3 Muscle stress is regulated by post-spike body contractions and water influx

We decompose the muscle stress into two parts based on their sources: each body contraction directly contributes a sudden increase to the muscle stress, which we call "active stress" (σ_a); cells swell under the constant water influx, contributing a continuous increase to the muscle stress, which we call "water stress" (σ_w). The total muscle stress is then taken to be simply the sum of these two parts: $\sigma_m = \sigma_a + \sigma_w$.

Active stress

The active stress is formulated as Eq. 3.2

$$\frac{\mathrm{d}\sigma_a}{\mathrm{d}t} = -\frac{\sigma_a}{\tau_a} + k_a \sum_{t^{(f)}} \delta(t - t^{(f)}) \tag{3.2}$$

where σ_a decays exponentially with a time constant τ_a when there is no body contraction, and each contraction contributes a sudden increment k_a. For simplicity, we consider the increase of σ_a to occur immediately after the neural firing time $t^{(f)}$, representing it with a delta function.

Water stress

We formulate the water stress as follows:

$$\frac{\mathrm{d}\sigma_w}{\mathrm{d}t} = k_{\mathrm{in}} - k_e \sum_{t^{(f)}} \delta(t - t^{(f)}) \tag{3.3}$$

where σ_w increases linearly with a rate k_{in} due to the constant water influx, and each contraction contributes a sudden decrement k_e by squeezing the cell tissues and extruding the excess water. We use a delta function to represent the decrement, approximating the water extrusion process to occur immediately after the firing time $t^{(f)}$ for simplicity.

3.3.4 Interactions of neuron, muscle and environment generate a parabolic bursting pattern

The resulting model dynamics are shown in Fig. 3.3, where Fig. 3.3A shows a periodic pattern of membrane potential, exhibiting a parabolic bursting pattern; Fig. 3.3B shows the how muscle stresses σ_a and σ_w evolve periodically with time , and Fig. 3.3C shows their repetitive trajectory on a 2D plane, showing the interplay of spiking and resting phases.

To better visualize the parabolic feature of the bursting dynamics, and to calibrate our simulation using experimental recordings, we plot the inter-spike intervals (ISI) in one burst from our model, and overlay them with data from 114 bursts extracted from 9 calcium imaging videos taken from different animals (Fig. 3.4). We note that the pulse numbers and intervals over different bursts are quite diverse, indicating that the bursting pattern of

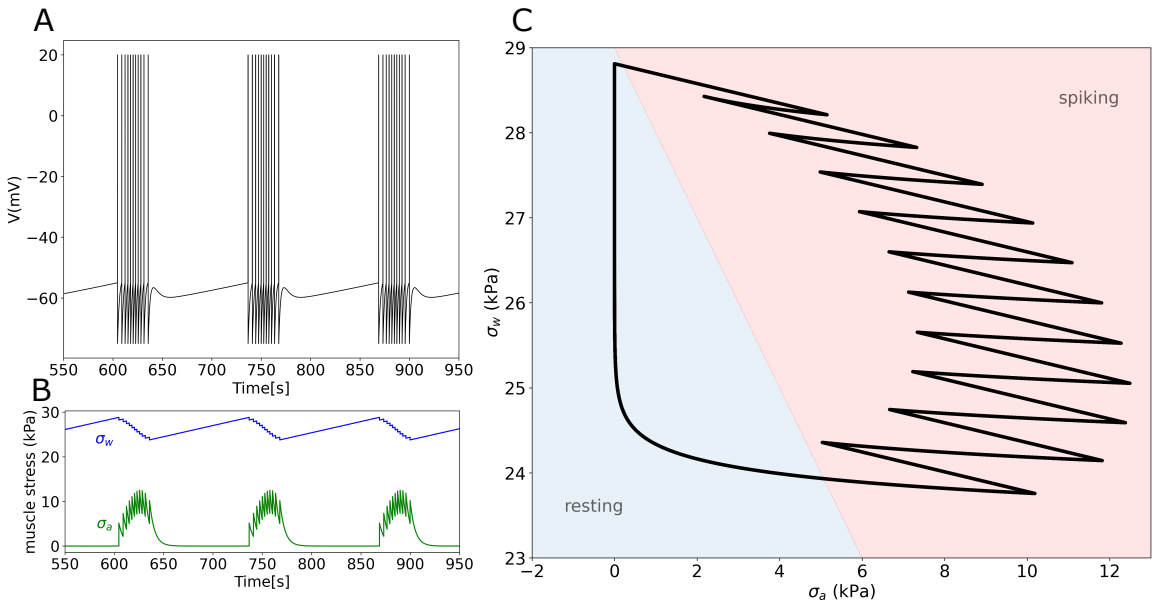

Figure 3.3: Simulation results of the model. (A) the trace of membrane potential; (B) traces of active and water stress; (C) the trajectory depicted as a curve on the (σ_a, σ_w) plane.

Hydra CB is irregular. Our model captures the typical feature of the bursting dynamics, and generates a good fit to the mean experimental data.

3.3.5 Measures of neural activity are inversely proportional to the osmolarity

We explored whether our model can predict the inverse relationship between CB firing and media osmolarity found in previous work [9, 80] by tuning the parameter k_{in} which controls the water influx rate (Fig. 3.5). We invert the x-axis since the influx rate k_{in} is inversely proportional to the media osmolarity which we are interested in. We use four metrics to quantify the neural activity: frequency of bursts (number of bursts over one second), pulse number per cycle, duration of a burst, and frequency of pulses in a burst (pulse number / burst duration). As shown in the figure, all four metrics have an inverse relationship with the osmolarity, which is consistent with the findings in [80] and [9]. Our simulation results show that purely varying the influx rate k_{in} will not change the parabolic bursting feature of the neuron, meaning that the *Hydra* CB should always exhibit parabolic bursting dynamics regardless of experimental variations in the media osmolarity. Furthermore, our simulation

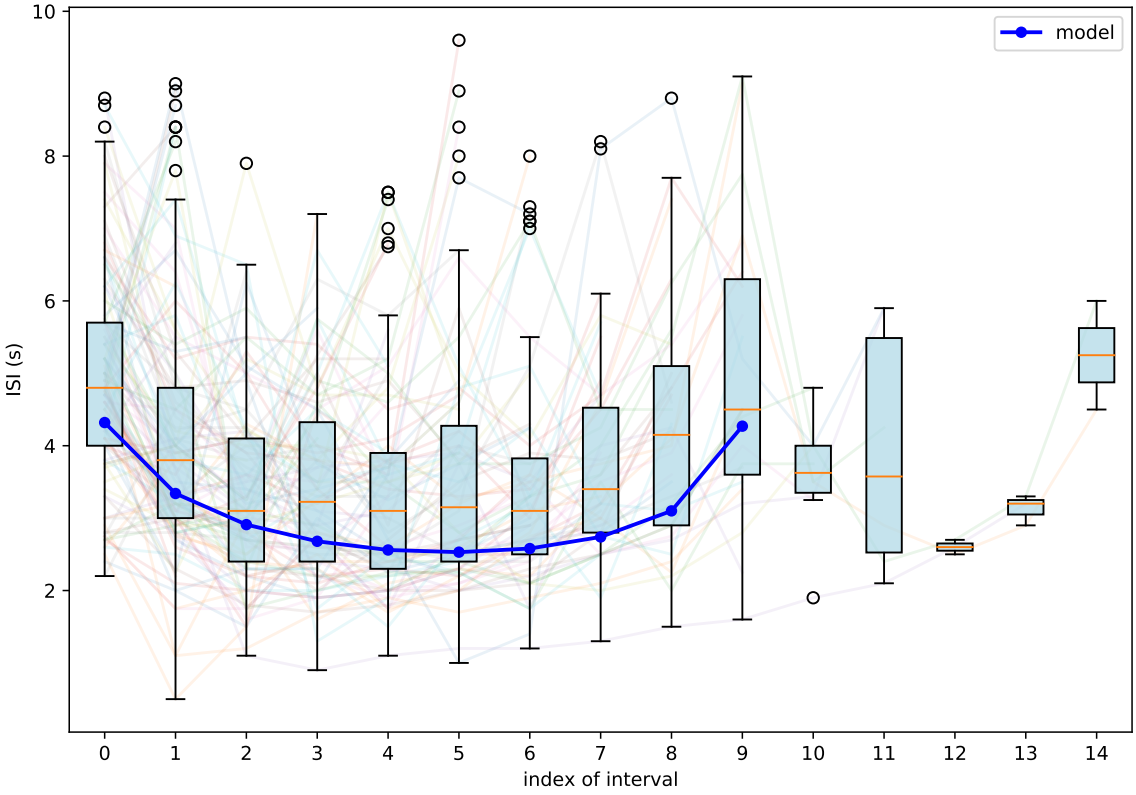

Figure 3.4: Inter-spike intervals (ISI) from our model (blue line) and calcium imaging videos (dim lines). Boxplots show the means and standard deviations of experimental ISI.

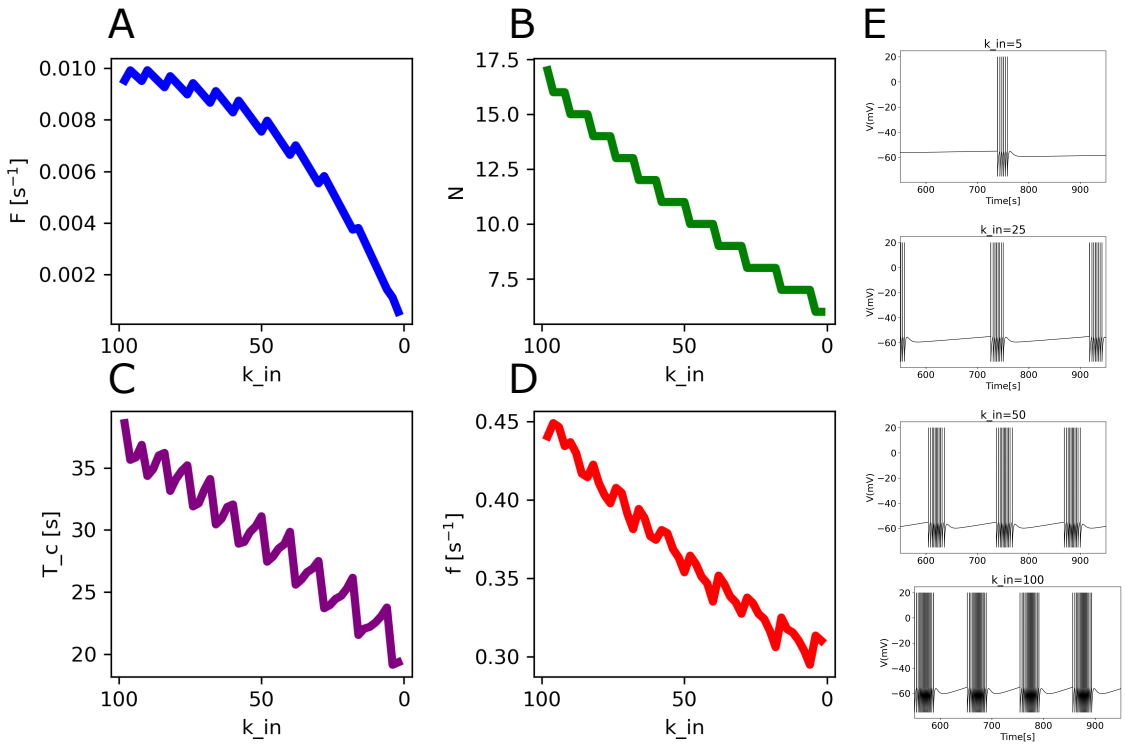

Figure 3.5: Relation between the neural activity and k_{in}. (A - D) Plots of how frequency of bursts (A), pulse number per cycle (B), duration of a burst (C) and frequency of pulses in a burst (D) vary with k_{in}. (E) Example firing patterns of $k_{\text{in}} = 5, 25, 50$ and 100.

results show some additional fine-scale features: with the increase of osmolarity, the number of pulses per cycle (Fig. 3.5B) decrease step-wise, and all other metrics (Fig. 3.5A, C, D) have a local increase when pulses number stays the same, and a drastic decrease when the pulse number decreases. Previous experiments only measure responses at a few osmolarity values over a large range so do not report on such local details. We predict such features may be observed in an experiment that records over many values of osmolarity, given sufficient data to average over the irregularity/noise.

3.3.6 Competition between k_a and k_e generates different dynamics

By tuning k_a and k_e, we found the competition between them also plays an important role in determining the firing patterns (Fig. 3.6). In contrast to k_{in}, varying k_a and k_e not

only affects features including frequency, duration and pulse number, but also determines whether the neuron exhibits a bursting pattern or not. Figs. 3.6A-D show that under some combinations of k_a and k_e (uncolored region), the neuron fires in an continuous spiking pattern instead of bursting (colored region). Since k_a and k_e reflecting physical properties, such as stiffness of the muscle and contractile intensity of the myonemes which are genetically determined, such a prediction is not easy to test experimentally. Potentially, experiments that can modify muscle properties may provide the possibility to expose a regime of non-bursting CB dynamics. Furthermore, based on the phase diagrams in Fig. 3.6, a combination with larger k_a and smaller k_e produces a larger number of pulses per burst, longer burst duration and higher pulse frequency, with, however, a smaller burst frequency. Similar with k_{in}, a step-wise trend of pulse number can also be observed along the direction from top-left to bottom-right (Fig. 3.6B), corresponding to the zigzag structure in Fig. 3.6A, C, D.

3.3.7 Gap junctions can synchronize the bursting of neurons

Given the prevalence of innexins in neuronal RNAseq data [63] and previous structural evidence [25, 72, 23], gap junctions are believed to be widely distributed among neurons in *Hydra*, and are assumed to play an important role in neural synchronization [36, 6]. We therefore built a model of the CB network in which each neuron is modeled by the modified LIF model introduced above, and neurons are gap junctionally coupled, such that input from other neurons to neuron i is given by as $I_c^i = g_c \sum_{j \in J}(V_j - V_i)$ where g_c is the bidirectional coupling coefficient and J is the set of all neighbors of neuron i. For simplicity, we build a random network of 50 neurons with a connection probability $P_c = 0.3$ between any pair of neurons. We initiate the network state by setting a random σ_w which is uniformly distributed between 2 kPa and 3 kPa for each neuron, holding all other parameters the same. Fig. 3.7 shows the comparison of spike trains between $g_c = 0$ and $g_c = 200$ (nS), from which we can see that gap junctional coupling is capable of synchronizing the out-of-phase neurons to fire as a cluster, thus allowing for the observed synchronization phenomena observed in reaggregation of dissociated *Hydra* [37].

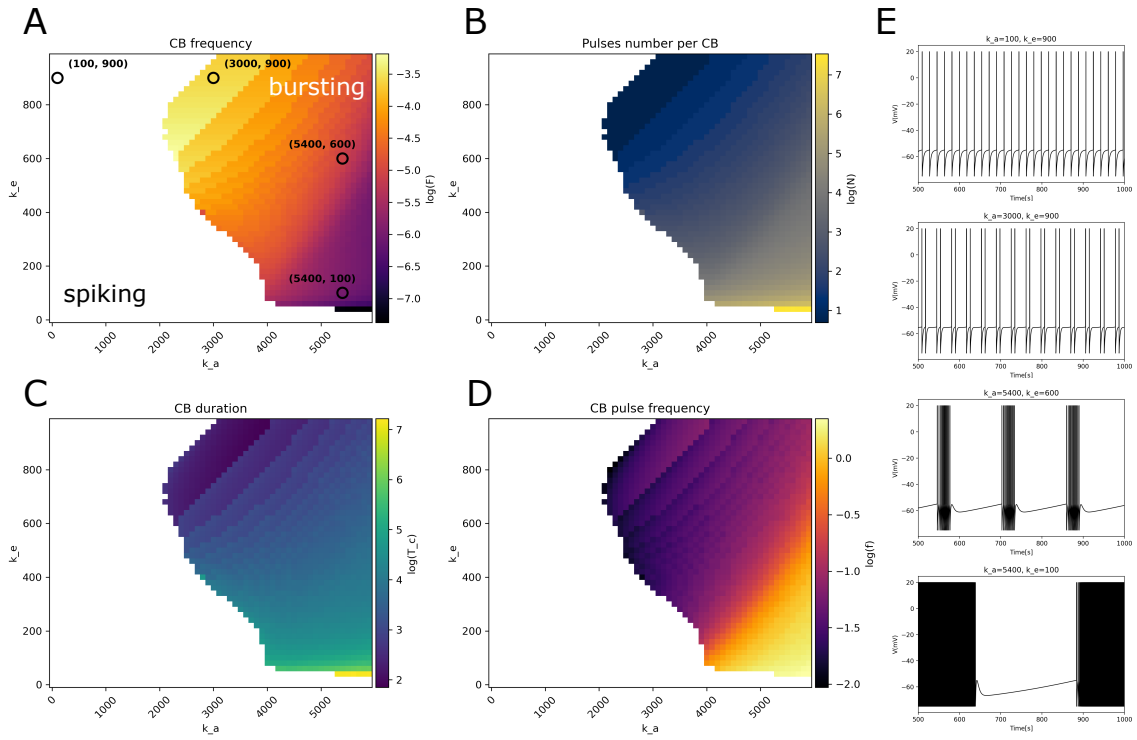

Figure 3.6: Effects of k_a and k_e on the firing pattern. (A - D) Log-scale phase diagrams of frequency of bursts (A), pulses number per cycle (B), duration of a burst (C) and frequency of pulses in a burst (D), where the neuron is showing a bursting pattern in colored region and a spiking pattern in uncolored region. (E) Example firing patterns corresponding to the markers in plot A.

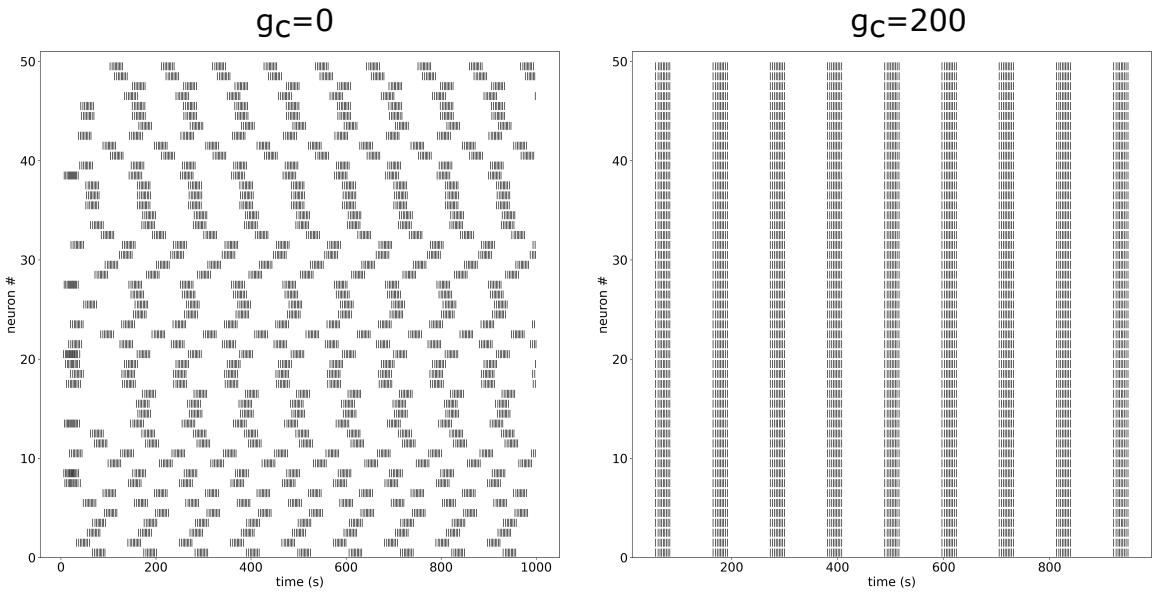

Figure 3.7: Spike trains of neurons in random networks with $g_c = 0$ and 200 nS, where x-axis represents time and each row along the y-axis represents the spike train of each neuron.

3.3.8 External electrical or mechanical stimulation triggers early single pulse responses and delay the upcoming bursts

Previous experiments have shown that external electrical stimuli can cause single contractions which supplant the regular bursts [52], and mechanical stimuli can also cause immediate neural responses which are three times more likely to be single pulses than the bursts typical in spontaneous activity [5]. We test whether our neural network model is consistent with these observations by modeling external stimulation. We apply an external input current ($I_{\text{ex}} = 10$ nA for 1 s) on 1 neuron in the network to simulate electrical stimulation, and apply an external stress on the muscle stress σ_m (200 kPa (29 psi) for 1 s) on 5 neurons to simulate the mechanical stimulation. We find that both stimulation protocols trigger neurons to give only single-pulse responses, and the upcoming bursts after that are delayed, Fig. 3.8, matching the experimental observations.

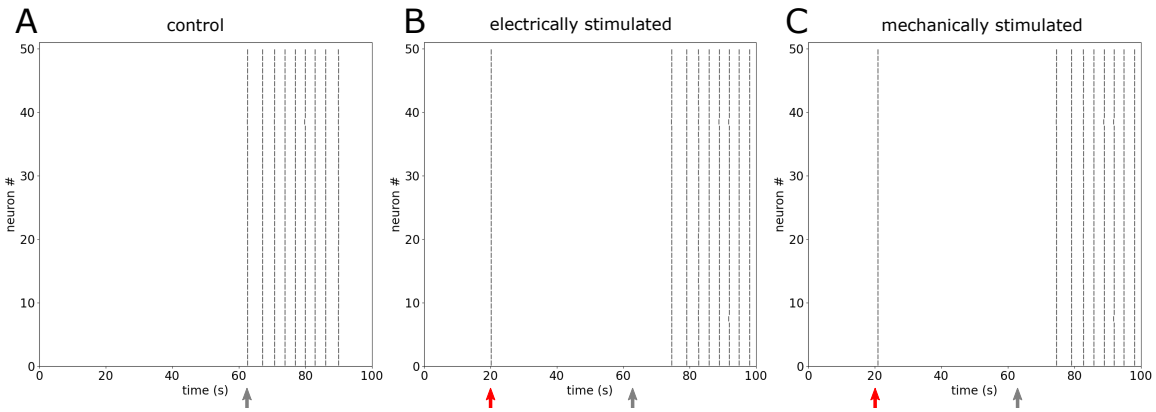

Figure 3.8: Spike trains of neural responses to external stimulation, where red arrows indicate times of stimulation and gray arrows the start time of the first burst of spontaneous activity without stimulation. (A) Spontaneous activity; (B) electrically stimulated; (C) mechanically stimulated.

3.4 Discussion

In this work, we built a model in which we concisely formulated expressions capturing proposed biological mechanisms, and successfully simulated the firing patterns of *Hydra* CB neurons. Supported by RNAseq query results [63], we hypothesized that mechanosensitive PIEZO channels are distributed on the neuronal membranes, which can sense the stress in the muscle and contribute to neuronal firing. Our model incorporated both the constant increase of the muscle stress with fluid absorption and the sudden effects of muscle contractions after neural firing. We simulated the interplay of active stress and passive stress, and showed that the interplay of these two timescales reproduce the parabolic bursting pattern that is consistent with experimental recordings. The intervals of our model fit experimental data well. Furthermore, the model predicts some detailed features of the firing patterns as osmolarity is varied and as a function of muscle parameters, which await testing by future experiments.

We then incorporated our single neuron model into a random network model to simulate the synchronization of neurons and their responses to different types of external stimulation. Our network model demonstrates that gap junctions can effectively synchronize neurons with different initial phases, and supported our proposed mechanism by reproducing experimental responses to both electrical and mechanical stimuli.

Rather than attempting to explain the dynamics with endogenous pacemaker activity intrinsic to a neuron, we considered the neuron as an open system and modeled the interactions among neuron, behavior and environment, exploring the functions that the neural activity plays in maintaining system homeostasis. This function exhibits a similarity with the autonomic nervous system (ANS) in advanced animals. Though considerable previous modeling work has focused on the ANS, especially the baroreflex control system [29, 18, 46, 39, 45, 48, 47, 34, 61, 62, 59], these are all generally limited to a phenomenological level due to the complexity of the system. However, the simplicity of *Hydra*, which is believed to be the ancestor of the vertebrate ANS [30], provides us the opportunity to construct biophysical models that can capture mechanisms of interaction and stability.

Despite the success, our model is clearly highly simplified and neglects some potential complexities that may be significant. For example, both body contraction and the water extrusion process are assumed to be transient events in our model; however, the processes can be very complex due to the viscosity of the muscle and water-structure interactions. Also, we assume that each contraction has the same effect on internal stress, but they may vary considerably because of the change in body shape and conformation during the contraction burst. Similarly, our modeling of the network was highly simplified and aimed only at capturing properties of synchronization and the interrelationship between bursting and coupling. We did not include properties such as distance-dependent connectivity and the potential role of inhibition from the rhythmic potential network, which is an important consideration for future work.

3.5 Materials and Methods

Our model is built with Python 3. Differential equations are solved using Euler stepping method with a 10 ms time step. All codes are available at github.com/hengjiwang/hydranerv.

Parameters used in our model are described in Tab. 3.1, where those related to the mechanosensitive channel (k_b, s, q, m, E_s) are borrowed from [66]. k_{in}, k_a and k_e are tuned to fit the firing frequency and intervals of the model to experimental data.

Parameter	Value	Unit
C_m	50	nF
g_L	15	nS
E_L	-75	mV
g_s	25	nS
k_b	106	1
s	0.00277	Pa^{-1}
q	1	1
m	25	1
E_s	10	mV
τ_a	5	s
k_a	5150	Pa
k_{in}	50	Pa/s
k_e	600	Pa

Table 3.1: Parameters used in the model.

3.6 Acknowledgements

This work was funded by the National Science Foundation Grant CRCNS 1822550 and a Simons Collaboration for the Global Brain grant to A.L.F.. We thank Rafael Yuste, John Syzmanski, Wataru Yamamoto, Rob Steele and Jacob Robinson for critical discussions.

Bibliography

[1] Larry F Abbott. Lapicque's introduction of the integrate-and-fire model neuron (1907). *Brain research bulletin*, 50(5-6):303–304, 1999.

[2] WB Adams. Slow depolarizing and hyperpolarizing currents which mediate bursting in aplysia neurone r15. *The Journal of physiology*, 360(1):51–68, 1985.

[3] William B Adams and Jack A Benson. The generation and modulation of endogenous rhythmicity in the aplysia bursting pacemaker neurone r15. *Progress in biophysics and molecular biology*, 46(1):1–49, 1985.

[4] Krishna N Badhiwala, Daniel L Gonzales, Daniel G Vercosa, Benjamin W Avants,

and Jacob T Robinson. Microfluidics for electrophysiology, imaging, and behavioral analysis of hydra. *Lab on a Chip*, 18(17):2523–2539, 2018.

[5] Krishna N Badhiwala, Abby S Primack, Celina Juliano, and Jacob T Robinson. Multiple neuronal networks coordinate hydra mechanosensory behavior. *bioRxiv*, pages 2020–10, 2021.

[6] Michael VL Bennett and R Suzanne Zukin. Electrical coupling and neuronal synchronization in the mammalian brain. *Neuron*, 41(4):495–511, 2004.

[7] Dale J Benos, R Gary Kirk, William P Barba, and Marcia M Goldner. Hyposmotic fluid formation in hydra. *Tissue and Cell*, 9(1):11–22, 1977.

[8] Dale J Benos and Robert D Prusch. Osmoregulation in fresh-waterhydra. *Comparative Biochemistry and Physiology Part A: Physiology*, 43(1):165–171, 1972.

[9] Dale J Benos and Robert D Prusch. Osmoregulation in hydra: Column contraction as a function of external osmolality. *Comparative Biochemistry and Physiology Part A: Physiology*, 44(4):1397–1400, 1973.

[10] Richard Bertram. A computational study of the effects of serotonin on a molluscan burster neuron. *Biological Cybernetics*, 69(3):257–267, 1993.

[11] Richard Bertram. Reduced-system analysis of the effects of serotonin on a molluscan burster neuron. *Biological cybernetics*, 70(4):359–368, 1994.

[12] Robert J Butera, John W Clark, Carmen C Canavier, Douglas A Baxter, and John H Byrne. Analysis of the effects of modulatory agents on a modeled bursting neuron: Dynamic interactions between voltage and calcium dependent systems. *Journal of computational neuroscience*, 2(1):19–44, 1995.

[13] CC Canavier, DA Baxter, JW Clark, and JH Byrne. Nonlinear dynamics in a model neuron provide a novel mechanism for transient synaptic inputs to produce long-term alterations of postsynaptic activity. *Journal of neurophysiology*, 69(6):2252–2257, 1993.

[14] CC Canavier, DA Baxter, JW Clark, and JH Byrne. Multiple modes of activity in a model neuron suggest a novel mechanism for the effects of neuromodulators. *Journal of neurophysiology*, 72(2):872–882, 1994.

[15] CC Canavier, JW Clark, and JH Byrne. Routes to chaos in a model of a bursting neuron. *Biophysical journal*, 57(6):1245–1251, 1990.

[16] CC Canavier, JW Clark, and JH Byrne. Simulation of the bursting activity of neuron r15 in aplysia: role of ionic currents, calcium balance, and modulatory transmitters. *Journal of Neurophysiology*, 66(6):2107–2124, 1991.

[17] Alexander T Chesler and Marcin Szczot. Piezo ion channels: portraits of a pressure sensor. *Elife*, 7:e34396, 2018.

[18] Richard W DeBoer, John M Karemaker, and Jan Strackee. Hemodynamic fluctuations and baroreflex sensitivity in humans: a beat-to-beat model. *American Journal of Physiology-Heart and Circulatory Physiology*, 253(3):H680–H689, 1987.

[19] Christophe Dupre and Rafael Yuste. Non-overlapping neural networks in hydra vulgaris. *Current Biology*, 27(8):1085–1097, 2017.

[20] G Bard Ermentrout and Nancy Kopell. Parabolic bursting in an excitable system coupled with a slow oscillation. *SIAM journal on applied mathematics*, 46(2):233–253, 1986.

[21] Xiang-Zhi Fang, Ting Zhou, Ji-Qian Xu, Ya-Xin Wang, Miao-Miao Sun, Ya-Jun He, Shang-Wen Pan, Wei Xiong, Zhe-Kang Peng, Xue-Hui Gao, et al. Structure, kinetic properties and biological function of mechanosensitive piezo channels. *Cell & bioscience*, 11(1):1–20, 2021.

[22] Jaroslav Ferenc, Panagiotis Papasaikas, Jacqueline Ferralli, Yukio Nakamura, Sebastien Smallwood, and Charisios D Tsiairis. Mechanical oscillations orchestrate axial patterning through wnt activation in hydra. *Science Advances*, 7(50):eabj6897, 2021.

[23] BK Filshie and NE Flower. Junctional structures in hydra. *Journal of Cell Science*, 23(1):151–172, 1977.

[24] C Fütterer, C Colombo, F Jülicher, and A Ott. Morphogenetic oscillations during symmetry breaking of regenerating hydra vulgaris cells. *EPL (Europhysics Letters)*, 64(1):137, 2003.

[25] Arthur R Hand and Stephen Gobel. The structural organization of the septate and gap junctions of hydra. *The Journal of cell biology*, 52(2):397–408, 1972.

[26] Eugene M Izhikevich. *Dynamical systems in neuroscience*. MIT press, 2007.

[27] Robert K Josephson. Conduction and contraction in the column of hydra. *Journal of Experimental Biology*, 47(1):179–190, 1967.

[28] Robert K Josephson and Martin Macklin. Electrical properties of the body wall of hydra. *The Journal of General Physiology*, 53(5):638–665, 1969.

[29] Franz Kappel and Robert O Peer. A mathematical model for fundamental regulation processes in the cardiovascular system. *Journal of mathematical biology*, 31(6):611–631, 1993.

[30] John M Karemaker. An introduction into autonomic nervous function. *Physiological measurement*, 38(5):R89, 2017.

[31] GSAA Kass-Simon and AA Scappaticci, Jr. The behavioral and developmental physiology of nematocysts. *Canadian Journal of Zoology*, 80(10):1772–1794, 2002.

[32] Adam Kepecs and John Lisman. Information encoding and computation with spikes and bursts. *Network: Computation in neural systems*, 14(1):103, 2003.

[33] Michael Kücken, Jordi Soriano, Pramod A Pullarkat, Albrecht Ott, and Ernesto M Nicola. An osmoregulatory basis for shape oscillations in regenerating hydra. *Biophysical journal*, 95(2):978–985, 2008.

[34] Virginie Le Rolle, Alfredo I Hernández, Pierre-Yves Richard, and Guy Carrault. An autonomic nervous system model applied to the analysis of orthostatic tests. *Modelling and Simulation in Engineering*, 2008, 2008.

[35] Edwin S Levitan and Irwin B Levitan. Serotonin acting via cyclic amp enhances both the hyperpolarizing and depolarizing phases of bursting pacemaker activity in the aplysia neuron r15. *Journal of Neuroscience*, 8(4):1152–1161, 1988.

[36] Elena Leznik and Rodolfo Llinas. Role of gap junctions in synchronized neuronal oscillations in the inferior olive. *Journal of neurophysiology*, 94(4):2447–2456, 2005.

[37] Jonathan R Lovas and Rafael Yuste. Ensemble synchronization in the reassembly of hydra's nervous system. *Current Biology*, 31(17):3784–3796, 2021.

[38] Martin Macklin, Thomas Roma, and Kevin Drake. Water excretion by hydra. *Science*, 179(4069):194–195, 1973.

[39] Adam Mahdi, Jacob Sturdy, Johnny T Ottesen, and Mette S Olufsen. Modeling the afferent dynamics of the baroreflex control system. *PLoS computational biology*, 9(12):e1003384, 2013.

[40] Eve Marder. Motor pattern generation. *Current opinion in neurobiology*, 10(6):691–698, 2000.

[41] Eve Marder and Ronald L Calabrese. Principles of rhythmic motor pattern generation. *Physiological reviews*, 76(3):687–717, 1996.

[42] CB McCullough. Pacemaker interaction in hydra. *American zoologist*, 5(3):499–504, 1965.

[43] Moritz Mercker, Alexandra Köthe, and Anna Marciniak-Czochra. Mechanochemical symmetry breaking in hydra aggregates. *Biophysical journal*, 108(9):2396–2407, 2015.

[44] Mirko Moroni, M Rocio Servin-Vences, Raluca Fleischer, Oscar Sánchez-Carranza, and Gary R Lewin. Voltage gating of mechanosensitive piezo channels. *Nature communications*, 9(1):1–15, 2018.

[45] David Ojeda, Virginie Le Rolle, Olivier Rossel, Nicole Karam, Albert Hagège, Jean-Luc Bonnet, Philippe Mabo, Guy Carrault, and Alfredo I Hernández. Analysis of a baroreflex model for the study of the chronotropic response to vagal nerve stimulation. In *2015 7th International IEEE/EMBS Conference on Neural Engineering (NER)*, pages 541–544. IEEE, 2015.

[46] Mette S Olufsen, Hien T Tran, Johnny T Ottesen, Lewis A Lipsitz, and Vera Novak. Modeling baroreflex regulation of heart rate during orthostatic stress. *American Journal of Physiology-Regulatory, Integrative and Comparative Physiology*, 291(5):R1355–R1368, 2006.

[47] Johnny T Ottesen and Mette S Olufsen. Functionality of the baroreceptor nerves in heart rate regulation. *Computer methods and programs in biomedicine*, 101(2):208–219, 2011.

[48] Johnny Tom Ottesen. Modelling the dynamical baroreflex-feedback control. *Mathematical and Computer Modelling*, 31(4-5):167–173, 2000.

[49] Thibaud Parpaite and Bertrand Coste. Piezo channels. *Current Biology*, 27(7):R250–R252, 2017.

[50] LM Passano and CB McCullough. The light response and the rhythmic potentials of hydra. *Proceedings of the National Academy of Sciences of the United States of America*, 48(8):1376, 1962.

[51] LM Passano and CB McCullough. Pacemaker hierarchies controlling the behaviour of hydras. *Nature*, 199(4899):1174–1175, 1963.

[52] LM Passano and CB McCullough. Co-ordinating systems and behaviour in hydra: I. pacemaker system of the periodic contractions. *Journal of Experimental Biology*, 41(3):643–664, 1964.

[53] LM Passano and CB McCullough. Co-ordinating systems and behaviour in hydra ii. the rhythmic potential system. *Journal of Experimental Biology*, 42(2):205–231, 1965.

[54] RE Plant and M Kim. Mathematical description of a bursting pacemaker neuron by a modification of the hodgkin-huxley equations. *Biophysical journal*, 16(3):227–244, 1976.

[55] Richard E Plant. Bifurcation and resonance in a model for bursting nerve cells. *Journal of mathematical biology*, 11(1):15–32, 1981.

[56] Richard E Plant and M Kim. On the mechanism underlying bursting in the aplysia abdominal ganglion r15 cell. *Mathematical Biosciences*, 26(3-4):357–375, 1975.

[57] Masha Prager-Khoutorsky. Mechanosensing in hypothalamic osmosensory neurons. In *Seminars in Cell & Developmental Biology*, volume 71, pages 13–21. Elsevier, 2017.

[58] John Rinzel and Young Seek Lee. Dissection of a model for neuronal parabolic bursting. *Journal of mathematical biology*, 25(6):653–675, 1987.

[59] William C Rose, IA Rybak, and James S Schwaber. Closed loop model of vagally-mediated baroreflex control of heart rate. In *Proceedings of 17th International Conference of the Engineering in Medicine and Biology Society*, volume 2, pages 1367–1368. IEEE, 1995.

[60] Norman B Rushforth, Allison L Burnett, and Richard Maynard. Behavior in hydra: contraction responses of hydra pirardi to mechanical and light stimuli. *Science*, 139(3556):760–761, 1963.

[61] S Sajitha, Balakrishnan Minimol, and MG Mini. A computational model of autonomic nervous system for heart rate variability. In *2019 Computing in Cardiology (CinC)*, pages Page–1. IEEE, 2019.

[62] Kartik Sharma and Tarun Kumar Bera. Modelling of autonomic regulation in cardiovascular system based on baroreflex mechanism and overwhelming controller. *Proceedings of the Institution of Mechanical Engineers, Part I: Journal of Systems and Control Engineering*, 231(4):299–311, 2017.

[63] Stefan Siebert, Jeffrey A Farrell, Jack F Cazet, Yashodara Abeykoon, Abby S Primack, Christine E Schnitzler, and Celina E Juliano. Stem cell differentiation trajectories in hydra resolved at single-cell resolution. *Science*, 365(6451):eaav9314, 2019.

[64] Jordi Soriano, Sten Rüdiger, Pramod Pullarkat, and Albrecht Ott. Mechanogenetic coupling of hydra symmetry breaking and driven turing instability model. *Biophysical Journal*, 96(4):1649–1660, 2009.

[65] C Soto-Trevino, N Kopell, and D Watson. Parabolic bursting revisited. *Journal of mathematical biology*, 35(1):114–128, 1996.

[66] C Swerup and B Rydqvist. A mathematical model of the crustacean stretch receptor neuron. biomechanics of the receptor muscle, mechanosensitive ion channels, and macrotransducer properties. *Journal of neurophysiology*, 76(4):2211–2220, 1996.

[67] John R Szymanski and Rafael Yuste. Mapping the whole-body muscle activity of hydra vulgaris. *Current Biology*, 29(11):1807–1817, 2019.

[68] Cloe Taddei-Ferretti and S Chillemi. Modulation of hydra attentuata rhythmic activity. *Biological cybernetics*, 56(4):225–235, 1987.

[69] Cloe Taddei-Ferretti, L Cordella, and S Chillemi. Analysis of hydra contraction behaviour. In *Coelenterate ecology and behavior*, pages 685–694. Springer, 1976.

[70] CLOE Taddei-Ferretti and LUIGI Cordella. Modulation of hydra attenuata rhythmic activity: phase response curve. *Journal of Experimental Biology*, 65(3):737–751, 1976.

[71] Cloe Taddei-Ferretti and Carlo Musio. The neural net of hydra and the modulation of its periodic activity. In *International Work-Conference on Artificial Neural Networks*, pages 123–137. Springer, 1999.

[72] Yasuharu Takaku, Jung Shan Hwang, Alexander Wolf, Angelika Böttger, Hiroshi Shimizu, Charles N David, and Takashi Gojobori. Innexin gap junctions in nerve cells coordinate spontaneous contractile behavior in hydra polyps. *Scientific reports*, 4:3573, 2014.

[73] Ulrich Thurm, Martin Brinkmann, Rainer Golz, Matthias Holtmann, Dominik Oliver, and Thiemo Sieger. Mechanoreception and synaptic transmission of hydrozoan nematocytes. *Hydrobiologia*, 530(1):97–105, 2004.

[74] Roger D Traub and RK Wong. Cellular mechanism of neuronal synchronization in epilepsy. *Science*, 216(4547):745–747, 1982.

[75] Constantine N Tzouanas, Soonyoung Kim, Krishna N Badhiwala, Benjamin W Avants, and Jacob T Robinson. Stable behavioral and neural responses to thermal stimulation despite large changes in the hydra vulgaris nervous system. *Hydra vulgaris*, 2020.

[76] George Wagner. Memoirs: on some movements and reactions of hydra. *Journal of Cell Science*, 2(192):585–622, 1905.

[77] Hengji Wang, Joshua Swore, Shashank Sharma, John Szymanski, Rafael Yuste, Thomas Daniel, Michael Regnier, Martha Bosma, and Adrienne L Fairhall. From neuron to muscle to movement: a complete biomechanical model of hydra contractile behaviors. *bioRxiv*, 2020.

[78] Rui Wang, Tapan Goel, Kate Khazoyan, Ziad Sabry, Heng J Quan, Patrick H Diamond, and Eva-Maria S Collins. Mouth function determines the shape oscillation pattern in regenerating hydra tissue spheres. *Biophysical journal*, 117(6):1145–1155, 2019.

[79] Rui Wang, Robert E Steele, and Eva-Maria S Collins. Wnt signaling determines body axis polarity in regenerating hydra tissue fragments. *Developmental Biology*, 467(1-2):88–94, 2020.

[80] Wataru Yamamoto and Rafael Yuste. Whole-body imaging of neural and muscle activity during behavior in hydra vulgaris: effect of osmolarity on contraction bursts. *Eneuro*, 7(4), 2020.

[81] Wei-Zheng Zeng, Kara L Marshall, Soohong Min, Ihab Daou, Mark W Chapleau, Francois M Abboud, Stephen D Liberles, and Ardem Patapoutian. Piezos mediate neuronal sensing of blood pressure and the baroreceptor reflex. *Science*, 362(6413):464–467, 2018.

Chapter 4

A MUTUAL INHIBITION NETWORK MODEL OF THE NEURAL CIRCUITS OF HYDRA

This chapter describes a neuronal network model for *Hydra* neural circuits, which is partially based on the single neuronal modeling work described in chapter 3. The experimental data in this chapter was collected by Dr. Joshua Swore and Dr. Martha Bosma. Dr. Adrienne Fairhall and I designed the research. I performed the data analysis, designed and built the model, and interpreted the results.

4.1 Introduction

How do neurons function together as a single network that exhibits a variety of macroscopic dynamics and stable reactions to the environments? This is a fundamental question in neuroscience, but the complexity of most nervous systems does not allow the construction of a bottom-to-top mechanistic model based on recordings of high resolution neural activity. *Hydra*, an organism with one of the first evolved nervous systems, provides us an opportunity to explore and understand the deep mechanisms governing the relationships between neural activity and behavior.

Past work has shown that *Hydra*'s neural network consists of non-overlapping subnetworks, in which the contraction burst (CB) and rhythmic potential (RP) networks exhibit the most distinguishable activity [15, 3]. CB exhibits spontaneous bursting dynamics without requiring external stimulus, which usually consists of 2 - 3 bursts of several spikes per 10 minutes and is always accompanied by contractile behavior of *Hydra* [15]. RP exhibits a regular repetitive pattern of individual spikes, of which the frequency varies from 1 to 12 or more per minute; no evidence shows a direct instantaneous correlation between RP activity and any movement [13, 14, 16].

The electrical pulses of CB have been found to originate from the sub-hypostomal region just proximal to the tentacle insertions, which has led some to believe that CB pacemakers

are located in or near the hypostome of *Hydra* [13, 7, 5]. The observation that removing tentacles does not block CB activity yet decapitation of the sub-hypostome halts bursts completely for a long time further supports this belief [14, 15]. Conversely, the spontaneous electrical signals of RP originate from the peduncle, and RP pacemakers are believed "by default" to be located in the lower body column, especially the peduncle region near the base. However, demonstrations that the location of their activity can be shifted under mechanical, photic, or electrical stimulus suggest that pacemaking is a potential property of every RP neuron, and the concrete location of pacemakers is a result of the architecture of connectivity [13, 14, 16]. The activities of CB and RP have been shown to be anticorrelated, promoting the belief that these two neuronal subnetworks mutually inhibit each other [11, 13, 14, 3]. Such inhibitory interaction is found to be stronger at the two ends than along the column [8, 18].

Alongside experiments on intact *Hydra*, several studies have made use of cutting or dissociating *Hydra* into different shapes to explore neural connectivity and the resulting perturbed firing patterns. Split-body preparations of *Hydra* indicate that the conducting path for the CB pulse is a longitudinally continuous pathway having discontinuous, randomly distributed horizontal transmission sites [7] (Figure 4.1). Bisection experiments that separate *Hydra* into two halves horizontally show that hypostomal half shows a faster CB activity yet slower RP activity than the peduncular half ([1], our unpublished data). Dissociation and reaggregation of *Hydra* cells including gCAMP-expressing neurons shows how the nervous system reassembles through hierarchical modularity to a distributed network [10].

Despite these numerous experimental studies of *Hydra*'s nervous system, a neural network model that is capable of describing the fundamental neural functionalities and computational principles of the identified subnetworks has not yet been constructed. Even though some early work has attempted to build such a model based on the hypothesis of mutual inhibition and post-inhibition rebound [18, 2], they are restricted to a simple conceptual level and the simulation results are not in correspondence with the experimental observations. Here we will introduce a neural network model composed of single neuronal model units as described in chapter 3, which is able to consistently reproduce experimental recordings.

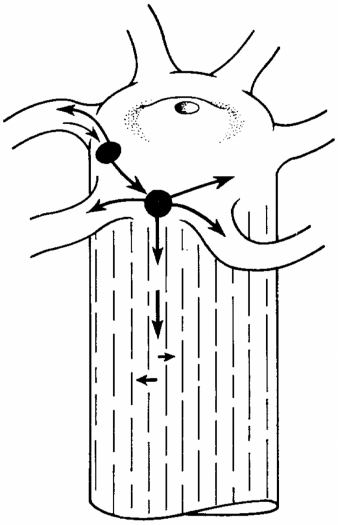

Figure 4.1: Conducting paths indicated by the split-body experiments [7].

Our work is an example of building a bottom-to-top neural network model for *Hydra* which we hope provides a basis to explore the joint evolution of nervous and mechanical systems in organisms to produce coordinated motion.

4.2 Results

4.2.1 A longitudinal-biased connectivity explains CB pulse conduction

In [7], *Hydra* polyps were prepared in multiple different split-body configurations to examine the conduction of electrical signals through the body column. These experiments revealed that CB pulses are initiated at the hypostome and conducted through a longitudinal-biased path down the body column. Based on some hypotheses, we build a neural network model consisting of single neuronal model units as described in chapter 3, and compare the simulation results with the experimental recordings in [7].

The layout of our network model for the CB net is shown in Figure 4.2. The transparent green cylindrical surface models the ectoderm of *Hydra*, on which each blue vertex represents a single CB neuron, with their indices denoted nearby. The vertices that are circled with red edges are pacemakers, which are assumed to possess mechanosensory channels that sense muscle stress (chapter 3), and others without edges are downstream neurons which

are passively driven. Black links that connect vertices represent gap junctions between neurons which synchronize their membrane potentials [19] as in chapter 3. The probability of connection between each pair of neurons decreases exponentially with their well-defined distance [12]. Based on experimental findings mentioned above, we hypothesize that the pacemakers of CB are located in the hypostome (top of the cylindrical model), neurons are connected in a longitudinal-biased pattern, and neurons at the two ends (top and bottom) are more densely distributed and connected than those at the middle of the body column. We initialize the pacemakers with different phases (water pressures), to guarantee that any observed synchronization is due to connectivity instead of coincidence.

Simulating this model produces neural spike trains as shown in Figure 4.3, which shows that pacemakers (indices < 20) can successfully synchronize with one other, and drive the whole network to burst synchronously.

We now simulate the operations of splitting the *Hydra* body by defining cut lines, denoted by thick gray curves in Figure 4.2, and removing all links that cross them. We tested two cases explored in [7] – cutting the network model into "H" (splitting *Hydra* into two halves connected with only one horizontal bridge) and "I" (splitting *Hydra* into two halves connected with only one longitudinal bridge) shapes, and compare the simulation results with the experimental recordings respectively. Our results show that a longitudinal bridge is more likely to conduct CB pulses than a horizontal one, Figure 4.5), supporting a longitudinal-biased connectivity in *Hydra*'s CB net, since otherwise the probability of gap junctions to cross the vertical bridge wouldn't be higher than crossing the horizontal bridge.

4.2.2 A mutual inhibition network can simulate the interplay of CB and RP activity

We next build a neural network including both CB and RP neurons. To model RP, we need to postulate a mechanism that drives its rhythmic firing pattern. It has been observed that extremely long-lasting elongation of the body can occur in the absence of CB, and that this is always accompanied by an increase of RP frequency [16, 17]. Further, no intracellular molecular mechanisms have been reported which can plausibly provide the drive for such a slow rhythm. Thus, we feel that it is reasonable to assume that the driving mechanism

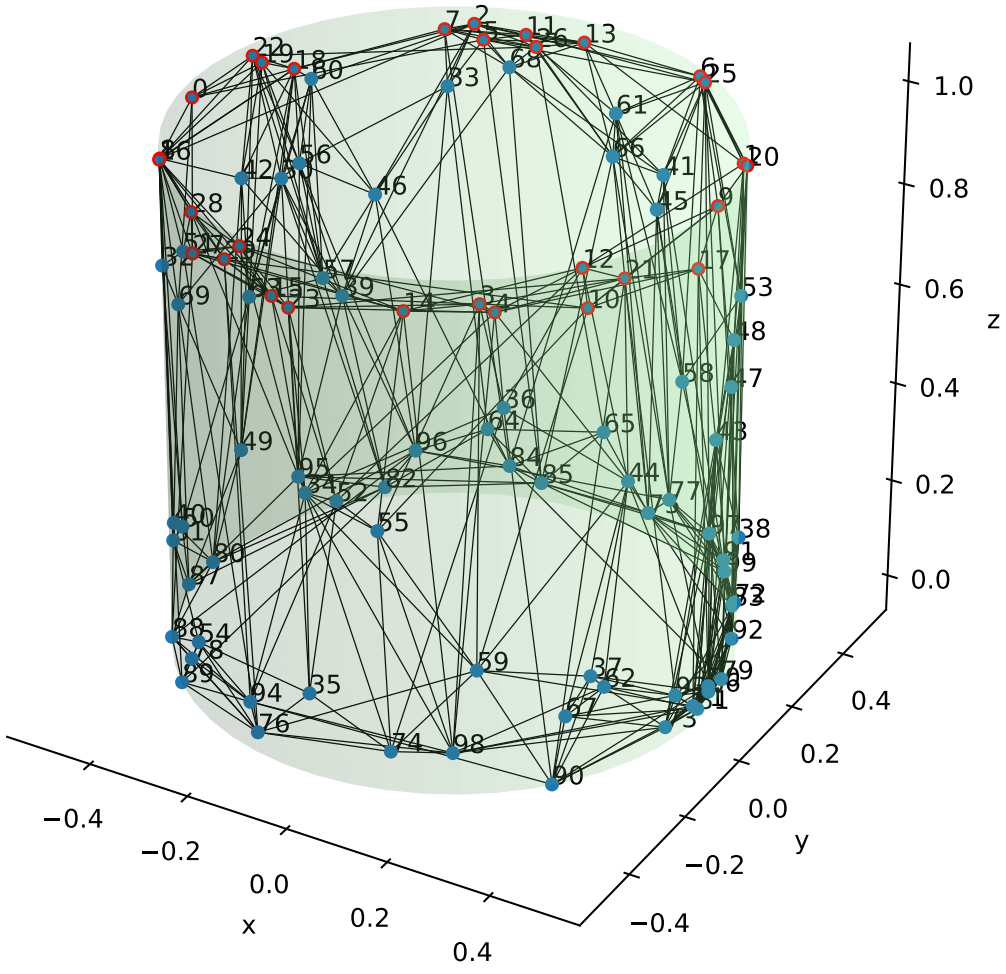

Figure 4.2: Layout of the longitudinal-biased neural network model for CB net.

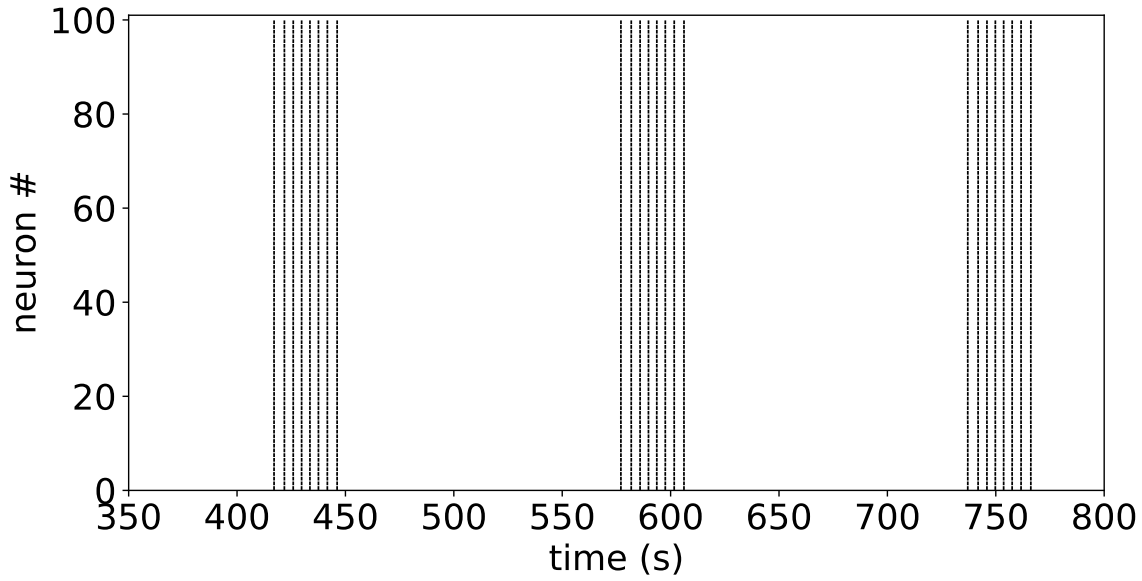

Figure 4.3: Spike trains from running simulation on the CB network model. Each index denotes a single CB neuron, increasing from top to bottom in a counterclockwise manner.

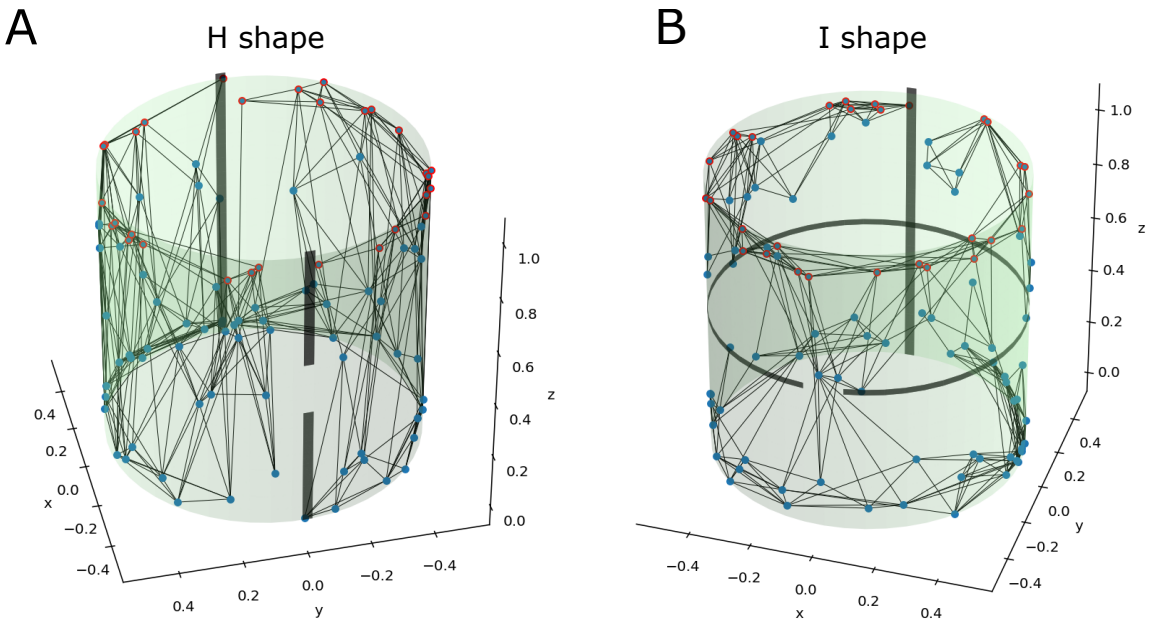

Figure 4.4: Models that are cut in different ways. (A) H-shape; (B) I-shape.

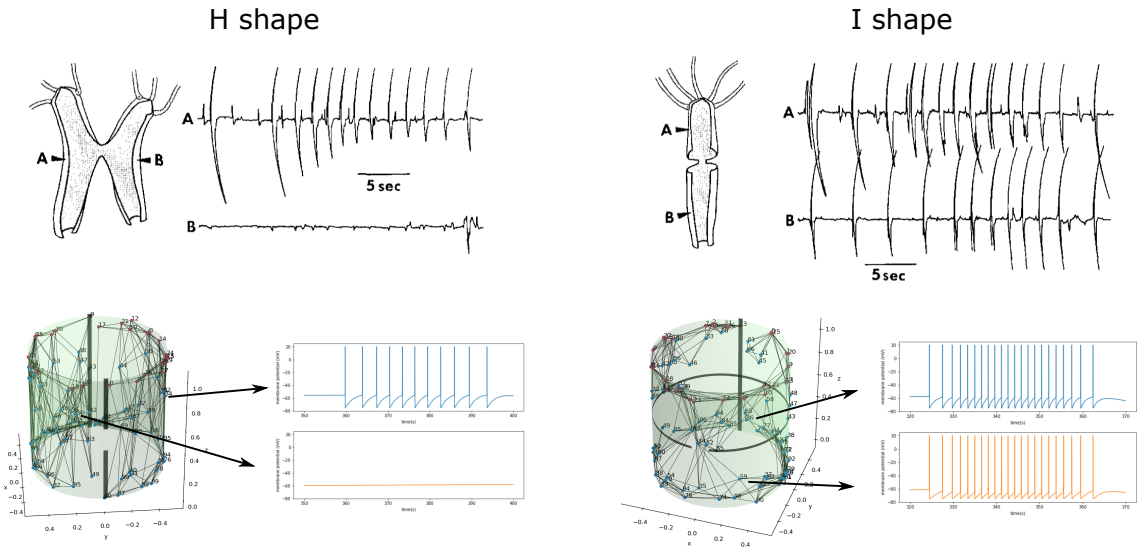

Figure 4.5: Comparisons between simulation results (bottom) and experimental recordings in [7] (top) under different cut preparations. Arrow heads marked with A, B in the top figures represent electrode placements.

arises from some environmental factor that varies periodically; it is natural and simple to attribute it to osmotic pressure, which we also assume to provide the drive for CB activity (chapter 3). Therefore, we hypothesize that the RP neuron also possesses mechanosensory channels like CB, but that its firing activity cannot drive muscle contraction and thus directly change the muscle stress. Because of its firing frequency is slower than CB, we assume that the density of mechanosensory channels on the membrane of RP is much lower than CB, represented by a smaller channel conductance in the model. Contrasting with the CB network which is taken to have specific neurons as pacemakers, we assume that every RP neuron can undertake the pacemaker role, as proposed by [16].

As with the CB network (Figure 4.6A), RP neurons are also found to be densely distributed at the two ends of *Hydra* and more sparsely at the middle body column [3], therefore we use the same algorithm as CB to randomly distribute RP on the cylindrical surface. As there has been no work done to explore the directional preference of RP connections as for [7] on CB, we build the RP network without a preferred direction, with a layout as shown in Figure 4.6B, where each orange vertex represents a RP neuron, and black links represent gap junctions connecting them.

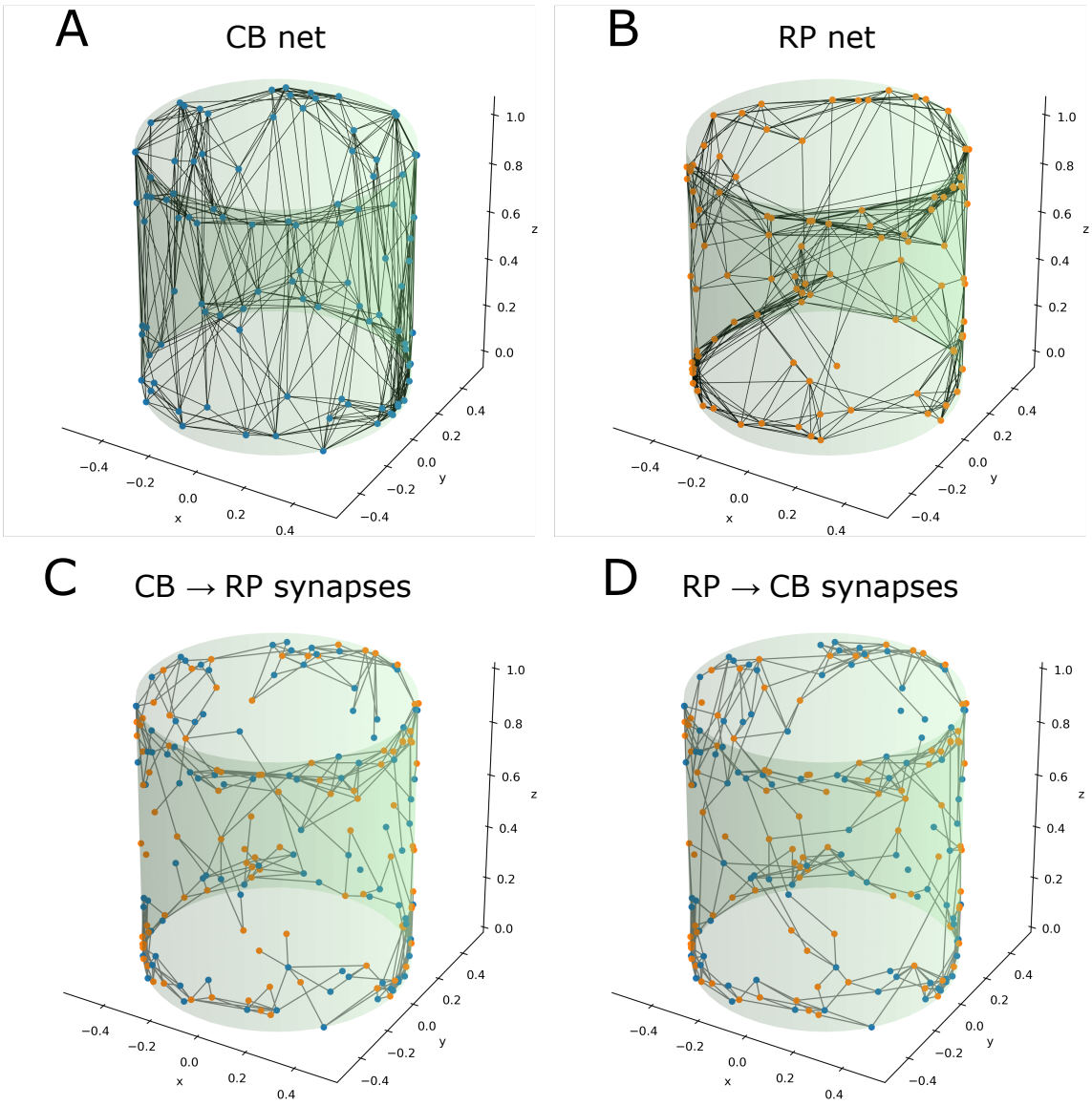

Figure 4.6: Layout of the mutual inhibition network model consisting of CB (blue, pacemakers are not highlighted here) and RP (orange) neurons. (A) Connectivity in CB net; (B) connectivity in RP net; (C) inhibitory synapses from CB to RP; (D) synapses from RP to CB.

We next include mutual inhibition between the CB and RP networks into our model. To include this, we assume the existence– which has not been directly demonstrated experimentally– of inhibitory synapses. We return to this assumption in the discussion. As within individual CB or RP networks, we distribute inhibitory synapses between CB and RP neurons (both CB $\rightarrow$ RP and RP $\rightarrow$ CB) with a distance-decayed probability. The connectivity of the mutual inhibition synapses are shown in Figure 4.6C and D.

Results from the mutual inhibition model, Figure 4.7, show the interplay of CB and RP activity as observed in experiments.

4.2.3 Simulating the difference of neural firing frequency in bisected halves

We have analysed both the network activity and the contraction state of *Hydra* in bisected animals Figure 4.8. We find that post bisection, the hypostomal half exhibits both a higher CB firing frequency as well as a lower RP firing frequency, than the peduncular half. Our statistical analysis Figure 4.9C indicates that this difference persists until 48 hrs post-bisection. These experiments confirm previous findings that expiration of the sub-hypostome halts bursts completely initially, while subsequent bursts recover with a much lower frequency over hours [14, 15].

We simulated the bisection experiments by circularly cutting the network across the vertical centerline, splitting it into two halves Figure 4.10. We then simulate the two halves independently. We find in the model that, while the CB frequency in the hypostomal half is similar to that of the intact animal Figure 4.11, the peduncular half shows no CB activity due to a lack of pacemakers; and the RP frequency in the hypostomal half is lower than that of the peduncular half due to different osmotic pressure levels and ongoing inhibition from CB, matching experimental data.

4.2.4 Simulating the recovery of CB activity in a regenerating peduncular half

As shown in Figure 4.11C-D, the lack of CB pacemakers results in an absence of CB activity and an accelerating RP frequency due to increasing osmotic pressure. However, experiments showed that the CB frequency recovers continuously after its initial absence Figure 4.8, in-

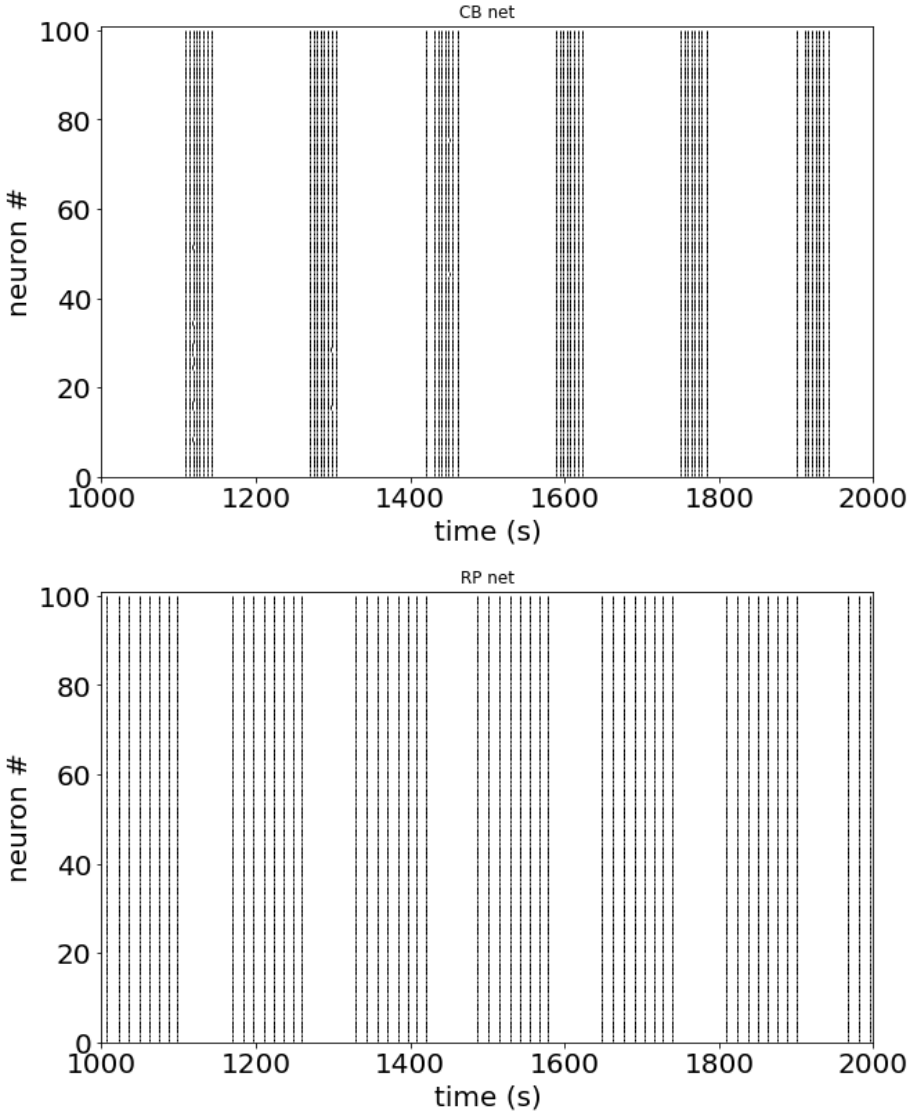

Figure 4.7: Simulation results of the mutual inhibition network. (A) Spiking trains of neurons in CB net; (B) spiking trains of neurons in RP net.

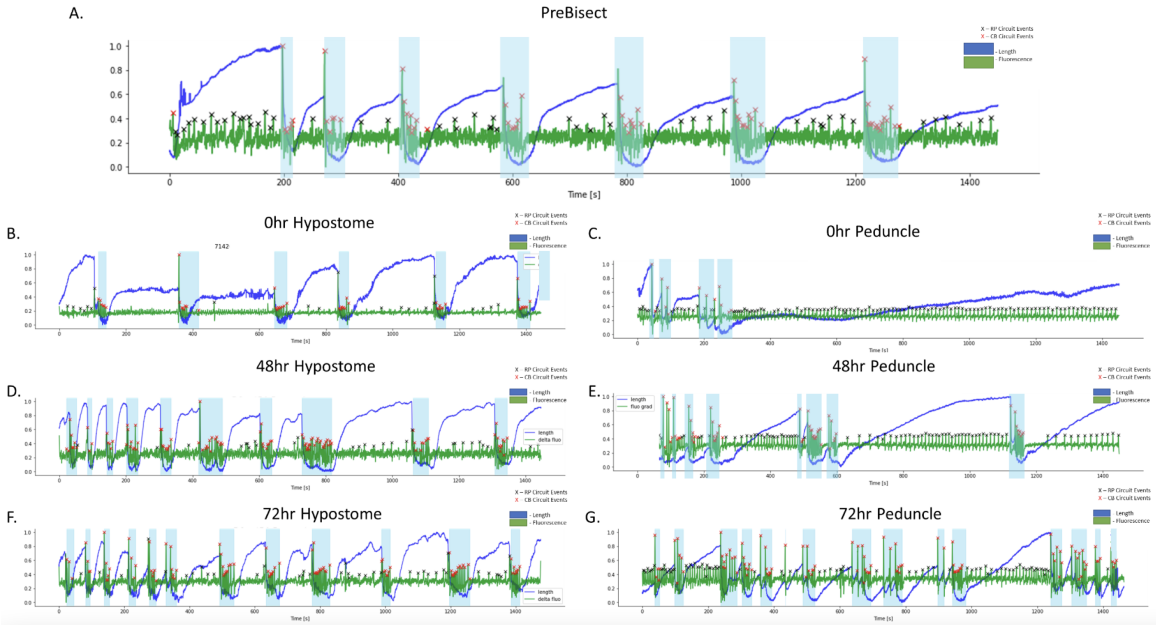

Figure 4.8: Fluorescence and behavior during regeneration of bisected *Hydra*. RP events are marked by black X's and CB events are marked by red X's. (A) Prebisection baseline data; (B-C) 0 hr after bisection; (D-E) 48 hr after bisection; (F-G) 72 hr after bisection.

dicating a regenerating CB circuit. We hypothesize that during the regeneration of peduncular half, CB pacemakers and RP neurons are generated densely near the "oral" region and sparsely at the middle column, accompanying the growth of the *Hydra* body. Meanwhile, connections are forming among the newly generated neurons and between the new and old neurons. We simulate some discrete stages during the regeneration process: for each stage, we cut the intact model at a specific z-position (a higher position for a later stage), then add a certain number of neurons around the top of the cut peduncle part (more added neurons for a later stage), and add connections involving new neurons with an increasing rate. Figure 4.12A-D shows the layout of our design, where the links denote the CB net.

The simulation results, Figure 4.12E-H, show that the CB bursts are restored when we add pacemakers into the network, with a low frequency period, with a decreasing RP frequency, successfully reproducing the experimental recordings (Figure 4.9, [14, 15]).

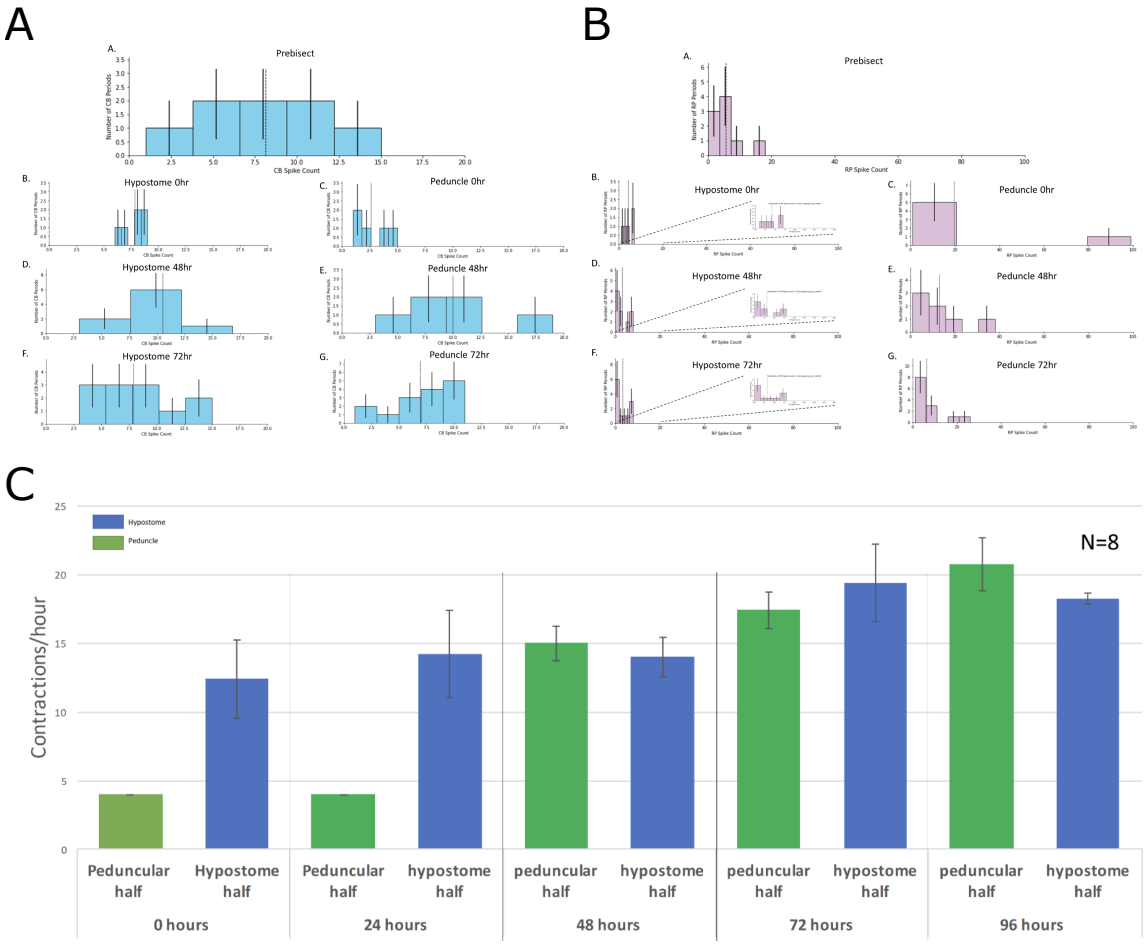

Figure 4.9: Statistical analysis from bisection experiments. (A) Distribution of CB frequency; (B) distribution of RP frequency; (C) comparison between hypostomal and peduncular halves over time.

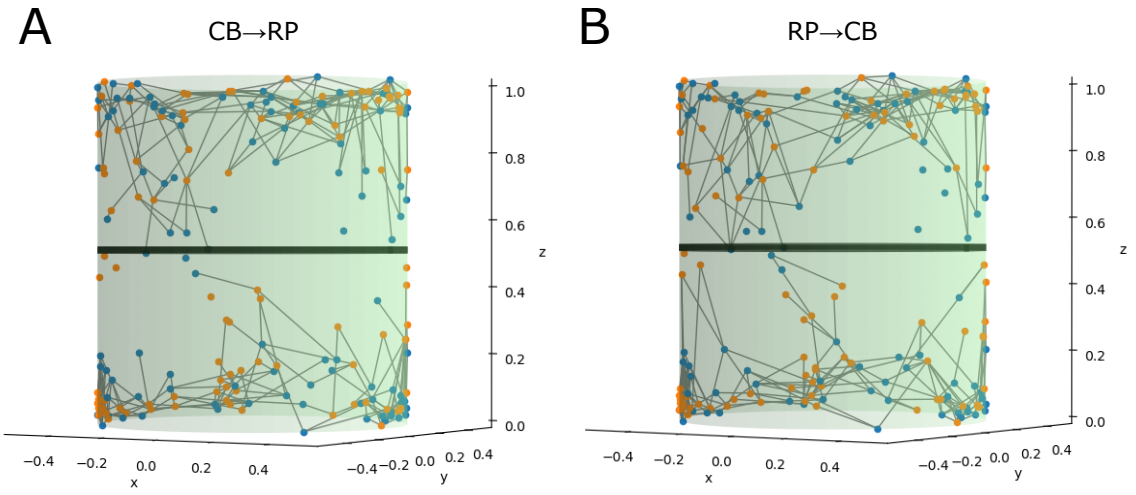

Figure 4.10: Design of bisecting the model. (A) Cut of CB → RP synapses; (B) cut of RP → CB synapses.

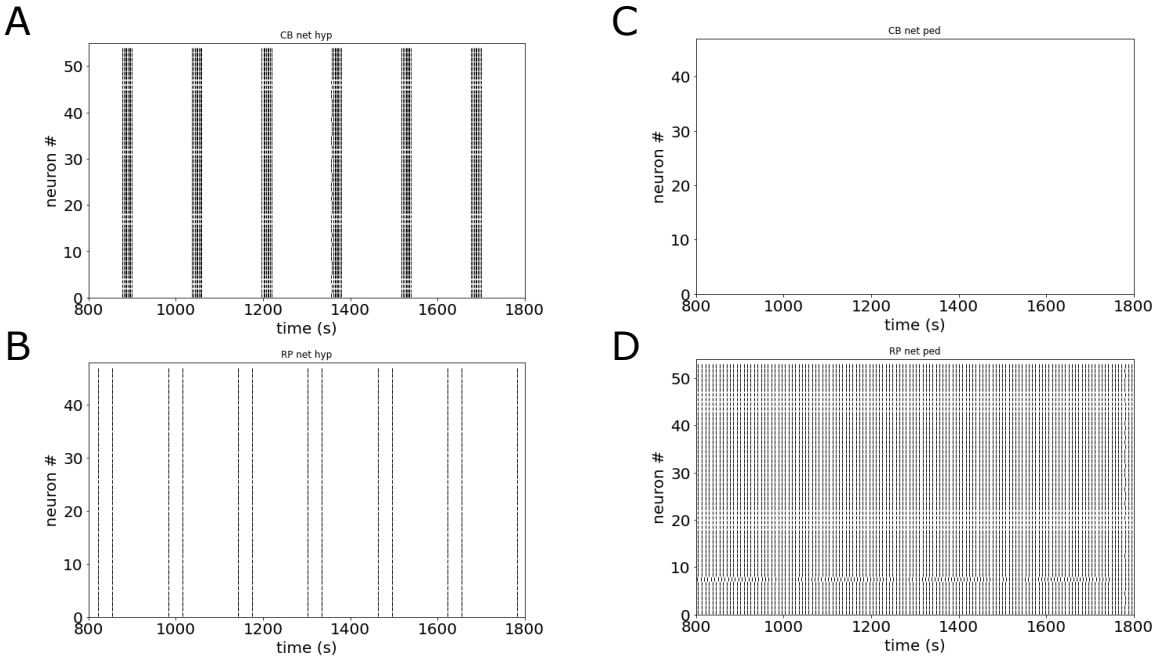

Figure 4.11: Simulation results of the bisected model. (A) CB spiking trains at hypostomal half; (B) RP spiking trains at hypostomal half; (C) CB spiking trains at the peduncular half; (D) RP spiking trains at the peduncular half.

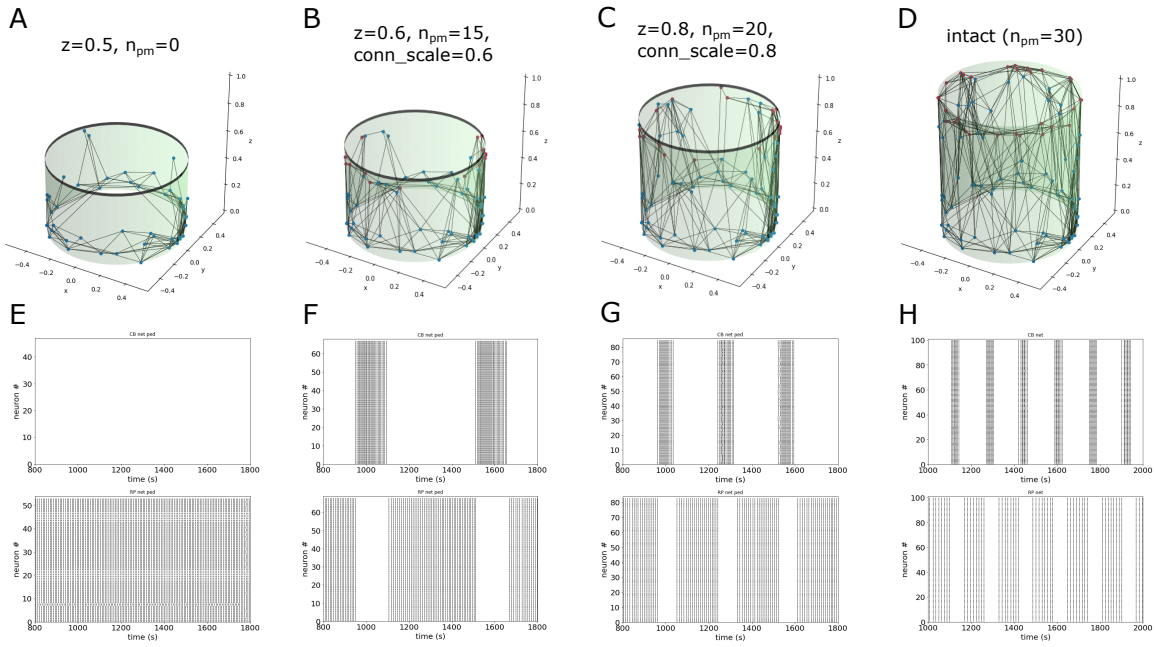

Figure 4.12: Layout (A-D) and results (E-F) of the simulation of the peduncle half regeneration, where z represents the cut position, n_{pm} represents the number of CB pacemakers, and conn_scale represents the scale of connectivity probability on newly added neurons.

4.3 Discussion

In this work, we summarize the experimental facts recorded in past studies, and build a neural network model composed of two mutually inhibiting neural nets, based on the single neuronal model described in chapter 3. Our model succeeds in qualitatively simulating the neural activity observed in both intact and split *Hydra*: the longitudinal conduction of CB pulses is explained by longitudinal-biased connectivity in CB network, the interplay of CB and RP activity is reproduced by the mutual inhibition between them, explaining the difference of neural activity between the bisected hypostomal and peduncular halves. We then apply some straightforward assumptions to capture the recovery of CB dynamics during the regeneration of the peduncular half.

Despite this success, our work has significant limitations due both to the model's simplicity and to the lack of detailed experiments with which to validate a more sophisticated model. For instance, we adopt the simplest LIF model to serve as the base of our neuronal

model, which neglects the potential nonlinearity and effects of the shape of depolarized membrane potentials, as well as neuronal geometry, which makes our model unable to accurately simulate conduction velocities of neural signals. Also, we assume that neurons are connected by gap junctions in the same subnetworks and by inhibitory synapses across different subnetworks. Even though several studies show the existence and distribution of synaptic vesicles as well as gap junctions [4, 22, 20, 21, 19], further studies are needed to determine accurate information about connections and their functions in conducting action potentials in *Hydra*'s nervous system. Increasingly advanced imaging, potentially of voltage, as well as emerging electron microscopy studies will eventually elicit the complete connectome of *Hydra*, which will support a more detailed and accurate model. These limitations notwithstanding, our model is based on and makes concrete several hypotheses derived from experimental findings, and simulates the most principle dynamics observed *Hydra*'s nerve nets. Thus it can serve as a testbed to test and reveal the organizational principles behind its operation.

We note that the mutual inhibition mechanism hypothesized in our model and its function of mediating and co-organizing one accelerating (CB) and one decelerating (RP) neural network to produce behaviors coupled with the environment shares a strong similarity with the mechanisms underlying the sympathetic (SANS) and parasympathetic (PANS) autonomic nervous system, respectively [9]. This supports the intriguing idea raised by Karemaker [6] that *Hydra*'s nerve net may be the ancestor of the autonomic nervous system (ANS) in mammalians. Our model, which integrates such co-ordination of neural networks and their coupling with the environment, may serve as a prototype for future modeling studies of higher complexity ANSs.

4.4 Materials and Methods

Our model is built with Python 3. Differential equations are solved using Euler stepping method with a 10 ms time step. All codes are available at github.com/hengjiwang/hydranerv.

Parameter	Value	Unit
C_m	50	nF
g_L	15 (CB) / 1 (RP)	nS
E_L	-75	mV
g_s	25 (CB pacemakers) / 2 (RP) / 0 (CB passive)	nS
k_b	106	1
s	0.00277	Pa^{-1}
q	1	1
m	25	1
E_s	10	mV

Table 4.1: Parameters for single CB / RP neurons.

4.4.1 Single neuronal models

Our model for both CB and RP neurons are LIF models with mechanosensitive channels as described in chapter 3 Equation 3.1, including a refractory period $t_{\text{ref}} = 100$ ms for valid propagation of action potentials:

The equations of muscle stress dynamics are the same with those in chapter 3 Equation 3.2 and Equation 3.3, with $k_a = 7500$ Pa, $k_e = 1000$ Pa, and all other parameters remain the same.

4.4.2 Gap junctions

Same as chapter 3, the gap junctional input from other neurons to neuron i is formulated as

$$I_c^i = g_c \sum_{j \in J} (V_j - V_i) \tag{4.1}$$

where g_c is the undirectional coupling coefficient and J is the set of all neighbors of neuron i. In this work, $g_c = 500$ nS for both CB and RP networks.

4.4.3 Inhibitory synapses

The current of the inhibitory synapse between each pair of CB and RP neurons is modeled as Equation 4.2

$$I_{\text{inh}} = -\sum_{t^{(f)}} I_0 \exp\left(-\frac{t - t^{(f)}}{\tau_{\text{inh}}}\right) \Theta(t - t^{(f)}) \tag{4.2}$$

where I_0 is a constant representing the increment caused by each firing event of the pre-synaptic neuron, $t^{(f)}$ is each firing moment of the pre-synaptic neuron, τ_{inh} is the time constant of the decay of I_{inh}, $\Theta(\cdot)$ is the Heaviside step function. In our simulations, we set $I_0 = 40$ pA and $\tau_{\text{inh}} = 5$ s for both CB $\rightarrow$ RP and RP $\rightarrow$ CB synapses.

4.4.4 Distribution of connections

The connectivity probability of intra-network gap junctions and inter-network inhibitory synapses are modeled as Equation 4.3, inspired by [12]:

$$P_{ij} = \exp\left(-d_{ij}^2 / 2\lambda_d^2\right) \tag{4.3}$$

where i, j are the indices of neurons which are either CB or RP neurons. d_{ij} here is the scaled distance between neuron i and j on the cylindrical surface as in Equation 4.4, λ_d is the distance constant which is set as 0.15 for CB network and inter-network inhibitory synapses (both CB $\rightarrow$ RP and RP $\rightarrow$ CB), and 0.25 for RP network.

$$d_{ij} = \sqrt{(\rho(\phi_i - \phi_j))^2 + (\alpha(z_i - z_j))^2} \tag{4.4}$$

where ρ is the radius of the cylinder which is set as 0.5 in our model, ϕ, z are respectively the angle and height coordinates of a neuron. α here is the longitudinal scale factor as we mentioned in the text, and a smaller α corresponds to a more longitudinal-preferred connectivity of the network. We set $\alpha = 0.3$ for the CB network and $\alpha = 1$ for the RP network and inter-network inhibitory synapses.

Bibliography

[1] Krishna N Badhiwala, Abby S Primack, Celina Juliano, and Jacob T Robinson. Multiple neuronal networks coordinate hydra mechanosensory behavior. *bioRxiv*, pages 2020–10, 2021.

[2] S Chillemi, M Riani, and E Simonotto. Neural network model of hydra photoresponsive. *Biocybernetics Of Vision: Integrative Mechanisms And Cognitive Processes*, 2:108, 1998.

[3] Christophe Dupre and Rafael Yuste. Non-overlapping neural networks in hydra vulgaris. *Current Biology*, 27(8):1085–1097, 2017.

[4] Arthur R Hand and Stephen Gobel. The structural organization of the septate and gap junctions of hydra. *The Journal of cell biology*, 52(2):397–408, 1972.

[5] Robert K Josephson. Conduction and contraction in the column of hydra. *Journal of Experimental Biology*, 47(1):179–190, 1967.

[6] John M Karemaker. An introduction into autonomic nervous function. *Physiological measurement*, 38(5):R89, 2017.

[7] G Kass-Simon. Longitudinal conduction of contraction burst pulses from hypostomal excitation loci inhydra attenuata. *Journal of comparative physiology*, 80(1):29–49, 1972.

[8] G Kass-Simon. Coordination of juxtaposed muscle layers as seen in hydra. In *Coelenterate ecology and behavior*, pages 705–714. Springer, 1976.

[9] John Newport Langley. *The autonomic nervous system.* W. Heffer & Sons, Limited, 1921.

[10] Jonathan R Lovas and Rafael Yuste. Ensemble synchronization in the reassembly of hydra's nervous system. *Current Biology*, 31(17):3784–3796, 2021.

[11] CB McCullough. Pacemaker interaction in hydra. *American zoologist*, 5(3):499–504, 1965.

[12] Rich Pang and Adrienne L Fairhall. Fast and flexible sequence induction in spiking neural networks via rapid excitability changes. *Elife*, 8, 2019.

[13] LM Passano and CB McCullough. The light response and the rhythmic potentials of hydra. *Proceedings of the National Academy of Sciences of the United States of America*, 48(8):1376, 1962.

[14] LM Passano and CB McCullough. Pacemaker hierarchies controlling the behaviour of hydras. *Nature*, 199(4899):1174–1175, 1963.

[15] LM Passano and CB McCullough. Co-ordinating systems and behaviour in hydra: I. pacemaker system of the periodic contractions. *Journal of Experimental Biology*, 41(3):643–664, 1964.

[16] LM Passano and CB McCullough. Co-ordinating systems and behaviour in hydra ii. the rhythmic potential system. *Journal of Experimental Biology*, 42(2):205–231, 1965.

[17] Joshua J Swore. *Molecular and Biophysiological Differences in Neuronal Innexin Gap Junctions Likely Underlie Unique Circuit Behaviors in Hydra vulgaris*. PhD thesis, University of Washington, 2022.

[18] Cloe Taddei-Ferretti and S Chillemi. Modulation of hydra attentuata rhythmic activity. *Biological cybernetics*, 56(4):225–235, 1987.

[19] Yasuharu Takaku, Jung Shan Hwang, Alexander Wolf, Angelika Böttger, Hiroshi Shimizu, Charles N David, and Takashi Gojobori. Innexin gap junctions in nerve cells coordinate spontaneous contractile behavior in hydra polyps. *Scientific reports*, 4:3573, 2014.

[20] Jane A Westfall. Ultrastructural evidence for a granule-containing sensory-motor-interneuron in hydra littoralis. *Journal of ultrastructure research*, 42(3-4):268–282, 1973.

[21] Jane A Westfall, John C Kinnamon, and David E Sims. Neuro-epitheliomuscular cell and neuro-neuronal gap junctions inhydra. *Journal of neurocytology*, 9(6):725–732, 1980.

[22] Richard L Wood and Aileen M Kuda. Formation of junctions in regeneratin hydra: Gap junctions. *Journal of ultrastructure research*, 73(3):350–360, 1980.

Chapter 5

CONCLUSIONS

In this project I have built different computational models demonstrating the mechanisms of *Hydra*'s neuromechanical dynamics as well as the dynamics of single neurons and neural networks. These models together have, for the first time, unraveled the physiological mechanisms and fundamental principles behind behaviors and physiological recordings that haven been explored for more than 270 years, in a unified modeling perspective at single cellular resolution. In the biomechanical model of chapter 2, I built a biophysical model composed of Hodgkin-Huxley style single cellular models of epitheliomuscular cells, and simulated the emergence of *Hydra*'s various behaviors from molecular-level dynamics and inter-cellular communications. In the model for the single CB neuron in chapter 3, I creatively coupled neural activity with properties of the environment, without sacrificing the model's simplicity and successfully matched major experimental observations. In my model of the neural network of *Hydra* in chapter 4, I extended the work in chapter 3 to simulate coupling between subnetworks, capturing many network-level phenomena observed in past experiments, based on a mutual inhibitory co-ordination principle which infers the evolutionary path from *Hydra* nerve net to the autonomic nervous system in advanced animals. These models, which span the multiple temporal and spatial scales that characterize dynamics and movement control, provide a complete interpretation of how neural, muscular and mechanical systems jointly evolve in organisms within their environments to affect coordinated motion and maintain the life of *Hydra* as a whole animal.

Despite the completeness and power of our models, they are based on a variety of hypotheses due to the lack of complete neurophysiological information. This is both inevitable for all modeling studies, and underscores the value of them. The hypotheses and predictions from our model, such as the coordination between CB activity and the muscle stress, and the distance decay connectivity between neurons, are waiting to be verified or challenged by

future detailed experiments. Furthermore, with future development of imaging techniques and data analysis tools, we believe that a comprehensive connectome of *Hydra* will eventually be extracted, and a more accurate model that integrates all components introduced in this dissertation will be constructed for *Hydra*, and for increasingly more complex nervous systems, including our brains.